ICFO-The Institute of Photonic Sciences

Doctoral Thesis

New phenomena in high-quality suspended nanotube devices

Author:
Carlos
Urgell Flores

Supervisor:
Prof. Adrian
Bachtold

A thesis submitted in fulfillment of the requirements for the degree of Doctor of Photonics

in the

Quantum Nanomechanics Group

February 2021

Acknowledgements

First, I would like to thank my advisor Prof. Adrian Bachtold for giving me the opportunity to do my PhD in the Quantum Nanomechanics group. This thesis would not have been possible without his guidance, optimism and, expertise.

I would like to thank Prof. Takis Kontos, Prof. Gary Steele and, Prof. Darrick Chang for kindly accepting to be part of my thesis committee. I would also like to thank Prof. Sergio Valenzuela and Prof. Hugues de Riedmatten for agreeing to be the substitute members.

I want to thank Prof. Wei Yang for his invaluable help throughout my PhD. None of this would have been possible without him, I am very grateful to have been able to work as a team with him. Apart of helping me to develop my career as a scientist, he helped to me grow up and develop myself as a person. I really appreciate that Adrian and Wei were always there to explain me everything I needed, thank you for your patience. I would also like to thank Dr. Sergio de Bonis for his help during all my PhD, he selflessly shared all the knowledge and expertise he accumulated during his scientific career. He never said no when I asked for help. I also want to acknowledge Dr. Gernot Gruber for his insight and contribution to the project we carried out, we really spent a nice time working together.

Further, I really appreciate how all the former and current members of the Quantum Nanomechanics group contributed to create a nice and relaxed working atmosphere. Thank you Adrien Noury, Jorge Vergara, Nicolás Morell, Jil Schwender, Peter Weber, Ioannis Tsioutsios, Alexandros Tavernarakis, Antoine Reserbat-Plantey, Lorenzo Vistoli, Roger Tormo Queralt, Chandan Samanta, Christoffer Møller, Parmeshwar Prasad and, Slaven Tepsic.

I would also like to thank all ICFO's members of the mechanical workshop, electronic workshop, clean room, maintenance and, human resources who supported and helped me during my PhD.

Finally, I want to thank my family and friends who have always been by my side throughout this stage of my life. Specially you Teresa, thank you for joining me on this journey.

Abstract

Carbon nanotubes (CNTs) have attracted the attention of the scientific community since their discovery in the 90s. They are an excellent material for the development of research fields as diverse as nanomechanics or quantum transport. Nanotube mechanical resonators are endowed with exceptional properties, including extremely small mass, ultra narrow cross-section, and operation over a large frequency range from 10 kHz to 10 GHz. They are also fantastic sensors of both mass adsorption and forces.

Its electric transport properties are remarkably the long ballistic transport of charge carriers, strong electron-electron interaction, and the important role of the spin and valley degrees of freedom. It is possible to observe a wide range of quantum transport phenomena ranging from single-electron tunneling to Kondo physics and Fabry-Pérot interference. It should be noted that the electrical transport and mechanical motion of suspended nanotubes can be coupled by a large amount.

In the first part of this thesis, we present an advanced ultrasensitive fabrication method that allows us to build and functionalize a nanotube cantilever for optical measurements. We grow a platinum particle at the end of the nanotube in order to increase laser reflection. For this, we track the material deposition on the cantilever through the electromechanical coupling with the electron beam during the process.

Next, we show electron transport measurements in high-quality devices with high transmission. While high-temperature measurements indicate electron-electron correlations, low-temperature transport characteristics point towards single-particle Fabry-Perot interference. We observe this effect both by modifying the temperature and by tuning the source-drain voltage. This effect is attributed to the interplay between fluctuations and quantum interactions in a correlated Fabry-Pérot regime.

In the last part, we show that it is possible to couple the mechanical movement of the CNT to the electron transport. By applying an electron current through the system, we can either cool or amplify the mechanical motion of the eigenmode. We cooled the nanoresonator down to 4.6 ± 2.0 quanta of vibration. The instabilities present in electron transport measurements are attributed to self-oscillation induced by the backaction amplification. These effects have an electrothermal origin. This method can be used in the future to cool NEMS into the quantum regime.

Resumen

Los nanotubos de carbono (CNTs) han suscitado el interés de la comunidad científica desde su descubrimiento en la década de los 90. Son un excelente material para el desarrollo de campos de investigación tan diversos como la nanomecánica o el transporte cuántico. Los resonadores mecánicos de nanotubos están dotados de propiedades excelentes, incluyendo una masa extremadamente pequeña, una sección transversal ultra estrecha, y funcionamiento en un amplio rango de frecuencias de 10 kHz a 10 GHz. También son fantásticos sensores de la absorción de masas y fuerzas.

Sus propiedades de transporte eléctrico son notablemente el largo transporte balístico de los portadores de carga, una fuerte interacción electrón-electrón y el importante papel de los grados de libertad de espín y valle. Es posible observar un ancho rango de fenómenos cuánticos que van desde la el efecto tunel de un solo electrón hasta la física de Kondo y la interferencia de Fabry-Pérot. Cabe señalar que el transporte eléctrico y el movimiento mecánico de los nanotubos suspendidos pueden ser acoplados en gran medida.

En la primera parte de esta tesis, presentamos un método de fabricación avanzado ultra-sensitivo que nos permite construir y funcionalizar un cantilever de nanotubo para medidas ópticas. Crecemos una partícula de platino en el extremo del nanotubo con el fin de aumentar la reflexión láser. Para ello, rastreamos la deposición del material en el cantilever a través del acoplamiento electromecánico con el haz de electrones durante el proceso.

Seguidamente, mostramos medidas de transporte de electrones en dispositivos de alta calidad con una alta transmisión. Mientras que las medidas a alta temperatura indican correlaciones electrón-electrón, características de transporte a baja temperatura apuntan hacia interferencia de Fabry-Pérot. Observamos este efecto tanto al modificar la temperatura como al variar el voltaje fuente-drenador. Este efecto se atribuye a la relación entre las fluctuaciones y las interacciones cuánticas en un régimen de Fabry-Pérot correlacionado.

En la última parte, mostramos que es posible acoplar el movimiento mecánico del CNT al transporte de electrones. Al aplicar una corriente de electrones a través del sistema podemos enfriar o amplificar el movimiento mecánico del modo propio. Enfriamos el nanoresonador hasta 4.6 ± 2.0 cuantas de vibración. Las inestabilidades presentes en el transporte de electrones son atribuidas a la autooscilación inducida por la amplificación de retroacción. Estos efectos tienen un origen electrotermal. Este método puede ser usado en el futuro para enfriar NEMS al régimen cuántico.

Contents

Chapter 1

Introduction

Nowadays, mechanical resonators have become a fundamental part of our daily life. We can find them in numerous devices that we constantly use. Specifically, micro-electromechanical systems (MEMS) are present in our cars, mobile phones, speakers, and computers, among many other devices. Accelerometers, gyroscopes, pressure sensors, bio-sensors or mirror arrays are designed using MEMS. Few commercial examples can be seen in Fig. 1.1. These type of systems are also an essential tool in research.Many breakthroughs are being achieved thanks to them. Some examples include the creation of the atomic force microscopy (AFM) achieved in 1986 [1], the ground state cooling of the mechanical resonator eigenmode in 2010 [2] and the first observation of gravitational waves in 2015 [3].

As R. Feynman stated in 1959: "There is plenty of room at the bottom". The miniaturization but specially the change of scope from a top-down to a bottom-up approach have allowed the reduction of the size of mechanical systems. We are now in the times of nano-electromechanical systems (NEMS).

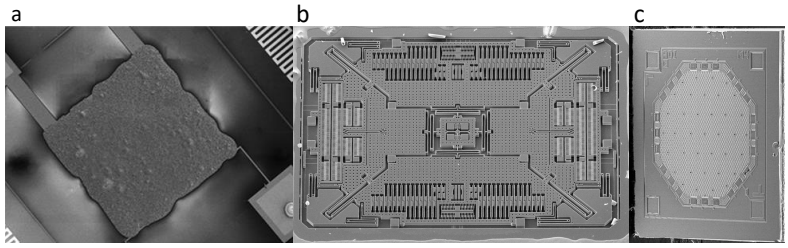

FIGURE 1.1: **Examples of commercial MEMS. (a)** Part of a chemoresistive gas sensor based on MEMS microheater. **(b)** A commercial gyroscope that is part of a low-power three-axis angular rate sensor. **(c)** MEMS microphone designed to be incorporated in a next generation of smaller, more efficient, higher quality hearing aids.

The mechanical motion of both MEMS and NEMS has been successfully coupled to other degrees of freedom. These systems include the charges of single-electron transistors [4–12], the Copper pairs of superconducting circuits [13], the quantum states of qubits [14], superfluids [15, 16], microwave radiation [17, 18], and electron or nuclear spins [19–21]. In this work we study in detail a system based on a carbon nanotube (CNT) which is used as both a single-electron transistor (SET) and a mechanical resonator (as depicted in Fig. 1.2(a)) so that the mechanical properties and the electronic transport are intrinsically coupled.

CNTs are carbon based hollow cylinders with exceptional mechanical and electrical properties. They possess a high strength and a very low mass. Among its mechanical properties, the following stand out: The tunability of its resonance frequency [22], the possibility of pushing it to the GHz frequency range [23, 24] and the high Q factor [25, 26]. This makes them excellent sensors. For example, they have been used in mass sensing experiments with an unprecedented resolution [27]. In addition, the force and displacement sensitivity have been demonstrated to reach values low enough to be able to detect the magnetic force created by a single nuclear spin [28, 29].

We here highlight the electronic properties of nanotubes. It is possible to have ambipolar transport, where the electronic transport can be carried by either holes or electrons by tuning the sign of the CNT electrochemical potential [30, 31]. Different transport regimes can be observed [32], from Coulomb Blockade [31, 33–36] and Kondo [37–40], where electron correlations dominate, to Fabry-Pérot interference [41, 42], where the wave-particle duality of the charge carriers manifests. The charge carrier mobility is extraordinarily high allowing the creation of an electron-waveguide in a CNT transistor. Fig. 1.2(b) shows the usual conductance curve of an ultraclean CNT where different regimes can be clearly distinguished.

Due to the coupling of the mechanical motion to other degrees of freedom, mechanical systems have been cooled to the quantum regime [43–45]. Different MEMS and NEMS have reached the ground state but not CNTs [18, 46, 47]. The motion of mechanical systems has been also amplified leading to self-oscillation [48–50]. In NEMS based on CNTs, the coupling between electron transport and the mechanical motion leads to important backaction effects. This enabled the control of the resonance frequency and the dissipation [7, 8]. New instabilities in quantum transport has been attributed to the electromechanical coupling [8]. However, cooling of the mechanical motion has never been achieved in a CNT-based NEMS.

This thesis explores all the intriguing phenomena associated to suspended nanotubes. We report on advances in the fabrication and functionalization of CNT force sensors. We present low temperature transport measurements in ultra-high quality CNT quantum dots. We focus in an intermediate regime where no clear energy scale dominates

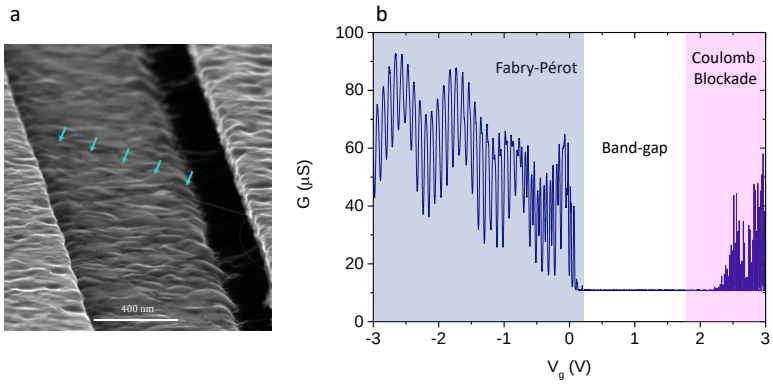

FIGURE 1.2: **Characterization of a CNT electromechanical resonator. (a)** Scanning electron microscopy (SEM) image of a CNT-based resonator suspended over a gate electrode and clamped between source and drain electrodes. **(b)** Electrical conductance of a CNT-based single electron transistor (SET) as function of the DC gate voltage measured at cryogenic temperatures.

and both electron correlations and interference effects are important. The transition between these different transport regimes is studied in detail. Finally, the interplay between mechanical motion and electron transport in a weak coupling regime is analyzed. We either cool or amplify the mechanical motion of the eigenmode of a CNT resonator. We discuss the origin of this backaction effect. Our work shows that the origin of the instabilities observed in quantum transport is related to self-oscillation.

The thesis structures as follows:

- **Chapter 2** presents the crystalline structure of CNTs and its main electronic and mechanical properties.
- **Chapter 3** introduces the basics of electron transport in quantum dots, with a special attention to nanotube-based devices. The concept of noise and its main contributions to nanotube devices is also introduced.
- **Chapter 4** builds the the framework to understand mechanical resonators. Here we introduce the concept of backaction.
- **Chapter 5** presents the fabrication methods used to produce ultra-high quality electrical devices based on suspended nanotubes. An advanced fabrication and functionalization process to prepare a CNT force sensor for optomechanical measurements is also described in this chapter.

- **Chapter 6** discusses the measurement setup used in the experiments presented in this work. Different methodologies are presented to quantify the quality of the filtering and thermalization by measuring the electronic temperature of the system.
- **Chapter 7** reports electron transport measurements in ultra-clean CNTs with high transmission. Here, we study the energy scales of the system and the interplay between quantum interference and electron correlations.
- **Chapter 8** demonstrates a simple yet powerful method to cool or amplify the eigenmode of a CNT resonator based on the use of a DC electron current.

Chapter 2

Carbon nanotubes

In this chapter we introduce the basic properties of carbon nanotubes. First we introduce the material and its history, describing the connection between graphene and carbon nanotubes. Then, we review the mechanical and electronic properties of the carbon nanotubes using their crystallographic structure.

2.1 Introduction

Graphene is a two dimensional material based in an atomically thin layer of carbon atoms arranged in a hexagonal lattice, while a carbon nanotube (CNT) can be understood as a rolled-up graphene sheet. In electron transport, it is considered one dimension, when the sub-band spacing is larger than the thermal energy and the elastic length. In both cases the carbon atoms are bonded by covalent bonds. Graphene is considered to be the basic building block of graphite, which consists in graphene sheets stacked by Van de Waals interaction. CNTs are classified in two categories according to their number of layers: Single-walled carbon nanotubes (SWCNTs) and multi-walled carbon nanotubes (MWCNTs). SWCNTs consist in one individual rolled-up sheet with a diameter about one nanometer. MWCNTs are an arrangement of multiple concentric shells of SWCNTs stacked together.

Basically, CNTs were known long before graphene. CNTs were experimentally discovered by Ijima in 1991 [51], while graphene was isolated for the first time by Andre Geim and Konstantin Novoselov in 2004 [52]. CNTs can be synthesized by different fabrication processes, such as chemical vapour deposition (CVD) [53], laser ablation [54] and arc discharge [51, 55]. CVD is the most common fabrication process; we used it in the experiments shown in this thesis. The length of the tubes obtained by this mean can range from few hundred nanometers to few millimeters depending on the process parameters [56, 57]. Additionally, other characteristics like the radius, the purity or the number of CNTs can be tuned with the fabrication parameters [58, 59].

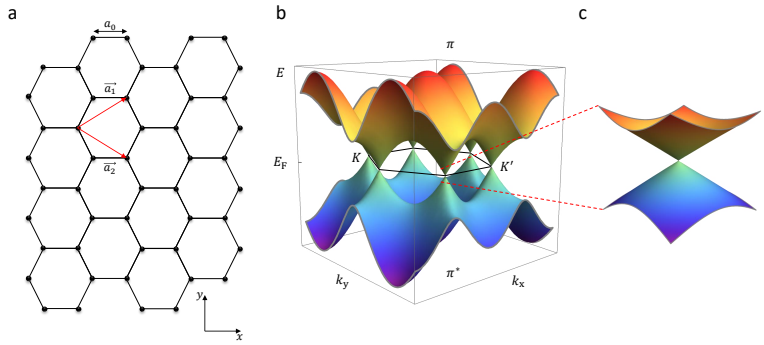

FIGURE 2.1: **Lattice and band-structure of graphene.** **(a)** The characteristic honeycomb lattice of a graphene flake with an inter-atomic distance a_0 and the unit cell defined by the vectors $\vec{a_1}$ and $\vec{a_2}$. **(b)** The band-structure where the K and $K^{'}$ points of the hexagonal first Brillouin zone are highlighted. The orbitals π and π^* merge at these points defining the electronic properties of graphene. **(c)** The characteristic linear energy dispersion at low energy around the K and $K^{'}$ points. The figures **b** and **c** have been adapted from [60].

Both materials share many of their properties. Next, we will proceed by presenting the basic mechanical and electronic properties of CNTs which, in some cases, can be explained directly from the inherent characteristics of graphene. This will allow us to understand the uniqueness of these systems and motivate their use nanoscience.

2.2 Electronic properties

The CNT electronic properties can be directly explained from the band-structure of graphene. Therefore, we start by introducing the key properties of graphene. In Fig. 2.1, we can see the honeycomb lattice of graphene , where the carbon-carbon bonds have a length of $a_0 = 0.142$nm, together with its band-structure. The unit cell in the lattice is defined by the vectors $\vec{a_1}$ and $\vec{a_2}$ and it contains only two carbon atoms.

Every carbon atom contains four covalent electrons, three of them are hybridized in a strong sp^2 orbital while the electrons which contribute to the electronic transport belong to the p_z orbital. The electrons in the sp^2 orbital play an important role in the elastic properties of the material which we discuss in the next section. They don't contribute to the electronic properties since its energy is far from the Fermi

energy E_F. The electrons in the p_z orbital, which lay perpendicular to the lattice, form the delocalized π-bonds. If we calculate the lower energy π-band structure using the tight binding model, we obtain the following energy dispersion relation for the valence and conductance band:

$$E(\vec{k}) = \pm\gamma_0\sqrt{3 + 2\cos(\vec{k}\cdot\vec{a}_1) + 2\cos(\vec{k}\cdot\vec{a}_2) + 2\cos(\vec{k}\cdot(\vec{a}_2 - \vec{a}_1))}, \tag{2.1}$$

where γ_0 represents the nearest hopping energy and the positive and negative solution denote the two sub-bands which converge into the charge neutrality point, which can be observed in Fig. 2.1(b) and Fig. 2.1(c). These symmetric bands form a cone shape located at the vertices of the Brillouin zone. This symmetry suggests that electrons and holes have the same properties in graphene. Two of these six points are non-equivalent due to symmetry reasons. These two points are the so-called K and K' valleys. Near the charge neutrality point, the energy dispersion relation can be approximated by a linear dispersion relation

$$E(\vec{k}) \approx \pm\hbar v_F\,|k|\,. \tag{2.2}$$

If $\gamma_0 = 3$ eV, the Fermi velocity is $v_F = \sqrt{3}a\gamma_0/2\hbar \approx 10^6$ m/s. The electrons in these states behave as massless particles and are called relativistic Dirac Fermions. Since at the charge neutrality point (described around $E_F = 0$) the two sub-bands touch together, graphene is known as a zero-band gap semiconductor.

Now, let's understand the properties of a nanotube. The electronic properties of such a structure are determined by the symmetry of the crystalline lattice. The vector $\vec{C} = \vec{a_1}n + \vec{a_2}m$ with $n, m \in \mathbb{Z}$, is known as the chiral vector and accounts for the axis symmetry. It connects lattice sites on opposite sides of the surface that are superposed when the graphene is rolled up forming a nanotube. The angle between the vectors $\vec{C}$ and $\vec{a_1}$ defines the chiral angle θ as despicted in Fig. 2.2. Basically, θ refers to the angle between the axis of the CNT and the orientation of the lattice. The chirality or chiral angle of the nanotube can be determined by the integer numbers n and m. Finally, a nanotube with the so-called chiral indices (n, m) is armchair for $(n, m = n)$, zig-zag if $(n, 0)$, and chiral for arbitrary (n, m).

The electronic properties of SWCNTs can be calculated from the band structure of graphene applying periodical boundary conditions around the circumference. It depends on the chirality of the tube which determines if the SWCNT is metallic or semiconductor. The

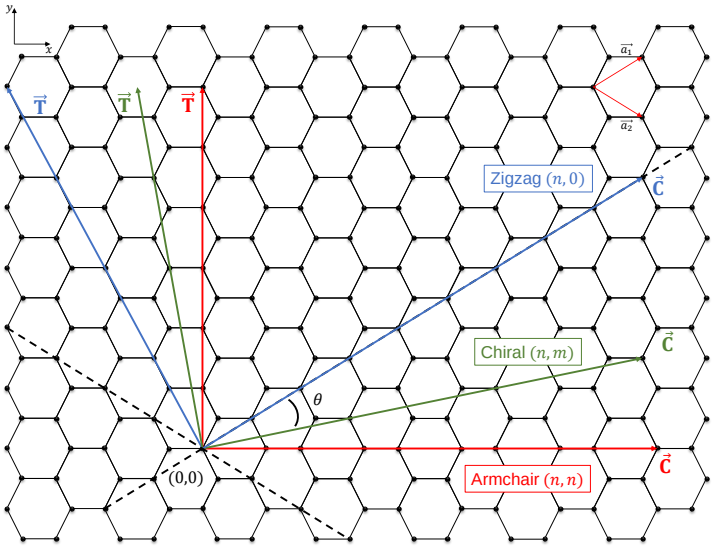

FIGURE 2.2: **Defining a CNT from a graphene sheet.** The CNT surface is defined by the chiral vector $\vec{C}$ and the translation vector $\vec{T}$. Additionally, the electronic properties are also defined by the surface area. The 3 different species of CNTs; armchair (n, n), zig-zag $(n, 0)$, and chiral (n, m) are represented by their characteristic vectors.

boundary conditions are introduced trough the zone-folding approximation which states that the wave vector $\kappa_\perp$ is quantized in the direction of the $\vec{C}$ vector of the tube. The electrons move freely in the axial direction so the transversal vector $\kappa_\parallel$ is not quantized when the nanotube is sufficiently long.

There is one sub-band per quantized $\kappa_\perp$ vector. As for the graphene case, the electronic transport is given by the states in the sub-band with $E(\kappa)$ around E_F. If at least one sub-band crosses the K-points, the CNT is metallic, while in the opposite case the CNT is semiconducting, as shown in Fig. 2.3. The energy band gap of semiconducting CNTs is given by $E_G = \frac{0.7}{d}$ eV, where d is the diameter of the CNT in nm. Finally, we emphasize that a comparatively small energy gap emerges in metallic nanotubes that are not armchair due to the curvature of the system..

As is the case for graphene, CNTs show extraordinary high electron mobility [35, 61], and ambipolar effect [30, 31]. Therefore, the implementation of CNTs in a field-effect transistor layout has been extremely successful.

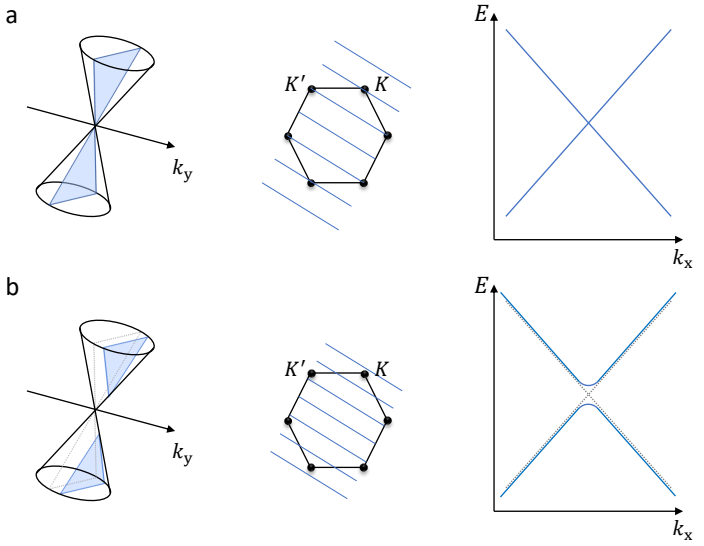

FIGURE 2.3: **Different sub-bands and dispersion curves for two different types of CNT.** The one-dimensional sub-bands together with the energy dispersion are shown for **(a)** metallic and **(b)** semiconducting nanotubes.

2.3 Mechanical properties

As we mentioned, CNTs possess an extraordinary high strength. It originates from the hybridized sp^2 carbon-carbon bonds and can be quantified by the Young Modulus. The low mass density combined with the high stiffness make CNTs an ideal material to implement in electromechanical systems.

The elastic properties of the material are characterized by the Young modulus E and the tensile strength σ_s. The Young modulus accounts for the linear dependence of the stress σ as function of the strain ϵ; in other words, it describes the in-plane strength of the material. The tensile strength refers to the maximum stress that the material can withstand before fracturing or irreversibly deforming. These two values have been experimentally measured in CNTs. The Young modulus in CNTs has been experimentally found in the TPa regime. The Young modulus can be measured: by pulling the two sides of a CNT with AFM tips [62], or by pushing and consequently stretching the CNT with an AFM tip from the top [63], or from thermal vibration measurements using an electronic microscope [64]. In the case of σ_s, it has been determined around few tens of GPa [62].

Chapter 3

Quantum transport in CNT devices

In the following chapter we present the singularities of the electronic transport in nanotube quantum dots. We introduce the relevant energy scales of such a system. Next, we cover the different transport regimes, from regimes like Coulomb-Blockade or Kondo, which are characterized by strong electron correlations, to Fabry-Pérot, where the wave-particle duality of the electrons strongly manifests as quantum interference. The constant interaction model (CI) is used to present the Coulomb-Blockade regime and its figures of merit. Next, we will focus on the the Fabry-Pérot regime, which is relevant for the experiments presented in this work. Finally, we introduce the shot noise in quantum dots, which emanates from the granularity of the electron current.

3.1 Introduction

The bloom of what we know as quantum transport experimental research originated in the 90's due to the improvement in the nanofabrication techniques. Before, the electronic transport in macroscopic systems was well described by the classical treatment of electrons as particles. These improvements on the nanofabrication techniques allowed the scientific community to miniaturize the systems to a dimension smaller than the coherence length of an electron. In these microscopic systems the wave-particle duality of the electrons manifests and different quantum transport phenomena were explored.

A quantum dot defines a zero-dimensional system where the electron wave function is confined in all three directions. The energy of these electrons is quantized as a consequence of the confinement and it can only adopt certain values. The discrete energy spectrum can be observed at room temperature in nanoscale objects but at a temperatures below 1K the confinement can be achieved in micrometer size objects.

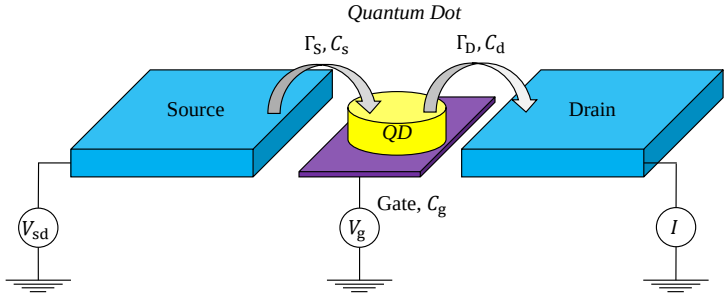

FIGURE 3.1: **Quantum dot schematic.** The quantum dot (QD) is capacitively coupled to the source, the drain, and the gate electrodes through the capacitances C_s, C_d, and C_g. Electrons can tunnel in and out of the quantum dot through the source and drain electrodes. The tunneling is quantified by means of the tunneling rates Γ_S and Γ_D.

Quantum dot devices can be made from various systems such as metallic islands, molecules, nanowires or single wall carbon nanotubes. A quantum dot can be connected to leads consisting of standard metals, ferromagnets or superconducting materials. Finally, its Fermy energy can be tuned by a gate electrode

3.2 Carbon nanotube quantum dots

As we mentioned, quantum dots can be made of carbon nanotubes. If we contact the nanotube ends to a source and a drain electrode and we capacitively couple it to a gate electrode we can achieve the terminal transistor layout (see Fig. 3.1). Because of the finite length of the nanotube, the confinement of the electrons results in quantized energy levels at sufficiently low temperature, so that the system dimension is not longer one but zero. The source and drain electrodes act as reservoirs of electrons that can tunnel into and out of the nanotube. Finally, the gate electrode can tune the electrochemical potential of the quantum dot.

3.2.1 Energy scales

Along with the thermal energy $k_B T$ imposed by the environment, other energy scales define the behaviour of the quantum transport through the quantum dot. We define four different energy scales:

- **Thermal energy:** The thermal energy $k_B T$ refers to the internal energy of the system due to its temperature. The experiments

presented in this work were done in a dilution refrigerator that can reach a temperature of 15 mK. The relevant temperature for quantum transport experiments is the electronic temperature. As we present in Chap. 6, we achieved a minimum electronic temperature of 25 mK. This temperature corresponds to an energy $k_B T_{\mathrm{el}} \approx 2\mu$eV.

- **Charging energy:** This is the Coulomb energy to pay when adding one electron in the quantum dot. It expresses as $E_{\mathrm{c}} = e^2/C_{\mathrm{T}}$, where e is the elemental charge and C_{T} the total capacitance of the quantum dot. C_{T} accounts for the capacitance of the source, drain and gate electrodes $C_{\mathrm{T}} = C_{\mathrm{s}} + C_{\mathrm{d}} + C_{\mathrm{g}}$. The charging energy of nanotube quantum dots is typically between 1 meV to 100 meV.

- **Level spacing energy:** As we previously introduced, the energy levels in a quantum dot are quantized. In a quantum dot with length L, the level spacing is given by the interference condition $\Delta E = \hbar v_F \pi / L$, where v_F represents the Fermi velocity. The level spacing energy of nanotube quantum dots is around few meV.

- **Tunneling rate:** The rate at which the electrodes exchange electrons with the nanotube is known as the tunneling rate. Each electrode has its own tunneling rate: Γ_{S} and Γ_{D} for the source and drain electrodes, respectively. This rate is mainly set by the electronic density of states in the reservoirs and the overlap of the wavefunction of the electrode and the quantum dot. Finally, we usually refer to the tunneling broadening $\hbar\Gamma_{\mathrm{T}} = \hbar(\Gamma_{\mathrm{S}} + \Gamma_{\mathrm{D}})$ which characterises the total coupling between the dot and the reservoirs. It usually takes values from few μeV's to the meV range and, as we will see next, it largely defines the transport regime in the quantum dot.

3.2.2 Transport regimes

The transport regime is determined by the comparison between the energy scales of the system ΔE, E_{c}, $k_{\mathrm{B}}T$, and Γ_{T}.

Coulomb blockade

We here consider that the thermal energy $k_B T$ and the tunnelling rate Γ_{T} are smaller than the level spacing $k_B T, \Gamma_{\mathrm{T}} \ll \Delta E$. On the other hand, the level spacing is usually smaller than or comparable to the charging energy $\Delta E \leq E_{\mathrm{c}}$.

The Coulomb blockade regime is dominated by the Coulomb repulsion between electrons. Once an electron tunnels into the quantum dot, the charge is fixed and no other electron can tunnel into the dot until the electron tunnels out. This regime is characterized by very

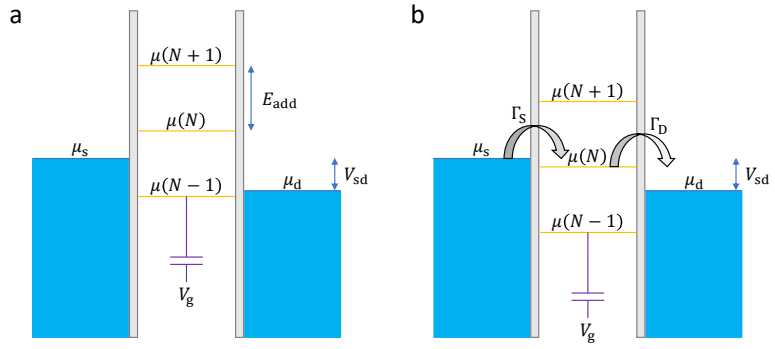

FIGURE 3.2: **Schematic of the energy levels in a quantum dot.** The energy levels are defined through the electrochemical potential μ: The source and drain electrodes are characterized by μ_s and μ_d respectively (the separation between them is defined by eV_{sd}). **(a)** There is no current flowing through the devices. **(b)** The Nth electronic level lays now between μ_s and μ_d and the number of electrons fluctuates between N and $N-1$ setting the conduction through the dot.

opaque tunnel barrier so that the tunnelling rate Γ_T between the dot and the reservoir is very small, resulting in a large lifetime of the electrons inside the dot. Alternatively, it can be also seen as a small energy broadening. The single electron tunneling transport in a CNT quantum dot was reported long time ago in two pioneer works [33, 36].

This regime is characterized by $k_B T \ll E_c$. The temperature has to be low enough in order to avoid thermally induced charge fluctuations in the quantum dot. Additionally, the number of charges inside the system has to be well defined. Therefore, the time Δt to charge or discharge the dot has to be low enough. Starting from the Heisenberg's uncertainty principle $\Delta E \Delta t = E_c \Delta t \geq h$ and knowing that the charge time is given by the RC-time $\Delta t = R_T C_T$, where R_T is the resistance of the tunnelling barrier. There is a minimum value of the resistance $R_T \gg R_K = h/e^2$. Here, $R_K = h/e^2 \approx 25.813\ \mathrm{K\Omega}$ is the Von Klitzing constant.

The constant interaction (CI) model [65] is a simple, yet powerful model to understand the electronic transport in the Coulomb blockade regime. There are two important assumptions that need to be made within the framework of this model. First, the Coulomb interactions among electrons in the dot are captured by a total capacitance C_T. Second, the charging energy is independent of those interactions, therefore it does not depend on the number of electrons in the dot. Considering these assumptions, the total energy of a N-electron dot

$U(N)$ with a source-drain voltage V_{sd} applied on the source, is given by

$$U(N) = \frac{\left(-eN + \sum_{m=1}^{3} C_m V_m\right)^2}{2C_T} + \sum_{n=1}^{N} \epsilon_n, \tag{3.1}$$

where e is the elemental charge, N the number of electrons and V_m and C_m are the applied voltage and the capacitance of the source, drain or gate, respectively. The electrostatic energy is represented by the two first terms of Eq. 3.1. Finally, the last term of Eq. 3.1 accounts for the occupied single-particle energy levels. It is convenient to use the electrochemical potential μ_N which is defined as the minimum energy required to add the Nth electron to the quantum dot $\mu_N = U(N) - U(N-1)$:

$$\mu_N = \frac{e^2}{C_T}\left(N - \frac{1}{2}\right) + e\left(\sum_{m=1}^{3} \alpha_m V_m\right) + \epsilon_N. \tag{3.2}$$

Here, $\alpha_m = C_m/C_T$ is the lever arm of the contact m. The lever arm is very useful since it allows us to convert the applied gate voltage into energy. The electrochemical potential increases while increasing the number of electrons N, creating a ladder structure as shown in Fig. 3.2. The energy needed to add an electron in the system is known as the adding energy $E_{add}(N)$. It takes into account the electrostatic energy E_c and the spacing between the energy levels ΔE:

$$E_{add}(N) = \mu_{N+1} - \mu_N = \epsilon_{N+1} - \epsilon_N + \frac{e^2}{C_T} = E_c + \Delta E. \tag{3.3}$$

When the potential level of the quantum dot lies in the window created between the electrochemical potential of the source (μ_s) and the drain (μ_d) we observe electronic transport. When the electrochemical potential of the quantum dot follows the hierarchy $\mu_s > \mu > \mu_d$, where $-eV_{sd} = \mu_s - \mu_d$, an electron typically tunnel into the dot from the source and then tunnel out to the drain (as shown in Fig. 3.2(b)). A second electron can tunnel onto the dot but only after that the first electron has tunneled out. This effect is known as single-electron tunneling.

Since the size of a quantum dot is small, the capacitance is also very small and consequently the charging energy takes large values. If the energy level of the dot remains out of the window defined by the electrochemical potential of source and drain, the quantum dot electron number is fixed and there is no current flowing through it. This is the so-called Coulomb Blockade.

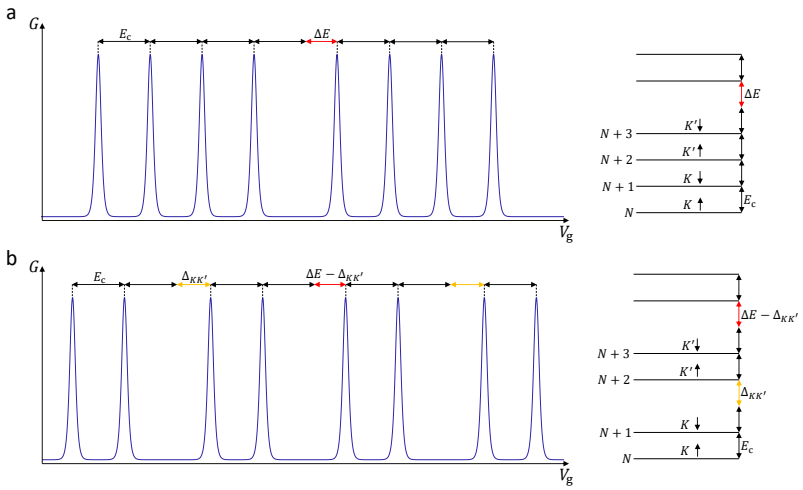

FIGURE 3.3: **Schematic representation of the quantum dot conductance G and the corresponding energy levels.** G is represented as function of the gate voltage V_g together with the corresponding schematic of the energy level distribution for one electronic shell in two different cases: **(a)** The electronic shell contains four electrons due to the valley and the spin degeneracy.**(b)** In this case there is a two-fold symmetry due to the spin degeneracy while there is a lifting due to the valley degeneracy.

In Fig. 3.3, by sweeping the gate voltage V_g and measuring the current, we obtain traces with regular peaks. This peaks represent the situation where an energy level falls in the bias window leading to single-electron tunneling current. The region between the peaks stands for the case where the number of electrons in the dot is fixed and there is not current flowing through it. ΔE can be extracted from the separation between the current peaks as described in Fig. 3.3. In the case of valley and spin degeneracy there is a fourfold degeneracy, as depicted in Fig. 3.3(a). In the case that the valley degeneracy is lifted, the periodicity changes as shown in Fig. 3.3(b). The lifting of the valley degeneracy may be caused by the scattering at the electrodes which creates a mismatch between the two valleys in the carbon nanotube band-structure.

When increasing the source-drain voltage one or more excited states can enter into the window defined by V_{sd}. The electron can tunnel either through the ground or the excited state increasing the total current.

In the so-called Coulomb Blockade diamond measurement. The differential conductance G_{diff} is measured while sweeping V_{sd} and V_g,

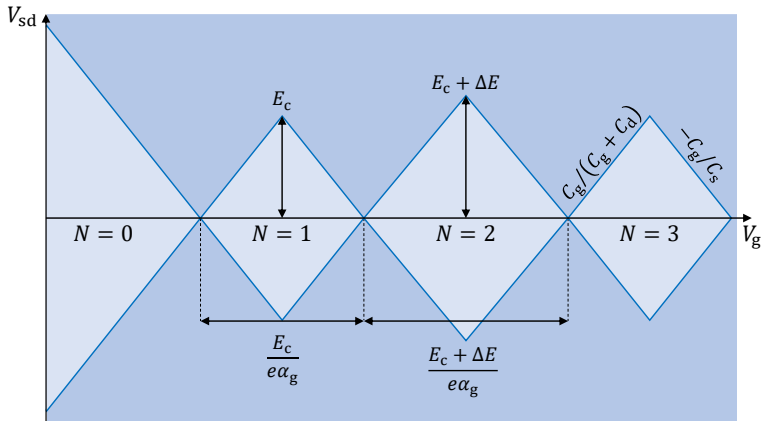

FIGURE 3.4: **Charge stability diagram schematic.** The differential conductance G_{diff} is shown as a function of the source-drain voltage V_{sd} and the gate voltage V_g for a system with spin degeneracy but without the valley degeneracy. The blue lines represent the evolution of the conductance peaks represented in Fig.3.3(b). The surfaces inside these lines (light blue) are the so-called Coulomb Diamond regions where the transport is not allowed because the charge in the system is fixed (the number of charges is depicted as N). The blue lines can be used to extract the important energies of the system (E_c and ΔE). The number of electrons outside the diamond-shaped regions (dark blue) can fluctuate since more allowed states enter in the bias window.

as shown in Fig. 3.4. Inside the diamond-shaped regions (light blue) the number of electrons is fixed and no current is measured. The addition energy E_{add} can be directly read from such a measurement.

As we mentioned before, two Coulomb peaks at zero bias are spaced by $\frac{E_{add}}{e\alpha_g}$. The height of the Coulomb Diamonds corresponds to $eV_{sd} = E_{add}$ and the slopes of the diamonds are given by the capacitances of the device. The positive slope of the Coulomb diamond is $s_+ = \frac{C_g}{C_g+C_d}$ (when the drain electrode is grounded) while the negative one is $s_- = -\frac{C_g}{C_s}$. The gate lever-arm can be determined from these slopes as $\alpha_g = \frac{1}{|s_+|+|s_-|}$.

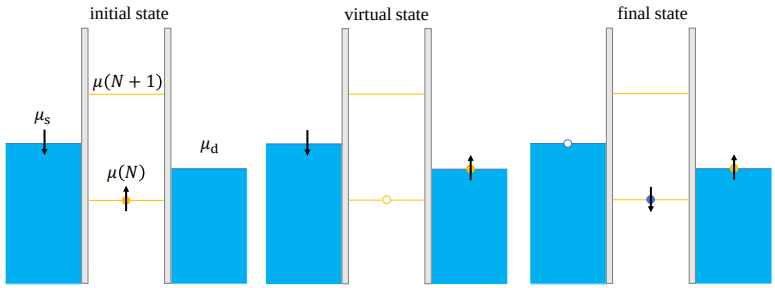

FIGURE 3.5: **Spin-flip co-tunnelling.** The spin up electron in the dot jump out to be replaced by a spin down electron leading to a final state in which the spin of the electron in the dot changed its sign. The spin in the dot is coupled to the spins in the electrode, forming a spin singlet.

Kondo regime

In this regime the thermal energy $k_B T$ is clearly smaller than the tunnelling rate $k_B T < \Gamma_T$. The rest of the energy scales follows the same hierarchy as that in the Coulomb Blockade case $\Gamma_T < \Delta E \leq E_c$.

When the dot becomes more transparent and the resistance approaches R_K, high-order processes need to be taken into account. Therefore, quantum fluctuations are observed in the electron number even in the Coulomb Blockade regime.

The conductance is given by elastic cotunneling processes [66]. In this high-order process, an electron can tunnel out the dot, leaving it temporarily in a classically forbidden state known as a virtual state. This process is allowed by the Heisenberg uncertainty principle if another electron immediately tunnels into the dot. In conclusion, the initial and final energy are the same but an electron has been transported through the dot.

The spin of the electron plays a central role. The initial energy state must have a spin and the final state has a spin that may be in the other direction. As a consequence, the net spin of the dot may be flipped during the event as depicted in Fig. 3.5. The spins of the electrons in the dot and the reservoirs are entangled. Therefore, there is a new ground state of the system as a whole spin singlet. The spins in the dot is screened by the spins of the electrons in the reservoir.

The Kondo effect in quantum dots was reported for the first time in 1998 [67, 68]. Later, this effect was also observed in carbon nanotube SETs [37].

There are various effects in transport measurements associted with the Kondo effect. First, there is an even-odd asymmetry in the gate voltage dependence of the conductance. When we have an even number of electrons in the dot the net spin is zero, while when we have

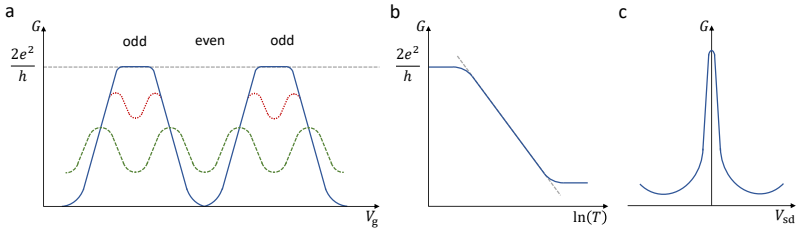

FIGURE 3.6: **Schematic of some of the main features of the Kondo effect in a CNT quantum dot. (a)** Schematic of the conductance G as function of the gate voltage V_g in three different cases: $T \ll T_K$ green line, $T \leq T_K$ red line, and $T \gg T_K$ blue line. **(b)** Schematic of the conductance G as function of the temperature T. G decreases logarithmically by increasing the temperature when the number of electrons is odd. **(c)** Schematic of the zero-bias Kondo resonance known as Kondo ridge.

an odd number the total spin is non-zero, resulting in the Kondo effect. Upon lowering the temperature, the conductance decreases in the even case, while is increases in the odd case. Second, the conductance in the middle of the Kondo valleys increases logarithmically by reducing the temperature until the saturation point $2e^2/h$ at the lowest temperature 3.6(b). This value corresponds to the so-called unitary limit of conductance [69]. This situation is equivalent to a completely transparent quantum dot. Usually we expect that charging effects and the tunnel barriers block the electron tunneling but in the Kondo regime the electrons can tunnel in an unimpeded way. Third, the conductance has a zero-bias resonance in the conductance G due to the Kondo resonance at the Fermi energy of the reservoirs 3.6(c), this feature is also known as Kondo ridge. The full-width half maximum of the resonance gives an estimation of T_K.

We present measurements showing signatures of the Kondo effect in Chap. 7 and Chap. 8.

Fabry-Pérot interference

The Fabry-Pérot regime is characterized by a high tunnelling rate Γ_T so that $k_B T, E_c \ll \Gamma_T$. In this case, Γ_T can approach the level spacing $\Gamma_T \leq \Delta E$.

This regime is characterized by transparent barriers. Electrons can tunnel in and out of the quantum dot fast enough so the charging effects are no longer dominant. The dot is considered open and interference phenomena becomes relevant. The right- and left-moving electron waves scatter at the interfaces with the reservoirs creating an effect analogous to the optical Fabry-Pérot interferometer (see

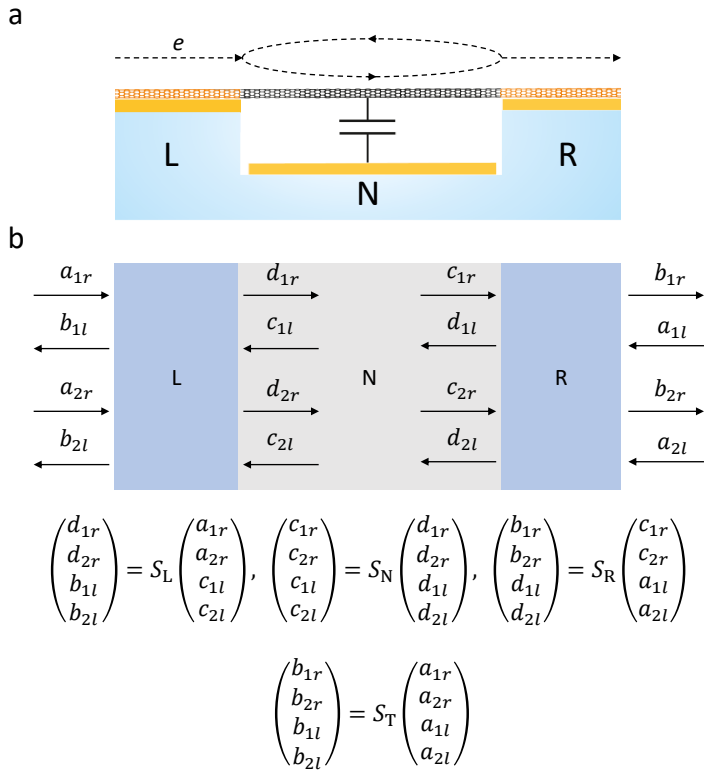

FIGURE 3.7: **Fabry-Pérot regime in a coherent electron-waveguide. (a)** Schematic of the device illustrating that the multiple electron reflections give rise to an interference pattern. **(b)** A diagram of the basis wavefunctions used to define the scattering matrices S_{L}, S_{R}, S_{N}, and S_{T}.

Fig. 3.7(a)). The characteristic interference pattern of transport measurements in this regime is explained by the modulation of the wave number k of electrons by sweeping V_{g} and V_{sd}. Analogous to the optical cavity case, where the transmitted intensity is also modulated, the period of the modulation is inversely proportional to the length L of the electron cavity.

In this type of devices, the carbon nanotube acts as a coherent electron-waveguide, where the resonant cavity is created between the two nanotube-reservoir interfaces. Therefore, the current is carried by two spin-degenerate, one-dimensional transport modes with linear dispersion. the maximum expected value of G, corresponding to two transport channels, is $4e^2/h$ when the electrons move ballistically through the conductor.

We present a simple theoretical framework based on a scattering

matrix approach to describe transport in the Fabry-Pérot regime [70–72]. In this model, 4x4 scattering (S) matrices characterize the electron transmission and reflection at each interface, S_L and S_R for the left (source) and right (drain) interfaces. The matrix that describes the transmission through the CNT is denoted as S_N. The basis wave functions that describe the system are outlined in Fig. 3.7(b). We define the transmission matrix S_T as the combination of the three different scattering matrices of the system.

$$S_T = S_L \otimes S_N \otimes S_R. \tag{3.4}$$

The generalized matrices of both interfaces can be written in terms of four submatrices of finite order:

$$S_{L,R} = \begin{pmatrix} S^{11}_{L,R} & S^{12}_{L,R} \\ S^{21}_{L,R} & S^{22}_{L,R} \end{pmatrix}, \tag{3.5}$$

where $S^{ij}_{L,R}$ are 2x2 submatrices that take into account the transmission and reflection at the interfaces. For the sake of simplicity, we will ignore the inter-mode mixing between the channels. The matrices $S^{12/21}_{L,R}$ can be described by a diagonal matrix:

$$S^{12/21}_{L,R} = \begin{pmatrix} r_{L,R} & 0 \\ 0 & r_{L,R} \end{pmatrix}, \tag{3.6}$$

here $r_{L,R}$ represent the reflection coefficients of each interface.

We also define the transmission part of the scattering matrix $S^{11/22}_{L,R}$ as a diagonal matrix:

$$S^{11/22}_{L,R} = \begin{pmatrix} t_{L,R} & 0 \\ 0 & t_{L,R} \end{pmatrix}, \tag{3.7}$$

where $t_{L,R}$ are the transmission coefficients of each interface.

The phase of the electronic wave function changes as a function of the gate voltage and the source-drain voltage. It leads to the interference pattern. It is important to mention that the two propagating modes in a carbon nanotube possess different wave vectors $\vec{k_1}$ and $\vec{k_2}$, which is the most important difference with respect to the single-mode optical cavity. The matrix S_N is also diagonal in absence of electron

scattering between the two modes in the nanotube:

$$S_{\mathrm{N}} = \begin{pmatrix} S_{\mathrm{N}}^{11} & 0 \\ 0 & S_{\mathrm{N}}^{22} \end{pmatrix} = \begin{pmatrix} e^{i\phi_1} & 0 & 0 & 0 \\ 0 & e^{i\phi_2} & 0 & 0 \\ 0 & 0 & e^{i\phi_1} & 0 \\ 0 & 0 & 0 & e^{i\phi_2} \end{pmatrix}, \tag{3.8}$$

where $S_{\mathrm{N}}^{11} = S_{\mathrm{N}}^{22} = S_{\mathrm{N}}^{0}$ and ϕ_1 and ϕ_2 account for the phase accumulated by the electrons corresponding to the two modes, respectively.

The matrix S_{T} can by calculated from the matrices S_{N}, S_{R} and S_{L} by matrix combination [70–72]. We write the generalized expression for the submatrix S_{T}^{11} which contains the transmission coefficients.

$$\begin{aligned} S_{\mathrm{T}}^{11} &= S_{\mathrm{L}}^{22} S_{\mathrm{N}}^{0} (\mathbb{1} - S_{\mathrm{R}}^{12} S_{\mathrm{N}}^{0} S_{\mathrm{L}}^{21} S_{\mathrm{N}}^{0})^{-1} S_{\mathrm{R}}^{22} = \\ &= \begin{pmatrix} t_T^{11} & t_T^{12} \\ t_T^{21} & t_T^{22} \end{pmatrix} = \begin{pmatrix} \frac{t_{\mathrm{L}} t_{\mathrm{R}} e^{i\phi_1}}{1 - r_{\mathrm{L}} r_{\mathrm{R}} e^{2i\phi_1}} & 0 \\ 0 & \frac{t_{\mathrm{L}} t_{\mathrm{R}} e^{i\phi_2}}{1 - r_{\mathrm{L}} r_{\mathrm{R}} e^{2i\phi_2}} \end{pmatrix}. \end{aligned} \tag{3.9}$$

The total transmission of the system can be expressed as

$$T = \sum_{i,j=1,2} \left| t_T^{ij} \right|^2. \tag{3.10}$$

The values of t_T^{ij} correspond to the different elements of the matrix S_{T}^{11} defined in Eq. 3.9. Finally, we can write G in terms of Eq. 3.10

$$\begin{aligned} G &= \frac{4e^2}{h} \sum_{i,j=1,2} \left| t_T^{ij} \right|^2 = \\ &= \frac{4e^2}{h} \sum_{i=1,2} \frac{|t_{\mathrm{L}}|^2 |t_{\mathrm{R}}|^2}{1 + |r_{\mathrm{L}}|^2 |r_{\mathrm{R}}|^2 - 2 |r_{\mathrm{L}}| |r_{\mathrm{R}}| \cos(2\phi_i(V_{\mathrm{g}}, V_{\mathrm{sd}}))} \end{aligned} \tag{3.11}$$

An example of an oscillating pattern is presented in Fig. 3.8. We numerically simulated G as function of V_{g} at zero bias using Eq. 3.11. We assumed symmetric and transparent interfaces. We also calculated $\phi_{1,2}$ using the standard experimental parameters in our CNT quantum dots [41]. The oscillation representative of the Fabry-Pérot interference pattern is captured by this model although we would need a more elaborated model to describe other effects such as the secondary oscillations as observed in previous studies on ultraclean CNTs [42, 73]. We present detailed measurements in Chap. 7 and Chap. 8.

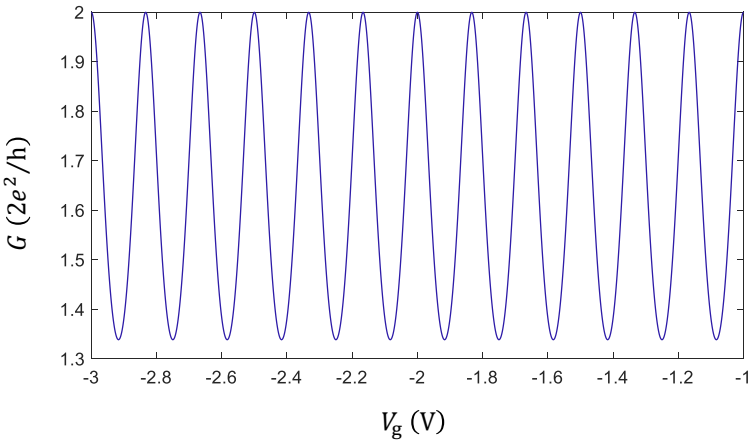

FIGURE 3.8: **Conductance oscillations in the Fabry-Pérot regime.** Calculation of the conductance G as function of the gate voltage V_g in a CNT quantum dot with almost perfectly transparent and symmetric barriers using Eq. 3.11. The phase ϕ has been calculated following the work of Liang and coworkers [41].

3.3 Noise in a quantum dot

We define the noise in our system as the random fluctuations over time of a physical quantity around its mean value. For example, if we consider the current $\mathrm{I}(t)$[1], its fluctuations from the average value are defined as $\delta\mathrm{I}(t) = \mathrm{I}(t) - \langle \mathrm{I}(t) \rangle$. Therefore, the autocorrelation function $G_\mathrm{I}(\tau)$ is

$$G_\mathrm{I}(t,\tau) = \langle \mathrm{I}(t)\mathrm{I}(t+\tau)^* \rangle = \int_{-\infty}^{\infty} \mathrm{I}(t)\mathrm{I}(t+\tau)^* dt, \tag{3.12}$$

where $\langle \mathrm{I}(t) \rangle$ is the statistical average and $\mathrm{I}(t)^*$ is the complex conjugate of $\mathrm{I}(t)$. The Wiener-Kinchin theorem states that the autocorrelation function of $\mathrm{I}(t)$ is the Fourier transform pair of its power spectral

[1] We use the convention $\mathrm{I}(\omega) = \int_{-\infty}^{\infty} \mathrm{I}(t) e^{i\omega t} dt$. and $\mathrm{I}(t) = \frac{1}{2\pi} \int_{-\infty}^{\infty} \mathrm{I}(\omega) e^{i\omega t} d\omega$

density (PSD)[2]. The double-sided PSD $S_{\mathrm{II}}^{\mathrm{d}}(\omega)$ is defined as

$$S_{\mathrm{II}}^{\mathrm{d}}(\omega) = \int_{-\infty}^{\infty} \langle \mathrm{I}(t)\mathrm{I}(t+\tau)^* \rangle e^{i\omega t} d\tau. \tag{3.13}$$

In the classical limit, the autocorrelation function is symmetric in time $G_{\mathrm{I}}(t) = G_{\mathrm{I}}(-t)$. Consequently, the PSD is also symmetric in frequency $S_{\mathrm{II}}(\omega) = S_{\mathrm{II}}(-\omega)$ for a frequency range far from the quantum limit $\hbar\omega \gg k_B T$. The PSD detected experimentally in this work is what is considered as the classical PSD.

We introduce the main sources of noise in the system:

- $1/f$ **noise:** The origin of this noise in electronic devices emanates from the slow current fluctuations due to the small changes in the device properties. It is present in every material and its value is proportional to the current but decays inversely with the frequency. It was first reported by J. B. Johnson [74] and was described by W. Schottky [75].

  In order to avoid this noise we built a measurement setup whose characteristic frequency is in the MHz range. We present the details of the measurement scheme in Chap. 5.

- **Thermal noise:** The thermal noise originates from the finite temperature of the system. The number of charges may fluctuate due to the thermal fluctuations leading to voltage and current fluctuations when the system is in equilibrium $V_{\mathrm{sd}} = 0$.

  This noise is known as the Johnson-Nyquist noise. It was first reported by J. B. Johnson [76] and its theoretical framework was develop by H. Nyquist [77]. The mathematical expression can be directly derived from the fluctuation-dissipation theorem as

  $$S_{\mathrm{VV}} = 4K_B T R. \tag{3.14}$$

  Thermal noise is frequency independent up to the quantum limit (white noise). We use the Jonhson-Nyquist noise as a thermometer in Chap. 6.

  The displacement in a suspended carbon nanotube quantum dot also fluctuates due to the finite temperature as we show in Chap. 4.

[2] We need to clarify that S_{II} corresponds to the single-sided PSD which contains only information of the positive frequency components. The double-sided PSD $S_{\mathrm{II}}^{\mathrm{d}}$ contains both components and it relates with the single-sided PSD as $S_{\mathrm{II}}(\omega > 0) = 2S_{\mathrm{II}}^{\mathrm{d}}(\omega > 0)$. Through this thesis we refer to the single-sided PSD since our experimental equipment directly outputs it.

- **Quantum noise:** When the frequency is above the limit $\hbar\omega \gg k_B T$, the PSD is not symmetric. Therefore, in this regime the absorbed and emitted noise is no longer the same (see the introduction to the quantum noise by Schoelkopf and coworkers in Ref. [78]). The zero point fluctuations (zpf) of the nanotube are responsible of this noise. Since we work in the few MHz regime we do not need to take into account its contribution.

- **Shot Noise:** The system moves out of equilibrium when a V_{sd} is applied and is larger than $k_B T$. Since the current consists of a flow of discrete charges, it creates current fluctuations. It was described by Schottky [75].

  The shot noise, based on the assumption that the statistics of electrons passage is Poissonian, reads

$$S_{II} = 2e\langle I\rangle. \tag{3.15}$$

  In phase coherent electron devices, the shot noise can be finite. The Fano factor is then defined as

$$F = \frac{S_{II}}{2e\langle I\rangle}. \tag{3.16}$$

  It was first introduced by Fano [79]. In the Coulomb Blockade regime, the shot noise is suppressed a facor two in a double barrier quantum dot [80, 81], leading to a Fano factor $F \approx 1/2$. While in a quantum point contact, where the conductance is maximum $G = 2e^2/h$, the transport can become noiseless [82]. We can find that in this case, F goes to zero at the position of the quantized conductance plateaus, where the quantum channels are fully transmitting. In addition, in some materials the shot noise gives information on the charge carriers: For instance, in a hybrid system based in a superconductor material, the shot noise is twice as large compared to that in the normal metal phase since the charge is carried by a Copper pair $q = 2e$ [83].

  In Chap. 6, we will expand the shot noise theory in order to calculate the total contribution of the shot noise together with the thermal noise in the current PSD. We use it as a thermometer to determine the electronic temperature of the carbon nanotube quantum dot.

Chapter 4

Basics of nanomechanical resonators

We provide the theoretical framework needed to understand the mechanical behaviour of the carbon nanotube resonators presented in this work. We first introduce the simplest model, the linear harmonic oscillator. Two scenarios are presented, one to describe the response to an external linear driving force and the second to describe the Brownian thermal motion. We follow with the non-linear description of the oscillator. Then, we model the carbon nanotube as a double clamped beam. Finally, we present the backaction effects and their fundamental limitation in a carbon nanotube electro-mechanical resonator.

4.1 The linear harmonic oscillator

The linear harmonic oscillator represents the simplest model of a carbon nanotube electro-mechanical resonator. This model captures the basic features of a mechanical system with an arbitrary geometry. We first study for simplicity the case where no external driving is applied and there is no damping. Next, we introduce the equation of motion for the general case of a damped resonator. The system is described by the Hooke's law

$$F(t) = -kz(t), \tag{4.1}$$

where k is the spring constant and $z(t)$ represents the vertical displacement in the time domain. According to the Newton's second law the restoring force F has to be equal to the effective mass m_{eff} multiplied by the acceleration of the system $\ddot{z}(t)$, $F = m_{\text{eff}}\ddot{z}(t)$. The equation of motion for such a system is

$$m_{\text{eff}}\frac{d^2z}{dt^2} + kz(t) = 0. \tag{4.2}$$

The solution of Eq. 4.2 takes the form of $z(t) = z_0 \exp(-i\omega_0 t + i\phi)$. Where ω_0 is the angular mechanical resonant frequency and z_0 and ϕ are the amplitude and phase of the motion, respectively. The resonant frequency is given by $\omega_0 = \sqrt{k/m_{\text{eff}}}$. In a more realistic case the damping, or friction, slows down the motion of the mechanical oscillator. Therefore, in addition to the restoring force there is a force due to the friction proportional to the velocity $\dot{z}(t)$, $F_{\text{fric}} = m_{\text{eff}}\Gamma_0\dot{z}(t)$. The equation of the motion of a damped oscillator reads as

$$m_{\text{eff}}\frac{d^2z}{dt^2} + kz(t) + m_{\text{eff}}\Gamma_0\frac{dz}{dt} = F(t). \tag{4.3}$$

The linear mechanical damping is quantified by Γ_0. $F(t)$ acts as an additional external time dependent force that drives the system (this case is further discussed below).

The quality factor Q which accounts for the interaction with the environment is considered an important figure of merit in the field of mechanical oscillators.

$$Q = 2\pi\left(\frac{\text{Total energy}}{\text{Energy lost per cycle}}\right). \tag{4.4}$$

In the approximation of small losses, $\Gamma_0 \ll \omega_0$, the quality factor can be approximated as $Q = \omega_0/\Delta\omega_0$.

For convenience we usually work in the frequency domain instead of the time domain. Therefore, we need to perform the Fourier transform on Eq. 4.3. We rewrite it as

$$z(\omega) = \chi(\omega)F(\omega), \tag{4.5}$$

where χ is the mechanical susceptibility which reads as

$$\chi(\omega) = \frac{1}{m_{\text{eff}}\left(\omega_0^2 - \omega^2 - i\Gamma_0\omega\right)}. \tag{4.6}$$

Equation 4.5 describes the linear response of the mechanical resonator in the frequency domain. From the experimental point of view, we work with the power spectral density (PSD) of the noise in the displacement, which reads

$$S_{zz}(\omega) = |\chi(\omega)|^2 S_{\text{FF}}(\omega). \tag{4.7}$$

$S_{\text{FF}}(\omega)$ is the PSD of the external force acting on the mechanical resonator. It can have different origins as we will develop further below.

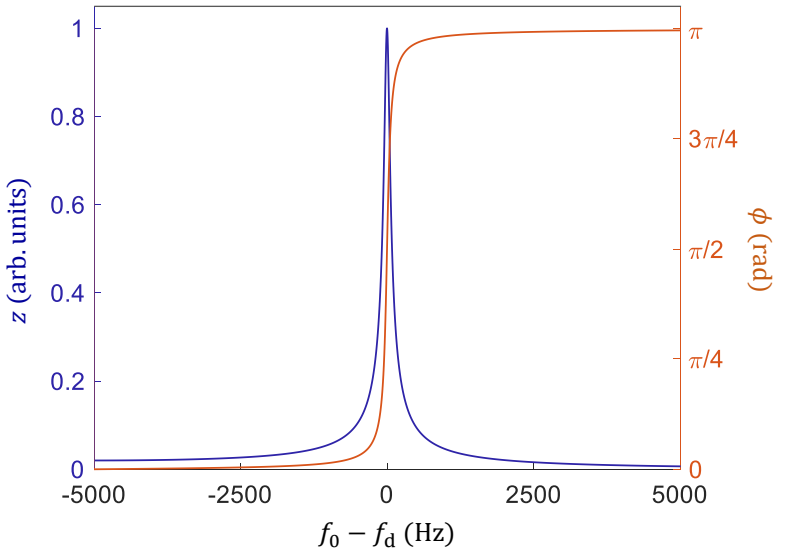

FIGURE 4.1: **Amplitude and phase of the motion for an harmonic oscillator coherently driven.** The amplitude of motion is maximized when the driving signal and the mechanical oscillator are in resonance ($\omega_0 = \omega_d$). The motion is then $\pi/2$ dephased with respect to the driving force.

4.1.1 Coherent driving

First, we present the case in which the external force $F(t)$ is a coherent sinusoidal driving force

$$F(t) = F_d \cos(\omega_d t), \tag{4.8}$$

where F_d is the amplitude of the driving force and ω_d is the frequency of the drive tone. Using Eq. 4.3, the displacement and the phase in the frequency domain take the following form

$$z(\omega_d) = \frac{F_d}{m_{eff}} \frac{1}{\sqrt{(\omega_0^2 - \omega_d^2)^2 + (\Gamma_0 \omega_d)^2}}, \tag{4.9}$$

$$\phi(\omega_d) = \arctan\left(\frac{\Gamma_0 \omega_d}{\omega_0^2 - \omega_d^2}\right). \tag{4.10}$$

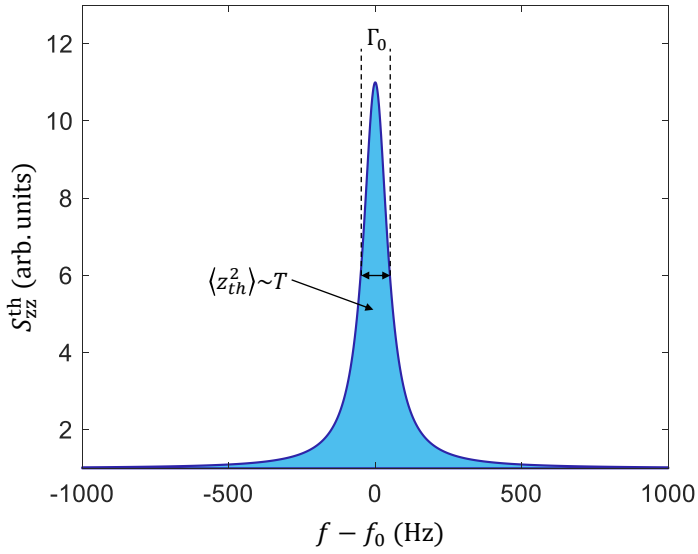

FIGURE 4.2: **Thermal displacement power spectral density for an harmonic oscillator.** The thermal displacement PSD following Eq. 4.13 is represented as a function of the frequency. The area below the curve corresponds to the variance of the displacement of the harmonic oscillator which is directly linked with its temperature through the equipartition theorem.

Analysing Eq. 4.9 and Eq. 4.10, we see that the amplitude $z(\omega_d)$ maximizes when the driving tone in resonance with the mechanical oscillator. At this point the phase corresponds to $\phi(\omega_d) = \pi/2$. The specific shape of $z(\omega_d)$ and $\phi(\omega_d)$ are depicted as a function of f_d in Fig. 4.1.

4.1.2 Incoherent driving

The external drive can also take an incoherent form. It can simply be caused by the energy exchange with the environment. We previously saw that the interaction with the environment is quantified by the factor Q. The coupling with the environment also manifests as a fluctuating driving force which leads to the well-known Brownian motion. This effects is well explained by the fluctuation-dissipation theorem [84], which states that in thermal equilibrium, the losses of the resonator are related to the external fluctuating thermal forces acting on it.

Using the linear response theory in the framework of the fluctuation-dissipation theorem [85, 86], the PSD of the single-sided thermal force noise is expressed as

$$S_{\mathrm{FF}}^{\mathrm{th}}(\omega) = -\frac{4k_BT}{\omega} Im\left(\frac{1}{\chi(\omega)}\right), \tag{4.11}$$

where k_B is the Boltzmann constant and T the temperature of the mechanical resonator. We can approximate $S_{\mathrm{FF}}^{\mathrm{th}}(\omega)$ classically (in the approximation of small losses) as

$$S_{\mathrm{FF}}^{\mathrm{th}}(\omega) = 4k_BTm_{\mathrm{eff}}\Gamma_0. \tag{4.12}$$

We see that $S_{\mathrm{FF}}^{\mathrm{th}}(\omega)$ is independent of the frequency.

We can calculate the PSD of the mechanical resonator's thermal displacement using Eq. 4.7 as,

$$S_{zz}^{\mathrm{th}}(\omega) = \frac{4k_BT\Gamma_0}{m_{\mathrm{eff}}[(\omega_0^2-\omega^2)^2+(\Gamma_0\omega)^2]}. \tag{4.13}$$

We now focus in the mean energy U. In thermal equilibrium, the mean energy of a linear harmonic oscillator reads

$$U = \frac{1}{2}m_{\mathrm{eff}}\langle \dot{z}_{th}^2\rangle + \frac{1}{2}k\langle z_{th}^2\rangle = k_BT, \tag{4.14}$$

where the first term accounts for the kinetic energy and the second one for the potential energy. The average energy U is equal to the thermal energy k_BT in the approximation where the thermal energy is bigger than the phonon energy, $k_BT \gg \hbar\omega$. Following the equipartition theorem for a harmonic oscillator, the contribution of the kinetic energy must be equal to the contribution of the potential energy. Therefore, we have that $\frac{1}{2}m_{\mathrm{eff}}\langle \dot{z}_{th}^2\rangle = \frac{1}{2}k\langle z_{th}^2\rangle = \frac{1}{2}k_BT$.

$$\langle z_{th}^2\rangle = \frac{k_BT}{m_{\mathrm{eff}}\omega_0^2} = \int_0^\infty \frac{1}{2\pi} S_{zz}^{\mathrm{th}}(\omega)d\omega. \tag{4.15}$$

We also know that the variance of the displacement $\langle z_{th}^2\rangle$[1] corresponds to the area under the curve represented by the Eq. 4.13. Accordingly, we can estimate the mode temperature of the mechanical oscillator by integrating the PSD (see Fig. 4.2).

[1] In the following chapters, we refer to the variance of the displacement $\langle z_{th}^2\rangle$ as δz^2.

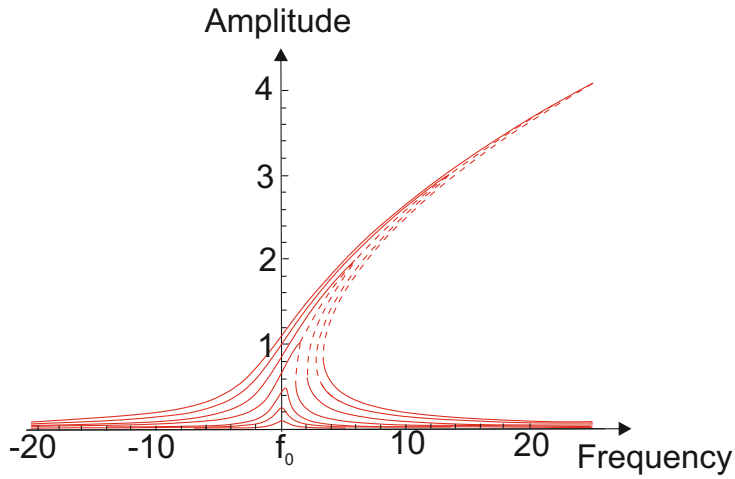

FIGURE 4.3: **Nonlinear response of the amplitude of motion as a function of driving frequency for a Duffing resonator.** Different curves correspond to different driving forces (adapted from [87]).

Finally, its important to mention that the thermal occupation n of a mechanical mode at a frequency ω and T is defined by the Bose-Einstein distribution:

$$n = \frac{1}{e^{\left(\frac{\hbar\omega}{k_B T}\right)} - 1}. \tag{4.16}$$

Equation 4.16 allows us to quantify how far is the mechanical oscillator from the ground state, as we show in Chap. 8.

4.2 The nonlinear harmonic oscillator

The linear harmonic oscillator is a good approximation for small amplitude vibrations which involve linear restoring forces. When driving the resonator to large amplitude vibrations, nonlinear restoring forces become sizeable converting a linear harmonic oscillator into the so-called Duffing resonator. Carbon nanotube electro-mechanical resonators possess a small dynamical range which leads to the appearance of nonlinearities at comparatively small displacements [88]. These nonlinear restoring forces can originate, for example, from geometrical reasons, external nonlinear potentials, the way the resonator

is clamped or the actuation and the detection mechanism used to interact with the resonator [87]. In order to correctly describe the motion of such a resonator, we need to introduce an additional term in the equation of motion. This additional term is proportional to the cubic displacement of the mechanical oscillator so that the equation of motion is

$$m_{\text{eff}}\frac{d^2z(t)}{dt^2} + kz(t) + m_{\text{eff}}\Gamma_0\frac{dz(t)}{dt} + \alpha z^3(t) = F(t), \tag{4.17}$$

where α is the Duffing nonlinear constant. In the limit of small amplitude, the driven amplitude $z(\omega_{\text{d}})$ can be calculated as

$$z(\omega_{\text{d}}) \approx \frac{F(t)}{2m_{\text{eff}}\omega_0^2}\frac{1}{\sqrt{\left(\frac{\omega_{\text{d}}-\omega_0}{\omega_0} - \frac{3}{8}\frac{\alpha}{m_{\text{eff}}\omega_0^2}z^2\right)^2 + (2Q)^{-2}}}. \tag{4.18}$$

If we look closely to Eq. 4.18, we can see that above a certain amplitude there are three possible solutions and two of them are stable. Therefore, a bistable and hysteretic behaviour is expected when sweeping the frequency of the driving tone. The behaviour of the amplitude is represented in Fig. 4.3. The amplitude of motion as a function of the driving frequency is well described by a Lorentzian function for small driving forces only. Above a threshold, the resonant frequency shifts to higher or lower frequency depending on the sign of the α constant. We could also consider the non-linear dissipation, which is present in carbon nanotube resonators [89]. It often appears in the damping mechanisms that accompany every mechanical resonator. This effect has been modelled as a term $\nu z^2(t)\frac{dz(t)}{dt}$, where ν is a constant. This new term modifies the $z(\omega_{\text{d}})$ response and it decreases the magnitude of the response when it is appreciable. Therefore, the responsivity is decreased as the driving amplitude is increased in the presence of nonlinear damping.

In Chap. 8 signatures of self-sustained motion of a carbon nanotube resonator are presented. This regime depends on the nonlinear response of the mechanical resonator.

4.3 Euler-Bernoulli beam theory

We describe now the mechanical properties of a double clamped beam using the continuum mechanics to describe a carbon nanotube electromechanical resonator. Specifically, we focus on the Euler-Bernoulli beam theory which is a simplification of the theory of elasticity [90].

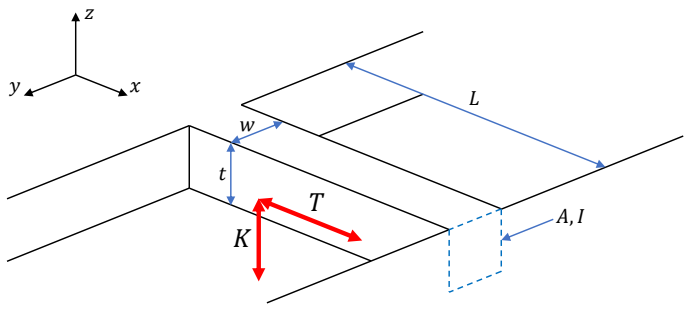

FIGURE 4.4: **Schematic of the modelling of the CNT as a double clamped beam in the Euler-Bernoulli beam theory framework.** The beam deflects in the z axis, and it has dimensions $Lx\omega xt$, cross-section area A and moment of inertia I. It is under a load K and tension $\vec{T}$.

We simplify the nanoresonator as a double clamped beam made of an isotropic and linear elastic material as shown in Fig. 4.4. The coordinate system defines x along the direction of the beam and y, z perpendicular to it. We assume that the cross-section A is symmetric and the forces are applied in the z direction. In this model we only consider the flexural modes of vibration. We only consider the displacement in the z axis. Therefore the problem reduces to two dimensions

We first solve the Euler-Bernoulli equation which allows us to understand the motion of the resonator. The spring constant may be affected by the changes of the tension (as we present in Chap. 8).

We look at the energy of the mechanical resonator. This energy has various contributions, for example, the elastic energy of the beam U_{elas}. It accounts for the energetic contribution of the bending and the elongation effects. It reads as

$$U_{\text{elas}} = \frac{1}{2}\int_0^L \left(EI\left(\frac{\partial^2 z}{\partial x^2}\right)^2 + \left(T_0 + \frac{EA}{2L}\int_0^L \left(\frac{\partial z}{\partial x}\right)^2 dx \right)\left(\frac{\partial z}{\partial x}\right)^2 \right) dx. \tag{4.19}$$

E denotes the elastic modulus of the material, I is the moment of inertia and L corresponds to the length of the beam. The first term of the integral accounts for the flexural rigidity and the second one corresponds to the extensional rigidity. The total tension T is divided into the built-in tension T_0 and an additional term accounting for the

tension induced by the displacement.

$$T = T_0 + \frac{EA}{2L} \int_0^L \left(\frac{\partial z}{\partial x}\right)^2 dx. \tag{4.20}$$

We also need to consider the kinetic energy of the resonator U_{kin}.

$$U_{\text{kin}} = \frac{1}{2} \int_0^L \rho A \left(\frac{\partial z}{\partial t}\right)^2 dx, \tag{4.21}$$

where ρ is the mass density. Finally, we need to take into account and external force K in the z direction. Its energetic contribution is expressed as $U_{\text{force}} = \frac{1}{2}\int_0^L Kz dx$. Finally, the total energy that accounts for all these three contributions reads as

$$U_{\text{total}} = \frac{1}{2} \int_0^L \left(\rho A \dot{z}^2 + EIz''^2 + Tz'^2 + Kz\right) dx, \tag{4.22}$$

here z'' is the second derivative of z with respect to x, z' the first derivative with respect to x and $\dot{z}$ the first derivative with respect to t.

We now proceed to calculate the equation of motion through the Lagrangian of the system:

$$\mathcal{L} = \frac{1}{2}\left(\rho A \dot{z}^2 - EIz''^2 - Tz'^2 + Kz\right). \tag{4.23}$$

Knowing the Lagrangian of the beam, we can solve the Euler-Lagrange equation to find the equation of the motion.

$$\frac{\partial \mathcal{L}}{\partial z} - \frac{\partial}{\partial t}\left(\frac{\partial \mathcal{L}}{\partial \dot{z}}\right) + \frac{\partial^2}{\partial x^2}\left(\frac{\partial \mathcal{L}}{\partial z''}\right) - \frac{\partial}{\partial x}\left(\frac{\partial \mathcal{L}}{\partial z'}\right) = 0. \tag{4.24}$$

Therefore, the Euler-Bernoulli equation for the static and dynamic displacement of a double clamped beam beam reads

$$\rho A \ddot{z}^2 = K - EIz'''' + Tz'', \tag{4.25}$$

where z'''' is the fourth derivative with respect to x and $\ddot{z}$ is the second derivative with respect to t. We divide the displacement into a static and a dynamic component:

$$Z(x,t) = z_{\text{s}} \times \phi_{\text{s}}(x) + z_1(t) \times \phi_1(x), \tag{4.26}$$

here z_{s} is the maximum static displacement, $z_1(t)$ is the maximum dynamic displacement, and $\phi_s(x)$ and $\phi_1(x)$ are the normalized static

and dynamic profiles of the displacement. We consider the case of a single mechanical mode with the shape:

$$\phi_s(x) = \phi_1(x) = \sin(\pi x/L), \tag{4.27}$$

this is a valid approximation when the beam is under tensile tension. We insert Eq. 4.26 and Eq. 4.27 into Eq. 4.25, we multiply Eq. 4.25 by $\phi_1(x)$, and we finally integrate it from 0 to L to get

$$\begin{aligned}\frac{d^2z_1}{dt^2} = &-\frac{1}{\rho A}\left[EIz_s\left(\frac{\pi}{L}\right)^4 + T_0 z_s\left(\frac{\pi}{L}\right)^2 + \frac{EA}{4}z_s^3\left(\frac{\pi}{L}\right)^4 - \frac{4}{\pi}K\right] \\ &-\frac{1}{\rho A}\left[EI\left(\frac{\pi}{L}\right)^4 + T_0\left(\frac{\pi}{L}\right)^2 + \frac{3}{4}EAz_s^2\left(\frac{\pi}{L}\right)^4\right] z_1(t) \\ &-\left[\frac{3E}{4\rho}z_s\left(\frac{\pi}{L}\right)^4\right] z_1^2(t) - \left[\frac{E}{4\rho}\left(\frac{\pi}{L}\right)^4\right] z_1^3(t).\end{aligned} \tag{4.28}$$

The first bracket, which represents the sum of the static terms, is independent of $z_1(t)$ and it has to be equal to zero in a static equilibrium position.

$$EIz_s\left(\frac{\pi}{L}\right)^4 + T_0 z_s\left(\frac{\pi}{L}\right)^2 + \frac{EA}{4}z_s^3\left(\frac{\pi}{L}\right)^4 - \frac{4}{\pi}K = 0. \tag{4.29}$$

We note that z_s can be expressed as function of the external force and the elastic characteristics of the beam. Finally, the equation of motion for a double clamped beam is

$$\frac{d^2z_1}{dt^2} = \alpha_1 z_1(t) - \alpha_2 z_1(t)^2 - \alpha_3 z_1(t)^3. \tag{4.30}$$

If we compare Eq. 4.30 with Eq. 4.17, the spring constant k is proportional to α_1. In the studied case there is no coefficient proportional to $\dot{z}$ and we didn't include any dissipation in the quantification of U_{total}.

4.4 Backaction in NEMS

In this section we introduce the concept of backaction in a nanomechanical resonator through the linear response theory [85, 86, 91, 92]. The backaction can modify the eigenmode dynamics, including its effective temperature, the dissipation, and the resonance frequency.

The backaction is usually associated with the effect of the detector on the object of study. In the classical case of a single electron transistor coupled to a nanomechanical resonator, we understand the

detector as the quantum conductor used to measure the position. The case of a carbon nanotube electro-mechanical resonator goes as follows. The detector and resonator constitute the same entity. The position is electrically detected using the electron current flowing through the mechanical oscillator. As a result of this measurement, the electron fluctuations perturb its position which reacts back in the electron transport in a closed cycle with a certain delay time τ_{delay}. We can apply the linear response theory in order to understand how the backaction of the quantum conductor affects the oscillator. We study the case when the conductor and the resonator are weakly coupled and the current responds linearly to the motion of the system. In order to study the backaction in a CNT-based NEMS, we are interested in studying how the position z is coupled with the quantum conductor. The Hamiltonian that represents the linear coupling between the position and its detection expresses as

$$H_{\text{int}} = -A\hat{z} \cdot \hat{F}, \tag{4.31}$$

where A is the coupling constant which has to be small enough to allow the linear description of the system. The operators $\hat{z}$ and $\hat{F}$ represent the position and quantity in the conductor that couples to the motion of the oscillator, respectively.

The detection of the position creates a backaction force on the oscillator. The fluctuating backaction force is related to the operator $\hat{F}$. Therefore, the unsymmetrized quantum force noise writes as

$$S_{\text{FF}}(\omega) = \int_{-\infty}^{\infty} \langle \left[\hat{F}(t), \hat{F}(0)\right] \rangle e^{i\omega t} dt, \tag{4.32}$$

where $\langle \left[\hat{F}(t), \hat{F}(0)\right] \rangle$ is the expected value of the commutator $\left[\hat{F}(t), \hat{F}(0)\right]$. Note that now S_{FF} refers to the quantum PSD as opposed to the classical one presented in Eq. 3.13 [2].

We now recover the equation of motion Eq. 4.3 in presence of an external incoherent driving force (thermal force) and the backaction force introduced above. This backaction force is expressed as a fluctuating force $\delta f(t)$ and an average force $f_{\text{avg}}(t)$.

$$m_{\text{eff}} \frac{d^2 z}{dt^2} + kz(t) + m_{\text{eff}} \Gamma_0 \frac{dz}{dt} = \delta f_0(t) + \delta f(t) + f_{\text{avg}}(t). \tag{4.33}$$

As we saw above, $m_{\text{eff}} \Gamma_0 \frac{dz}{dt}$ and $\delta f_0(t)$ describe the effects of the thermal bath on the oscillator, Γ_0 and $\delta f_0(t)$ corresponding to the damping rate and the fluctuating force, respectively. The fluctuating

[2] Note that in this section we talk about to the double-sided PSD and we refer to it as S_{FF} for convenience

force of the thermal bath is directly related with the bath temperature T as

$$S_{FF}^{th}(\omega) = m_{eff}\Gamma_0\hbar\omega \coth\frac{\hbar\omega}{2k_BT}. \tag{4.34}$$

We recover the usual result shown in Eq. 4.12 in the classical approximation $\hbar\omega \ll k_BT$ and taking the single-sided PSD.

The other terms in Eq. 4.33 describe the backaction effect on the resonator. We can understand part of this effect as having an additional thermal bath. The term δf represents the fluctuating part of the backaction force. Its power spectral density is directly determined by the symmetrized noise $S_{FF}(\omega) = 1/2\overline{S}_{FF}(\omega) + \overline{S}_{FF}(-\omega)$. In contrast to $\delta f(t)$, $f_{avg}(t)$ is the average value of the backaction force. We generalize $f_{avg}(t)$ as the sum of a conservative force (in-phase with the motion) and a damping force (out-of-phase with the motion), $f_{avg}(t) = f_{cons}(t) + f_{damp}(t)$. We develop the two components as

$$f_{damp}(t) = -m_{eff}\int_{-\infty}^{\infty}\Gamma(t-\tau)\dot{z}(\tau)d\tau, \tag{4.35}$$

$$f_{cons}(t) = \int_{-\infty}^{\infty}\alpha(t-\tau)z(\tau)d\tau. \tag{4.36}$$

If we now use the standard quantum linear response relations we obtain

$$\chi_{FF}(t) = -\frac{i}{\hbar}\theta(t)\langle[\hat{F}(t),\hat{F}(0)]\rangle, \tag{4.37}$$

$$m_{eff}\Gamma(\omega) = A^2\left(\frac{-Im[\chi_{FF}(\omega)]}{\omega}\right) = \frac{A^2}{\hbar}\left(\frac{\overline{S}_{FF}(\omega)-\overline{S}_{FF}(-\omega)}{2\omega}\right), \tag{4.38}$$

$$\Delta k(\omega) = \alpha(\omega) = -A^2\left(-Re[\chi_{FF}(\omega)]\right), \tag{4.39}$$

where $\theta(t)$ represents the unit step function, $\theta(t) = 0$ or 1 when $t < 0$ or $t > 0$ respectively.

We can understand the backaction as follow: Eq. 4.38 quantifies

how the damping generated by the backaction is related to the susceptibility χ_{FF} and the asymmetric force noise associated with the backaction.

We can define the effective temperature T_{eff} associated with the thermal bath as

$$S_{FF}(\omega) = m_{eff}\Gamma(\omega)\hbar\omega \coth \frac{\hbar\omega}{2k_B T_{eff}}. \tag{4.40}$$

When the oscillator possesses a high quality factor it is likely that the effect of the backaction is constant over the mechanical frequency bandwidth, so that we can set $\Gamma(\omega) = \Gamma(\omega_0)$.

Finally, Eq. 4.33 tells us that the mechanical oscillator has a total damping rate $\Gamma(\omega_0) + \Gamma_0$ and a temperature T_{vib} that characterizes its thermal state

$$T_{vib} = \frac{\Gamma_0 T + \Gamma(\omega_0) T_{eff}}{\Gamma_0 + \Gamma(\omega_0)}. \tag{4.41}$$

Here the damping $\Gamma(\omega_0)$ can take positive or negative values depending on the detector state.

Chapter 8 describes measurements pointing to backaction in a CNT electro-mechanical resonator.

Chapter 5

Carbon nanotube fabrication and engineering

Parts of this chapter have been published in:
Mass Sensing for the Advanced Fabrication of Nanomechanical Resonators
G. Gruber, C. Urgell, A. Tavernarakis, A. Stavrinadis, S. Tepsic, C. Magen, S. Sangiao, J. M. de Teresa, P. Verlot, and A. Bachtold
Nano Lett., 19, 69876992, (2019)

This chapter divides in two parts. We first describe the fabrication process of the devices used to perform the experiments shown in Chap. 7 and Chap. 8. Finally, we present an advanced fabrication process of carbon nanotube mechanical sensors that allows to monitor the mass while engineering the device.

5.1 Device fabrication

The fabrication process of the carbon nanotube electro-mechanical resonators used in this work is based on a chemical vapour deposition (CVD) growth done in the last step of the fabrication process. It ensures the purity of the nanotube since it is kept away from all kind of chemical substances used during fabrication.

5.1.1 Prepatterned chips

The prepatterned chips are fabricated on highly resistive silicon (Si) wafers covered with a thermally grown silicon dioxide (SiO_2) layer of 600 nm and a silicon nitride (Si_3N_4) layer of 100 nm. The purpose is to isolate the wafer from the device so no RF signal from the device

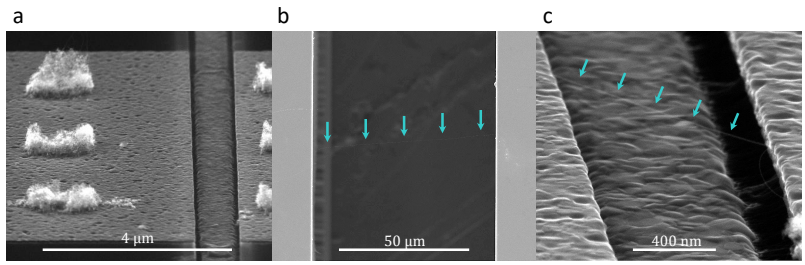

FIGURE 5.1: **Scanning electron microscopy (SEM) images of different devices.** **(a)** Image of a standard device where different catalyst islands can be clearly seen on top of the source electrode . **(b)** Ultralong CNT grown using the fast-heating method over a wide trench.Its total length surpassess 100μm. **(c)** CNT suspended over a gate electrode and grown on a prepatterned device. The green arrows in **b** and **c** are used to highlight the CNT position.

could leak to the wafer. An array of gate electrodes is defined by UV-photolithography followed by a reactive ion ecthing (RIE) process. A final wet etching process is used to etch an undercut in the SiO_2 layer to avoid any future short between the metallic electrodes. Afterwards the gate electrode is made by metal deposition of 5 nm of tungsten (W) and 75 nm of platinum (Pt). The source and drain electrodes are also patterned using a UV-photolithography process but without any additional etching. The thickness of the source and drain metallic layer is again 5 nm of W and 75 nm of Pt. The separation between source and drain varies between 1μm and 1.5μm and the nominal separation between the gate electrode and the top of the source and drain electrodes is 350 nm.

5.1.2 CVD growth process of carbon nanotubes

Here we describe the different CVD processes we carry out to fabricate ultraclean and ultralong devices. In order to grow carbon nanotubes on a prepatterned chip, we first spin the chips with a PMMA layer. Then, we pattern openings in the PMMA layer at a distance of few micrometers from the trench trough an electron-beam lithography process. Afterwards, we deposit a catalyst solution on top of the chip. The catalyst dries during 2 minutes in ambient conditions and then, the chips are baked on a hotplate at 150 ^{o}C for 5 minutes. The catalyst consists in a solution of methanol (CH_3OH) containing iron (Fe) catalyst nanoparticles mixed with molybdenum (Mo) which is used to enhance the catalytic behaviour of the Fe. The nanoparticles are trapped

in a alumina (Al_2O_3) nanoporous structure to prevent any aggregation. A lift-off process is needed to remove all the catalyst except the patterned islands, an example can be seen in Fig. 5.1(a) where the catalyst island can be clearly distinguished. An oxygen plasma process is used to remove all the organic residues on the surface. Finally, The chips are moved inside a quartz tube placed in the oven to perform the CVD growth. The CVD process is based on the decomposition of methane (CH_4) in an argon (Ar) and hydrogen (H_2) atmosphere. This process is carried out at 830 ^{o}C for around 10 minutes to prevent that the metal electrodes melt and short the circuit.

Ultraclean but short carbon nanotubes are obtained by performing the growth process in a rich Ar atmosphere (500ml$_n$/min) while flushing H_2 (100ml$_n$/min) and CH_4 (550ml$_n$/min). An example can be seen in Fig. 5.1(c) where a nanotube is suspended over a trench with 1μm width. The devices shown in Chap. 7 and Chap. 8 were grown using this method. The nanotubes presented later in this chapter were grown by using a different method. When the length of the tubes has to be longer than $5-10\mu$m the "fast-heating" method[93] is used. This method consists in rapidly sliding the substrate inside the oven to create a gradient of temperature between the substrate and the outer part of the quartz tube. This gradient of temperature creates a convection flow which lifts the catalyst nanoparticles promoting a "kite-mechanism" for the nanotube growth [94]. This growth mechanism allows to produce long carbon nanotubes. In order to create even longer tubes the Ar flow can be reduced (100ml$_n$/min) while the H_2 is increased (200ml$_n$/min) keeping the same amount of CH_4 (550ml$_n$/min). Ultralong nanotubes exceeding 100μm are grown using this method. An example is shown in Fig 5.1(b).

5.2 Advanced fabrication of carbon nanotube nanomechanical sensors

We report on a nanomechanical engineering method to monitor matter growth in real time via e-beam electromechanical coupling. This method relies on the exceptional mass sensing capabilities of nanomechanical resonators. Focused electron beam induced deposition (FEBID) is employed to selectively grow platinum particles at the free end of singly clamped nanotube cantilevers. The electron beam has two functions: it allows both to grow material on the nanotube and to track in real time the deposited mass by probing the noise-driven mechanical resonance of the nanotube. On the one hand, this detection method is highly effective as it can resolve mass deposition with a resolution in the zeptogram range; on the other hand, this method is simple to use and readily available to a wide range of potential users, since it can be operated in existing commercial FEBID systems without making any modification. The presented method allows to engineer

hybrid nanomechanical resonators with precisely tailored functionality. It also appears as a new tool for studying growth dynamics of ultra-thin nanostructures, opening new opportunities for investigating so far out-of-reach physics of FEBID and related methods.

5.2.1 Introduction

Nanomechanical devices are exquisite sensors of mass deposition [27, 95–97] and external forces[28, 29, 98–100]. These sensing capabilities enabled advances in mass spectrometry[101–103], surface science[15, 104–109], scanning probe microscopy[110, 111], and magnetic resonance imaging[20, 21, 112]. The highest sensitivity is achieved with carbon nanotube resonators[27, 29] because of their tiny mass compared to the other operational mechanical resonators. However, a general challenge with such small transducers is to provide them with a physical function, which can be e.g. magnetic, chemical, or optical. Conventional nanofabrication processes, such as electron-beam lithography and reactive-ion etching, are difficult to employ with such small suspended structures without altering their sensing capabilities. Developing new methods to engineer nanoscale resonators with high precision and providing them with a specific functionality is in high demand as it would enable a whole range of new technological and scientific applications.

5.2.2 Carbon nanotube nanomechanical sensors

In this section we report a nanofabrication method enabling ultra-sensitive, versatile functionalization of carbon nanotube resonators[113, 114] inside a scanning electron microscope (SEM). Using focused electron beam induced deposition (FEBID)[115–119], we report the mass-controlled growth of Pt particles on carbon nanotube nanomechanical sensors, enabling their optomechanical funcionalization[120]. The deposited mass is tracked in real time by monitoring frequency changes of the noise-driven oscillations of the nanotube resonator. Measuring the nanomechanical vibrations relies on e-beam electromechanical coupling[121, 122] and is accomplished using the same electron-beam as that used for FEBID. We demonstrate the high sensitivity and versatility of this method, which enables us to address mass changes over more than six orders of magnitude, with a resolution down to the zg range.

5.2.3 Sample and setup characteristics

The samples consist of carbon nanotubes grown via chemical vapor deposition on silicon substrates. The nanotubes stick to the surface

due to Van der Waals forces. Some nanotubes extend over the substrate edge, forming cantilevers. We used cantilevers with lengths between 1μm and 15μm and spring constants between 10^{-7} N/m and $2.6 \cdot 10^{-4}$ N/m in order to investigate the robustness of our method.

All SEM and FEBID experiments were conducted in a Zeiss Auriga field emission electron microscope equipped with a gas injection system (GIS). The acceleration voltage of the electron beam was 5kV and the typical beam current was 200pA. The precursor gas was methylcyclopentadienyl(trimethyl)platinum(IV) in order to grow a Pt deposit onto the sample surface when illuminated by the electron beam[123]. All the experiments reported below have been completed with the GIS nozzle being placed $\approx 500\mu$m above the substrate.

A schematic of the experimental setup used for the deposition experiments is depicted in Fig. 5.2(a). The electron beam is set onto the apex of the nanotube in spot mode while monitoring the secondary electron (SE) current I_{SE}. The signal is displayed in the frequency domain via fast Fourier transform (FFT). The data is real-time processed using a fast peak-search custom computer program, enabling us to extract the mechanical resonance frequency at a rate between typically 0.5Hz and 5Hz.

5.2.4 Mass sensing for advanced fabrication

Fig. 5.2(b) shows a nanotube before and after the deposition process with the deposited particle clearly visible. Furthermore, the free end of the nanotube appears blurred due to the motion fluctuations. The spring constant k can be extracted from the variance of the displacement δz^2 using the equipartition theorem

$$k = \frac{k_B T}{\delta z^2}, \tag{5.1}$$

where k_B is the Boltzmann constant and T is the temperature[121]. Fig. 5.2(c) shows the SE current profiles taken along the dashed lines marked in Fig. 5.2(b) before and after the deposition with Gaussian fits to determine δz^2. The resulting spring constant $k = 2.1\,(2) \cdot 10^{-6}\,\mathrm{N/m}$ is the same in both cases. This shows that k is not affected by the deposition process and any permanent changes in the mechanical resonance frequency are consequently associated with mass deposition (see further discussion below). Specific care was dedicated to avoid broadening of the observed peak by back-action phenomena during imaging[121]. This was achieved by averaging multiple frames using the fastest scanning speed (122ms/frame).

The mass of the Pt particle is monitored in real time during its formation. This is done by continuously acquiring the resonance spectrum of the noise-driven vibrations of the nanotube with the electron-beam. We typically use high resolution bandwidth settings in order

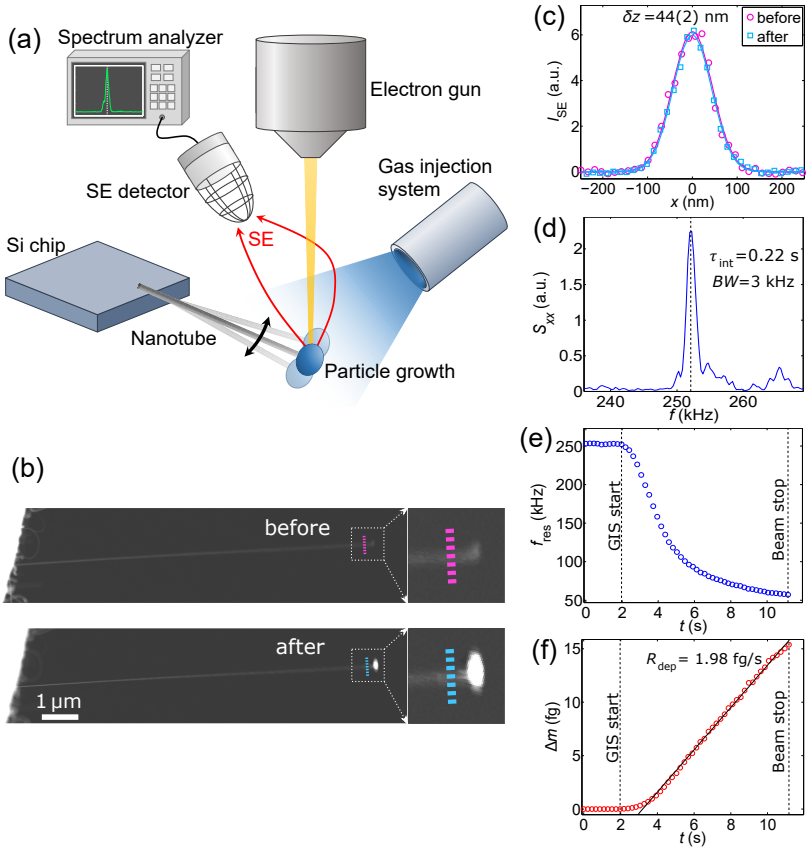

FIGURE 5.2: **(a)** Schematic of the setup: The electron beam is set on the apex of the suspended nanotube cantilever, creating a secondary electron (SE) current, which is detected and fed into a spectrum analyzer. Using the gas injection system (GIS) a nanoparticle is grown on the nanotube, resulting in a shift of the observed resonance frequency. **(b)** SEM images of a nanotube before and after the deposition of a particle, with 3x magnified view of the apex (right side). **(c)** Profiles of the SE current I_{SE} along the dashed lines marked in **b** with Gaussian fits (solid lines). **(d)** Typical resonance signal used to measure the resonance frequency. **(e)** Monitoring of the resonance frequency during the deposition; at t≈ 2s the GIS valve was opened and at t≈ 11s it was closed and the beam exposure stopped. **(f)** Deposited mass determined from **e** using Eq. 5.3.

to enable a high sampling rate. Fig. 5.2(d) shows a typically obtained

signal used to count the frequency for the mass detection. The resolution bandwidth of the measurement in this case was $BW = 3\,\mathrm{kHz}$. The resonance frequency f_{res} relates to the effective mass m^* of the mechanical eigenmode via the equation:

$$f_{\mathrm{res}} = \frac{1}{2\pi}\sqrt{\frac{k}{m^*}}. \tag{5.2}$$

Fig. 5.2(e) shows the evolution of f_{res} over time. Here, the GIS nozzle was opened at $t \approx 2\,\mathrm{s}$. The electromechanical interaction then becomes strongly non-linear, resulting in a strong amplification of the electromechanical spectrum and the appearance of a large number of peaks at multiples of the fundamental resonance frequency. We attribute this behaviour to the increasing interaction volume resulting from the deposition process. Our frequency counting algorithm includes a dynamical discrimination procedure enabling to unambiguously keep track of the fundamental resonance frequency in real-time. As shown on Fig.5.2 (e), f_{res} decreases over time, which is the expected evolution in presence of mass adsorption.

The deposition was limited to the apex of the nanotube, such that the spring strength can be reasonably assumed to remain unchanged. Therefore, the deposited mass $\Delta m\,(t)$ yields to a frequency shift, independent from the shape of the eigenmode[101]:

$$\Delta m\,(t) = \frac{k}{4\pi^2}\left(\frac{1}{f_{\mathrm{res},t}^2} - \frac{1}{f_{\mathrm{res},0}^2}\right), \tag{5.3}$$

where $f_{\mathrm{res},t}$ and $f_{\mathrm{res},0}$ are the resonance frequencies measured during the deposition at time t and prior to the deposition, respectively[27, 95–97, 101–105, 107, 109]. In the limit of high signal-to-noise ratio, the mass determination does weakly depend on the SE emission rate. Additionally, we performed optomechanical measurements[120] in order to gain independent confirmation of the post-deposition mechanical properties. These measurements ensure that the electromechanical coupling has negligible impact on the mechanical resonance frequency and that the observed changes are due to mass deposition.

Fig. 5.2(f) displays the corresponding evolution of the deposited mass over time. After some transient regime, the deposition becomes linear in time, allowing us to extract the deposition rate $R_{\mathrm{dep}} = 1.98\,\mathrm{fg/s}$ from a linear fit. At $t \approx 11\,\mathrm{s}$ the GIS valve was closed and the beam exposure was stopped to avoid spurious growth. The resonance frequency at the end was $f_{\mathrm{res}} = 56.1\,(5)$ kHz and the total mass of the particle seen in Fig. 5.2(b) is (15.5 ± 2.0) fg. Optomechanical measurements of this resonator yield to a post-deposition mechanical resonance frequency $f_0 = 57.04\,\mathrm{kHz}$ with a quality factor $Q \approx 3000$ at room temperature. Besides further confirming the mass-induced

origin of the measured frequency change, this measurement demonstrates that the deposition using FEBID does not degrade the mechanical properties of the nanotube resonator, which is crucial in the context of functionalizing nanomechanical resonators.

5.2.5 Fabrication statistics

Using the above-described methodology, a large set of hybrid nanotube cantilevers were fabricated and characterized. Fig. 5.3(a) shows the determined deposition rates and final masses of the deposited particles for each experiment. The dashed lines indicate how the deposition rate and deposited mass are related via the deposition time. The observed variations arise from different modes of operations (see further discussion below), to which have been assigned distinct colors. Note that even within the same mode of operation, the obtained results are widely dispersed. This is because FEBID is a highly complex process where various interdependent parameters may affect the growth rate[124]. These include the focus of the electron beam, the temperature of the substrate, the temperature and flux of the precursor molecules, and the pressure of residual gas in the chamber. The deposition rate is also affected by the amplitude of the nanotube vibrations, since the amplitude can be larger than the electron-beam diameter, resulting in a net decrease of the effective deposition cross-section. The different GIS operation modes as well as illustrative results are discussed in the following.

We start with the default operation mode of the GIS, which was also used for the measurements in Fig. 5.2. When the nozzle is opened the precursor gas is released into the chamber resulting in a strong increase of the chamber pressure. The pressure typically saturates in the range $p = (7-11)\times 10^{-6}$ mbar, while the background vacuum pressure is typically $\approx 1\times 10^{-6}$ mbar. It results in measured deposition rates between 0.28 fg/s and 11 fg/s. Fig.5.3 (b) shows a typical measurement in this operation mode, demonstrating a constant deposition rate $R_{\mathrm{dep}} = 0.34$ fg/s over a time as long as 50 s. The deposited mass is more than 30 times larger than the initially measured mass of the nanotube cantilever.

We explored lower Pt deposition rates by reducing the pressure. This is achieved by first purging the GIS nozzle with precursor molecules and then pumping the chamber for several minutes. As such, we investigated deposition of precursor molecules in a pressure range $p = (1-1.7)\times 10^{-6}$ mbar resulting in observed deposition rates ranging between 0.93 ag/s and 8.5 ag/s. A typical mass deposition measurement in this low-pressure regime is displayed in Fig. 5.3(c). The SEM image after the deposition reveals a small Pt particle. The deposition rate $R_{\mathrm{dep}} = 0.93$ ag/s is equivalent to roughly 2900 Pt atoms or 1800 precursor molecules per second.

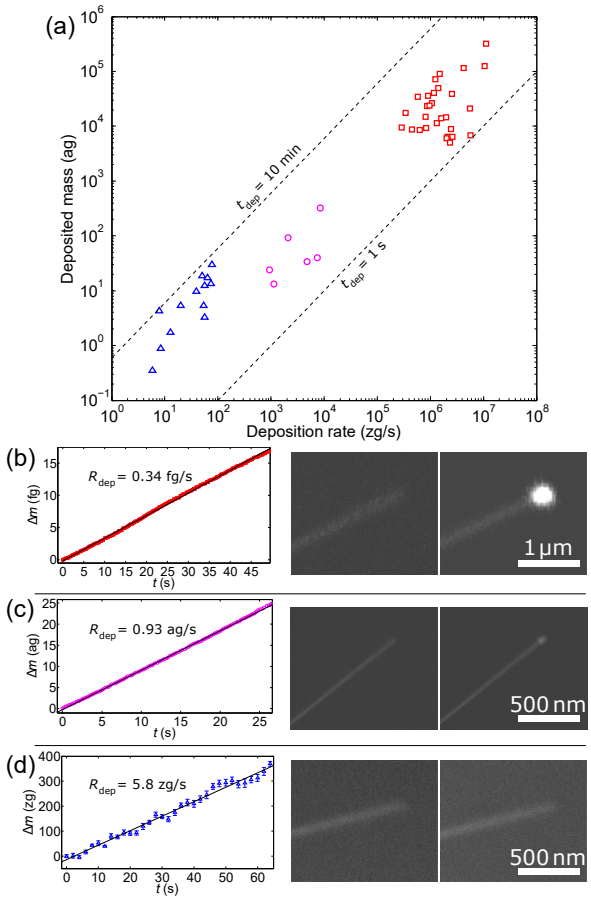

FIGURE 5.3: **(a)** Deposition rate and deposited mass for all the fabricated devices, with deposition times t_{dep} in the range between 1 s and 10 min. The different operation modes are marked by different colors, and exemplary measurements are shown in **b**-**d**. **(b)** Mass deposition in default GIS operation mode (GIS nozzle open, precursor in the chamber at a pressure in the range of $p = (7 - 11) \times 10^{-6}$ mbar). **(c)** Mass deposition in low-pressure mode (GIS nozzle closed, precursor residuals in the chamber with $p = (1 - 1.7) \times 10^{-6}$ mbar). **(d)** Mass deposition in the background vacuum regime (after more than 24 h of pumping, $p = (0.8 - 1) \times 10^{-6}$ mbar). The SEM images on the right show each nanotube before and after the deposition. The spring constants determined before and after the deposition are $k = 6.2\,(5) \times 10^{-7}$ N/m for **b**, $k = 1.57\,(7) \times 10^{-5}$ N/m for **c**, and $k = 1.00\,(3) \times 10^{-6}$ N/m for **d**.

The lowest deposition rates were attained by pumping the chamber for more than 24 h with the GIS nozzle closed and heated so residual precursor molecules could desorb from the nozzle and be pumped away. It is assumed that in this regime the chamber gas is predominantly composed of organic molecules resulting in e-beam deposition of amorphous carbon. The base pressure in this background vacuum regime was in the range $p = (0.8 - 1) \times 10^{-6}$ mbar and the observed deposition rates were between 5.8 zg/s and 77 zg/s. The lowest value $R_{\mathrm{dep}} = 5.8\,\mathrm{zg/s}$ with 2s integration time was observed in the experiment shown in Fig. 5.3(d) and is equivalent to about 290 C atoms per second. Computing the Allan deviation of the resonance frequency with 2s integration time results in an effective mass resolution of 13zg. This estimation includes the spurious contribution of the deposition of C atoms, so that it represents an upper bound of the mass resolution of the nanotube resonator. The deposited mass of 330 zg does not result in a distinctive feature on the nanotube in the SEM images. In this case, the electromechanical measurement enables us to reveal the evolution of the structure that is totally invisible in the SEM image. Besides controlling the growth process, this demonstrates the relevance of e-beam electromechanical coupling as a powerful complementary embedded tool to scanning electron microscopy.

5.2.6 Conclusions

In summary, we have reported a method allowing high-resolution mass monitoring of the growth of a Pt nanoparticle on a nanotube resonator via *in situ* electromechanical readout in a FEBID system. The method can be readily employed in any existing SEM or STEM setup without requiring any further modification. The demonstrated mass and time resolution offers a precise control on the deposited mass to engineer nanomechanical sensors, especially since various materials can be grown with FEBID [125, 126]. This may lead to new advances in one- and two-dimensional [110, 111] magnetic force microscopy [127] and magnetic resonance force microscopy [20, 112, 128]. Our technique may also be employed with semiconducting nanowire resonators made from e.g. GaN, SiC, and InAs [122, 129–131] as well as microfabricated top-down resonators [100, 132–138].

Chapter 6

Measurement setup

We present in this chapter the cryostat and its wiring where carbon nanotube electro-mechanical resonators are measured. Different improvements in the setup regarding filtering, thermalization and better thermometry are presented. Note that the last improvements were implemented after the experiments presented in Chap. 7 and Chap. 8.

6.1 Experimental setup description

The low temperature experiments are carried out in two dilution refrigerators, the models Triton 200 and Triton 400 from Oxford Instruments with a base temperature of 15 mK. The measurement setup is designed to perform noise measurements and transmission measurements from few Hz's to hundreds of MHz's. The system is made up of radiofrequency (RF) lines, DC lines and a RF read-out scheme. The RF lines consist of UT85-SS-SS stainless steel radio-frequency cables from the room temperature stage to the 700 mK still stage. From the still plate to the mixing chamber (MC) the lines are formed of UT85-Nb-Nb niobium cables to avoid any thermal exchange between different stages. All the radiofrequency lines are attenuated using cryogenic attenuators as shown in the setup schematic (Fig. 6.1). The attenuation consists of 10dB at $T = 45$ K, 20 dB at $T = 3.5$ K, 6 dB at $T = 700$ mK. There are an additional 20 dB on the source line at the MC. The RF line employed for the gate electrode has additional 10 dB at the MC from a directional coupler ZX30-9-4-S+ from Mini-circuits, which physically isolates the gate line. Regarding the DC lines, a thermocoax Cu/Nb cable (around 100Ω) is used from room temperature to the MC. A UT85-Nb-Nb radio-frequency cable is also used for the read-out line from the MC to the still plate, from the still stage to room temperature UT85-SS-SS or UT85-Cu-Cu radio-frequency cable is used (depending on which dilution fridge model).

The RF lines are filtered as follow. A VLFX-225+ filter from Mini-circuits is used in the gate line. DC-blocks are placed outside the fridge in order to prevent the injection of low frequency noise from the RF

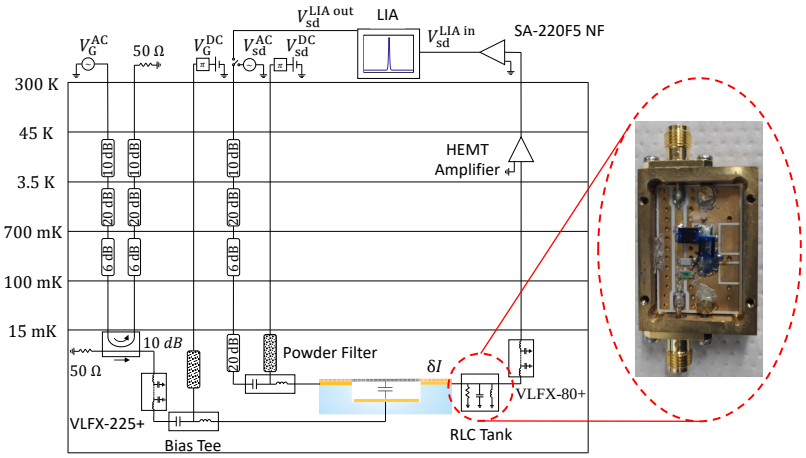

FIGURE 6.1: **Schematic of the setup.** Both the DC and the RF lines of the setup are represented together with the cryogenic wiring. All the amplification chain is represented. The inset shows an image of the homemade RLC circuit. We can distinguish all the RLC components along with the epoxy to better thermalize the circuit.

sources through the RF lines. The DC lines are filtered at room temperature using π-filters. The high frequency noise is filtered at base temperature by using powder filters. The low frequency noise in the DC line is also filtered using bias tees ZFBT-6GW+ from Mini-circuits. The bias tee also mixes the RF with the DC signal. A VLFX-80+ filter from Mini-circuits is placed in the read-out line together with an RLC circuit made of a ultra-high precision 10KΩ SMD resistor, two high frequency 33μF inductors, and the intrinsic capacitance of the circuit together with an additional 10pF SMD multilayer ceramic capacitor mounted on the PCB (see the Fig. 6.1 inset). The signal is amplified at low temperature by a high electron mobility transistor (HEMT) amplifier [139, 140] and at room temperature by a SA-220F5 NF low noise amplifier as in [15, 29]. Finally, the sample is located in a cooper sample box covered by a metallic shield to isolate it from the RF environmental noise.

The DC voltages are applied to the sample and to the HEMT amplifier using SIM928 SRS isolated voltage sources and high stability isolated voltage DC sources BE2142 BiLT from Itest. The RF signals are generated with a Rohde & Schwarz SMB 100A microwave signal generator and a zurich lock-in amplifier UHFLI 600 MHz. We measure the output signal using again the UHFLI 600 MHz lock-in input port.

6.2 Cryogenics

Advancing towards the temperature reduction is mandatory in order to study quantum phenomena. As mentioned in the previous section, our dilution refrigerators achieve a base temperature of 15 mK but the temperature of the electrons inside our quantum circuit differs from this value. Therefore, the electron temperature T_{el} and the cryostat temperature T decouple. RF heating, bad thermalization and electrical noise transmitted through the circuit lines are the dominant heating effects. Aiming to keep the heat leak as small as possible, every line is filtered and thermally anchored to the cryostat as explained in the previous section.

6.2.1 Thermalization

Here, we present the strategies to thermalize the system. First of all, we fabricate every thermalization element using materials with a high thermal conductivity.

The thermalization of every the RF line is done through the attenuators that thermally anchor the inner conductor to every stage. The DC line coaxial cables are pressed between two gold-plated oxygen-free copper clamps thermally anchored at every stage to achieve a good thermalization. As previously demonstrated [141, 142], the thermalization of the device is mainly done through the electrical contacts. Therefore, the RLC printed circuit board (PCB) is screwed to its oxigen free copper box to improve the thermal anchoring. The thermal link between the sample contacts and the PCB is done by aluminium wirebonds.

In order to better thermalize the RLC resonator a silver-filled epoxy (EPO-TEK H20E) was added on the PCB after the experiments shown in Chap. 7 and Chap. 8. The current RLC resonator can be observed in the inset of Fig. 6.1. The improvement of thermalization is formidable, the details will be discussed in the next section.

6.2.2 Effective electron temperature

We need to find a reliable way to determine the effective temperature T_{el} of our samples since the MC temperature of our dilution refrigerator is not reliable to determine it. Two methods based on current fluctuation measurements are presented to quantify the electronic temperature of either the overall circuit on the MC plate or the quantum electron device. These fluctuations are a very robust thermometer.

Johnson-Nyquist noise of the RLC circuit

The Johnson-Nyquist noise accounts for the electrical noise in the circuit. This is the intrinsic electronic noise generated by the thermal

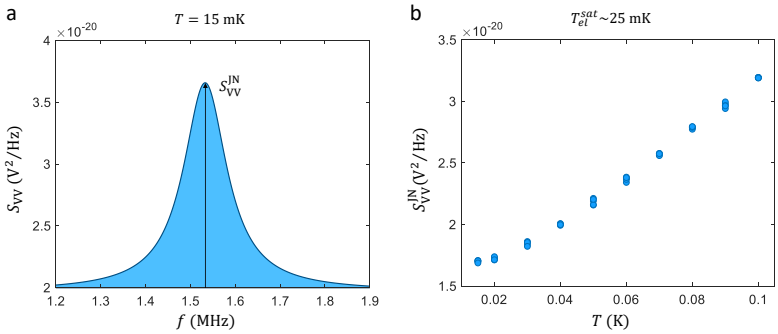

FIGURE 6.2: **RLC Johnson-Nyquist noise. (a)** Voltage power spectral density S_{VV} at a given cryostat temperature of 15mK. The height of the peak S_{VV}^{JN} corresponds to Eq. 3.14. The measured curve is smoothed. **(b)** We plot the height S_{VV}^{JN} at different temperatures T. The saturation point can be clearly observed between 20mK and 30mK.

agitation of the charge carriers inside an electrical conductor in equilibrium, which happens regardless of any applied voltage. The power spectral density (PSD) is described by Eq. 3.14. Which we previously described as a white noise in Chap. 3.

Taking advantage of the Johnson-Nyquist we can estimate the temperature of the electrons at the MC level. In the experiments presented in Chap. 7 and Chap. 8 we couldn't cool the RLC below 70 mK due to bad thermalization [29]. The improvements described in the previous section lead to an important reduction of the T_{el}.

The current noise of the RLC resistor is converted into voltage by the RLC filter. It is amplified by both the HEMT amplifier and the room temperature amplifier. By using a Fourier transformation, we record the PSD of the voltage noise S_{VV} at an specific T, an example is depicted in Fig. 6.2(a). Finally, we measure S_{VV} at different temperatures to extract the saturation point, see Fig. 6.2(b).

A clear saturation of the Johnson-Nyquist noise is observed between 20 mK and 30 mK. The current and voltage noise of the HEMT remain constant during the MC temperature sweep since the amplifier is kept at a constant temperature on the 3.5 K plate. The only noise contribution that depends on the temperature comes from the RLC resonator current fluctuations. In conclusion, we can state that the electronic noise going from the RLC resonator to the nanotube device thermalize at about 25 mK.

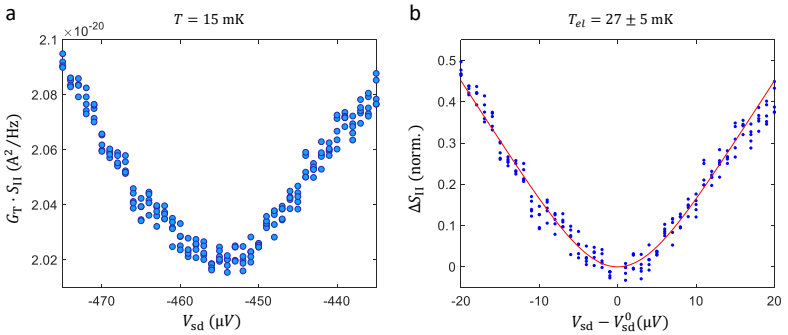

FIGURE 6.3: **Carbon nanotube shot noise. (a)** Current power spectral density multiplied by the effective gain $G_T \cdot S_{II}$ as function of the applied DC bias V_{sd} at a cryostat temperature of 15mK. **(b)** Normalized excess of current noise ΔS_{II} as function of the source-drain voltage V_{sd}. We extract an electronic temperature $T_{el} = 27$mK from this specific curve.

Shot Noise of a carbon nanotube nanoresonator

The excess of PSD $\Delta S_{II}(V_{sd})$ for a short quantum conductor is expressed as

$$\Delta S_{II}(V_{sd}) = S_{II}(V_{sd}) - S_{II}(0). \tag{6.1}$$

It can be approximated in the standard scattering approach to a two terminal conductor in the zero-temperature approximation [143–145]:

$$\frac{S_{II}(V_{sd})}{G_T} = \frac{2e^2}{h} \sum_{n=1}^{4} \tau_n (1 - \tau_n) \cdot \left[eV_{sd} \coth \frac{eV_{sd}}{2k_B T_{el}} - 2k_B T_{el} \right], \tag{6.2}$$

where G_T is the effective gain of the amplification chain, e the elemental charge, h the planck constant, V_{sd} the source-drain bias applied to the carbon nanotube and τ_n corresponds to the transmission probability per conduction channel. In the case of a carbon nanotube quantum conductor, we consider 4 conduction channels due to the spin and valley degeneracy.

We perform the shot noise measurements of carbon nanotube resonators at the base temperature of the dilution refrigerator. The current noise fluctuations of the shot noise are converted into voltage through the total impedance of the system. The system consist of the resistance of the RLC resistor and the impedance of the carbon nanotube. As in the previous case, the S_{VV} is amplified and recorded. The shot noise measurements are carried out at different V_{sd} values

around the effective zero source-drain bias as shown in Fig. 6.3. Using the Eq. 6.2, we are able to extract T_{el} with only two fitting parameters, T_{el} itself and $\tau_n(1-\tau_n)$. We systematically extract an electron temperature around 27 ± 5 mK as a result of the fitting of multiple traces. These results proved to be independent of the applied gate voltage V_{g} showing the robustness of this method. We can conclude that the strategies used to enhance the measurement setup lead to more than a factor 2 improvement of T_{el} with respect to the results shown in Chap. 7 and Chap. 8 which correspond to the setup configuration presented in ref. [29].

Chapter 7

Fabry-Pérot Oscillations in Correlated CNTs

Parts of this chapter have been published in::
Fabry-Pérot Oscillations in Correlated Carbon Nanotubes
W. Yang, C. Urgell, S. L. De Bonis, M. Margańska, M. Grifoni and A. Bachtold
Phys. Rev. Lett., 125, 187701, (2020)

We report the observation of an intriguing behavior in the transport properties of nanodevices operating in a regime between the Fabry-Pérot and the Kondo limits. Using ultrahigh quality nanotube devices, we study how the conductance oscillates when sweeping the gate voltage. Surprisingly, we observe a fourfold enhancement of the oscillation period upon decreasing temperature, signaling a crossover from single-electron tunneling to Fabry-Pérot interference. These results suggest that the Fabry-Pérot interference occurs in a regime where electrons are correlated. The link between the measured correlated Fabry-Pérot oscillations and the SU(4) Kondo effect is discussed.

7.1 Introduction

Electron interactions and quantum interference are central in mesoscopic devices. The former are due to the electronic charge and give rise to many-body effects; the latter emerges due to the wave-like properties of an electron. Resonant ballistic devices with a few conduction modes and moderate coupling to electrodes are sensitive to both of these electronic properties. On the one hand, quantum interference between electron waves backscattered at the boundaries between the mesoscopic system and the metallic electrodes gives rise to resonant features in the transmission, analogous to the light transmission in an optical Fabry-Pérot cavity [70]. On the other hand, if

the electron spends enough time in the mesoscopic device before being transmitted, Coulomb repulsion can also become important giving rise to Coulomb blockade and single-charge tunneling effects [65]. Despite considerable efforts, the interplay between electron interactions and quantum interference remains poorly understood from both an experimental and a theoretical point of view, due to the many-body character of the problem. This is the topic of the present chapter.

7.2 Interaction or interference

Carbon nanotubes (CNTs), semiconducting nanowires, and edge channels of the quantum Hall effect are ideal quasi one-dimensional (1D) systems to study both electron correlations and quantum interference. In fact, various many-body effects including Coulomb blockade [33, 36, 146], Wigner phases [147–150], Luttinger liquid [151, 152] and Kondo physics [37, 40, 153–162] as well as Fabry-Pérot and Mach-Zehnder oscillations resulting from electron interference [41, 42, 73, 163–166] have been observed in these multi-mode 1D systems.

It is possible to switch from interaction- to interference-governed transport regimes by tuning the tunnel couplings at the interface between the wire and the electrodes, Γ_S and Γ_D for the source (S) and drain (D) electrodes. Which transport regime dominates crucially depends on how large the tunneling broadening $\hbar\Gamma = \hbar(\Gamma_S + \Gamma_D)$ is compared to other energy scales, in particular to the charging energy E_C, being the electrostatic cost to add another (charged) electron to the wire [32]. In the so-called quantum dot limit, characterized by $\hbar\Gamma \ll E_C$, tunneling events in and out of the wire are rare and Coulomb charging effects are dominant. They give rise to Coulomb blockade phenomena and incoherent single-electron tunneling in the regime $\hbar\Gamma < k_BT \ll E_C$. By decreasing temperature, one expects coherent single electron tunneling for $k_BT \simeq \hbar\Gamma \ll E_C$, where the width of the Coulomb peaks is determined by Γ; at even lower temperatures, when spin-fluctuations become relevant, the Kondo effect emerges as the dominant transport mechanism. In the opposite limit of large transmission, $\hbar\Gamma \gg E_C$, interference effects give rise to the characteristic Fabry-Péerot patterns, which can be easily calculated from a non-interacting single-particle scattering approach [41]. In the focus of this chapter is the intermediate transmission regime $\hbar\Gamma \sim E_C \gg k_BT$ when no clear hierarchy of energy scales exists.

An experimental hallmark of both interaction- and interference-dominated transport is the modulation of the conductance when sweeping the electrochemical potential, that is, by varying the gate voltage V_g. In the incoherent tunneling regime, the alternance of single-electron tunneling and Coulomb blockade physics results in finite conductance peaks with a period in V_g of the order of e/C_g [65],

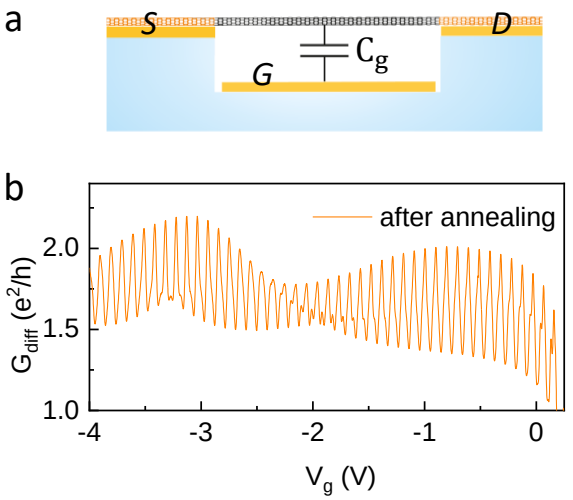

FIGURE 7.1: **Schematics of the device and low-temperature transport characteristics. (a)** Three-terminal device with a suspended CNT contacted to source (S), drain (D), and gate (G) electrodes. **(b)** Gate voltage dependence of the conductance at zero source-drain voltage of device I at $T = 15$mK measured after the current annealing step. An oscillating voltage with amplitude smaller than $k_B T/e$ is applied to measure the differential conductance.

where $-e$ is the (negative) electron charge and C_g is the capacitance between the nanotube and the gate electrode; see Fig. 7.1(a). In contrast, in the interference-dominated regime, the conductance modulation of the Fabry-Pérot oscillations arises from the electron wave phase accumulated during a round trip along the nanotube. The presence of valley and spin degrees of freedom gives rise in CNT interferometers to oscillations of period $\Delta V_g = 4e/C_g$ [41].

In this chapter, we improve the quality of nanotube devices to an unprecedented level. We discover a crossover of the conductance oscillation period between e/C_g and $4e/C_g$ upon sweeping temperature. Above helium temperature, the period is e/C_g with oscillations amplitudes pointing to coherent single-electron tunneling in an open quantum dot configuration. At low temperature, the period becomes $4e/C_g$ and the oscillations feature typical characteristics of Fabry-Pérot interference. These unexpected data are a clear signature of the interplay between interaction and quantum interference.

7.3 Electron transport measurements

We grow nanotubes by chemical vapor deposition on prepatterned electrodes [167]. The nanotube is suspended between two metal electrodes, see Fig. 7.1. We clean the nanotube in the dilution fridge at base temperature by applying a high constant source-drain voltage V_{sd} for a few minutes (see Sec. A.1.1 of the App. A). This current-annealing step cleans the nanotube surface from contamination molecules adsorbed when the device is in contact with air.The energy gap of the two nanotubes discussed in this chapter is on the order of 10 meV (for details see the App. A). The length of the two suspended nanotubes inferred by scanning electron microscopy (SEM) is about 1.5μm.

Figure 7.1(b) shows the modulation of the differential conductance G_{diff} of device I as a function of V_g in the hole-side regime at 15 mK. Rapid conductance oscillations are superimposed on slow modulations. Since the conductance remains always large, that is above e^2/h, we attribute the rapid oscillation to the Fabry-Pérot interference with period in gate voltage being $\Delta V_g = 4e/C_g$. The slow modulation may be caused by the Sagnac interference [42, 73], the additional backscattering due to a few residual adatoms on the CNT, the symmetry breaking of the electronic wave function by the planar contacts of the device, or any combination of these.

A crossover to a regime dominated by the charging effects in an open interacting quantum dot is observed upon increasing temperature. Specifically, by sweeping the temperature from 15 mK to 8 K the amplitude of the oscillations gets smaller. Further, the oscillation period gets four times lower, changing from $4e/C_g$ at 15 mK to e/C_g at 8 K, see Figs. 7.2(a) and 7.2(c)-7.2(e). The period in V_g is calibrated in units of e/C_g using the measurements in the electron-side regime, where regular Coulomb oscillations are observed at 8K, as shown in Fig. 7.2(b). The same behavior is observed in device II, Figs. 7.3(a) and 7.3(b). The $4e/C_g$ oscillations vanish above 4K in both devices, whereas the e/C_g oscillation amplitude is suppressed to almost zero below $\sim$ 1K in device I and below $\sim$ 0.1K in device II, see Figs. 7.2(f) and 7.3(b).

7.4 Energy hierarchy

Our interpretation of a temperature-induced crossover between two seemingly distinct transport regimes is confirmed by measured maps of the differential conductance as a function of source-drain and gate voltages at $T = 15$mK and $T = 8$K, as shown in Fig. 7.4(a) and 7.4(d), respectively. The low-temperature data feature the regular

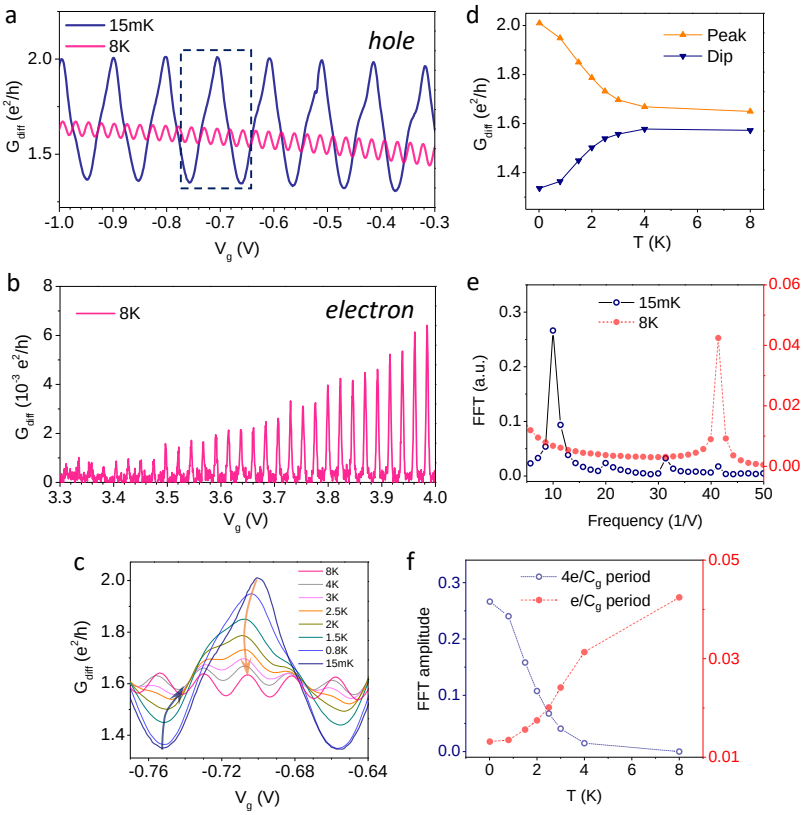

FIGURE 7.2: **Temperature-induced crossover from an interference-dominated to a charging-controlled regime in device I. (a), (b)** Oscillations of the conductance $G_{\mathrm{diff}}(V_{\mathrm{g}})$ versus gate voltage V_{g} in the hole- and electron-doped regimes. **(c)** Evolution of the oscillation period for a series of different temperatures. The range of V_{g} shown in this figure is highlighted in panel a by a dashed rectangle. **(d)** Temperature dependence of the conductance associated with a peak and a dip, as indicated by arrows in **c**. **(e)** Fast Fourier transform (FFT) of the $G_{\mathrm{diff}}(V_{\mathrm{g}})$ traces at 15 mK and 8 K measured for V_{g} between -1.0V and -0.3V. **(f)** Temperature dependence of the FFT amplitude associated with the $4e/C_{\mathrm{g}}$ period oscillations and the e/C_{g} period oscillations.

chess-board-like Fabry-Pérot interference pattern [41], while the high-temperature data show smeared Coulomb diamonds. Such measurements further allow us to extract important energy scales for our device. The characteristic bias V_{sd}^{*} indicated by the arrow in Fig. 7.4(a)

yields a single-particle excitation energy $\Delta E = eV_{sd}^{*} \simeq 1.7$meV. This value is consistent with what is expected from a nanotube with length $L \simeq 1.5\mu$m. Assuming the linear dispersion $\varepsilon(k) = \hbar v_F k$, with longitudinal quantization $k_n = n\pi/L$ and the Fermi velocity $v_F = 10^6$m/s, it yields $\Delta E = \varepsilon(k_{n+1}) - \varepsilon(k_n) = \hbar v_F \pi/L \simeq 1.4$meV.

The charging energy is estimated from the charge stability diagram measurements at 8K, Fig. 7.4(d); from the Coulomb diamond, indicated by the dashed lines, a charging energy $E_C \simeq 3.6$meV is extracted. Further, we estimate $\hbar\Gamma \sim E_C$ because of the strong smearing of the diamonds in Fig. 7.4(d) and the weak conductance modulation at 8K in Fig. 7.2(a). The energy hierarchy in our experiment is thus $E_C \simeq \hbar\Gamma \simeq \Delta E \gg k_B T$.

The evolution of the 15 mK conductance oscillations as a function of the source-drain bias shows that both oscillations coexist over a large bias range, albeit with modulated strengths, see Figs. 7.4(a)-7.4(c). The main trend is that the oscillation period changes from $4e/C_g$ at zero bias to e/C_g at high bias. By contrast, the evolution in perpendicular magnetic field shows that the conductance peaks are split in two, with the splitting in gate voltage being linear in magnetic field; see Figs. 7.3(c) and 7.3(d). This is attributed to the Zeeman splitting, since the associated g-factor is 2.4 ± 0.4. The error in the estimation arises from the uncertainty in the lever arm. These data indicate degeneracy of the four electron levels associated to the spin and valley degrees of freedom.

7.5 Interpretation in terms of Fabry-Pérot in a correlated system

We examine possible origins of the temperature-induced period change. Let us first assume that interactions are not important. Then, upon lowering temperature, noninteracting Fabry-Pérot oscillations are expected to emerge when the thermal smearing becomes smaller than the single-particle excitation energy. However, thermal smearing is associated to a characteristic temperature $T_{th} \sim \Delta E/k_B \sim \Gamma/k_B \approx$ 20 K, which is rather different from the measured crossover temperature $T_C \sim 3$K in Fig 7.2(f) and 7.3(c). In addition, thermal smearing cannot explain the suppression at low temperature of the e/C_g oscillations due to coherent single-electron tunneling. Therefore, thermal smearing is not at the origin of the measured period change. The single-particle Fabry-Pérot interference theory does not explain our findings. The cause of the fourfould variation of the period could not be explained considering only charge fluctuations.

The high-temperature measurement of the charging effect in an open quantum dot indicates electron correlation. When reducing temperature, the associated e/C_g conductance oscillations disappear smoothly to give rise to the $4e/C_g$ oscillations. The smoothness of

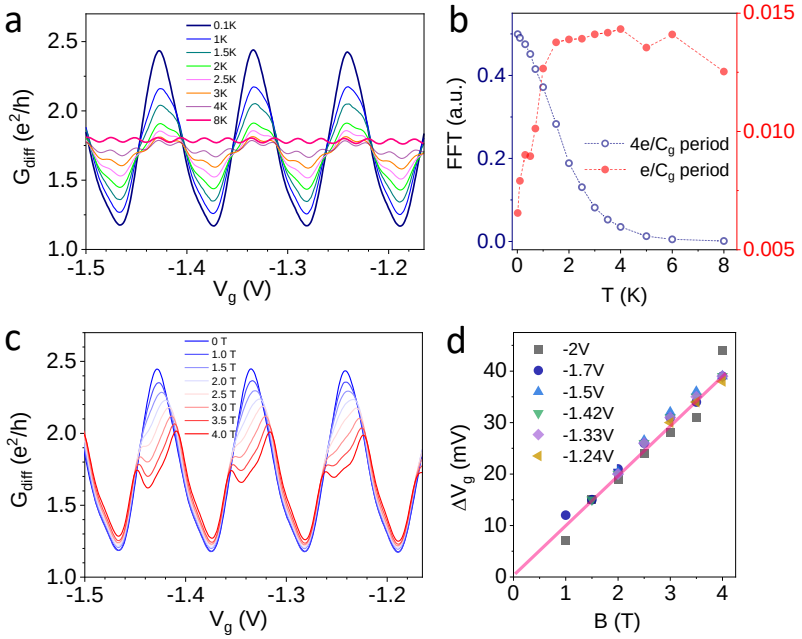

FIGURE 7.3: **Measurements on device II. (a)** Conductance traces for a series of different temperatures. **(b)** Temperature dependence of the FFT amplitude associated with the $4e/C_g$ and the e/C_g period oscillations. **(c)** Conductance traces for different perpendicular magnetic fields at 15 mK. **(d)** Peak splitting as a function of magnetic field for the conductance peaks at different gate voltages.

the crossover suggests that the Fabry-Pérot-like oscillations also occur in a regime where electrons are correlated. Such oscillations have similarities but also differences compared to the SU(4) Kondo effect in carbon nanotubes, occurring in the weak tunneling regime $E_C \gg \hbar\Gamma > k_B T$ [159, 168]. In the Kondo effect, the tunneling coupling is low enough compared to the charging energy to allow full localization of the charge within the dot, but it is large enough compared to the Kondo energy to enable both spin and valley fluctuations [40]. This results in a crossover from charging effects at high temperature to the increased conductance of Kondo resonances at zero temperature with a fourfold enhancement of the oscillation period [32, 154, 168]. In contrast to our observations, though, in the SU(4) Kondo effect, the conductance alternates between large values close to $4e^2/h$ at oscillation maxima and almost zero at the minima [159, 168]; see also Sec. A.1.2 of App. A. In our annealed devices, the tunneling coupling is large; $\hbar\Gamma \simeq E_C$. The charge is no longer strongly localized

within the dot. As a result, our devices are in a regime where there are also charge fluctuations in the nanotube in addition to spin and valley fluctuations. This might be at the origin of the crossover of the conductance oscillation period observed in this chapter, similar to what happens in the SU(4) Kondo regime [32, 154, 168], but with conductance minima clearly distinc from zero. We emphasize that the low temperature linear conductance $G_{\mathrm{diff}}(V_{\mathrm{g}})$ data alone do not allow one to distinguish between non-interacting and correlated Fabry-Pérot oscillations. However, the smooth modulation between e/C_{g} and $4e/C_{\mathrm{g}}$ oscillations upon increasing the bias (see Fig. 7.4(c)) further supports our hypothesis of correlated Fabry-Pérot regime.

7.6 Conclusions

Our work provides a comprehensible phenomenology of transport in nanotubes when both interference and interaction are involved. The findings presented in this chapter have been possible thanks to the high quality of the devices, since otherwise disorder leads to irregular $G_{\mathrm{diff}}(V_{\mathrm{g}})$ modulations that are difficult to interpret. The main results are summarized as follows: (i) We measure a fourfold enhancement of the oscillation period of $G_{\mathrm{diff}}(V_{\mathrm{g}})$ upon decreasing temperature, signaling a crossover from coherent single-electron tunneling to Fabry-Pérot interference; both oscillations coexist at the crossover temperature. (ii) Upon increasing the source-drain bias at low temperature, both oscillations coexist over a large bias range. (iii) The Sagnac-like modulation pinpoints the quantum interference nature of the Fabry-Pérot oscillations at zero bias. (iv) The magnetic field data suggest a fourfold spin and orbital degeneracy at zero-magnetic field.

The unexpected temperature-induced crossover, possibly related to charge, spin, and valley fluctuations, raises an important question: How does the strength of charge fluctuations compare to that of spin and valley fluctuations in our experiment? Indeed, when the electron transmission approaches one in open fermion channels, the electron shot noise is suppressed to zero [144], indicating that there are no longer any charge, spin, and valley fluctuations in nanotubes; by contrast, in the lower Γ limit of SU(4) Kondo, spin and valley fluctuate, but not the charge.It is then natural to ask how the crossover temperature for these more open interacting channels compare with the well-known Kondo temperature of closed quantum dots. However, a quantitative description of our experiment constitutes a theoretical challenge. It will be interesting to measure shot noise [169–172] and the backaction of the electro-mechanical coupling [10] (like in the Chap. 8) to further characterize these correlated Fabry-Pérot oscillations.

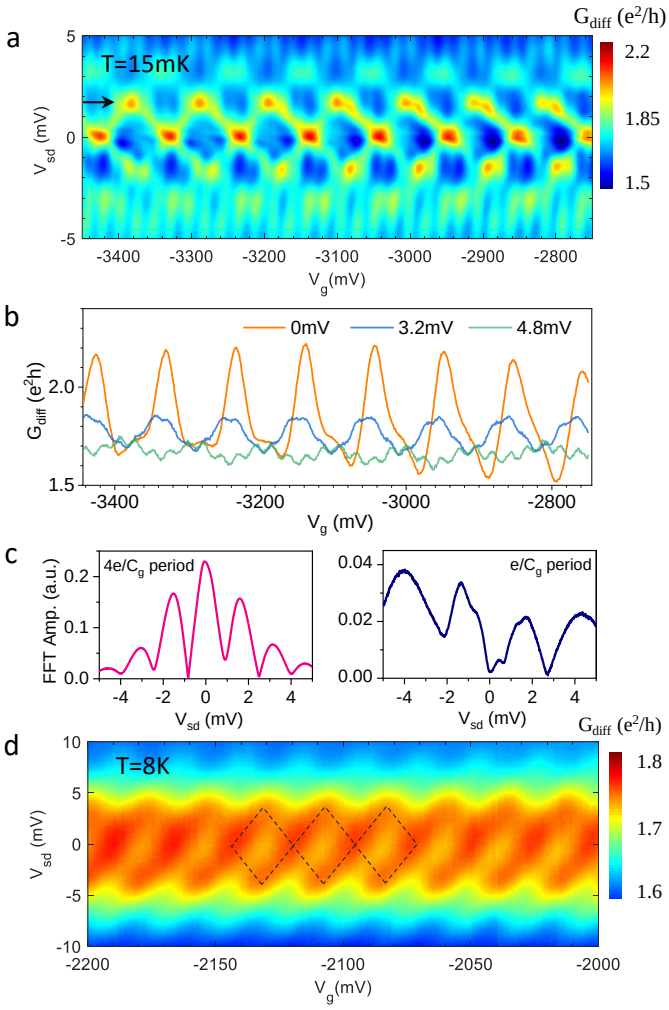

FIGURE 7.4: **From Fabry-Pérot patterns to blurred Coulomb diamonds in device I**. **(a)** Map of the differential conductance as a function of V_{sd} and V_g at 15 mK. From the position of the arrow the single-particle excitation energy is extracted. **(b)** Differential conductance traces for a series of different source-drain voltages at 15 mK. **(c)** Source-drain voltage dependence of the FFT amplitude associated with the $4e/C_g$ and the e/C_g period oscillations at 15 mK. The curves are obtained by doing a FFT of the $G_{diff}(V_g)$ trace for each V_{sd} value.**(d)** A map of the differential conductance as a function of V_{sd} and V_g at 8K. The dashed lines highlight the contours of the Coulomb diamonds.

Chapter 8

Cooling and Self-Oscillation in a Nanotube Electro-Mechanical Resonator

Parts of this chapter have been published in:
Cooling and Self-Oscillation in a Nanotube Electro-Mechanical Resonator
C. Urgell, W. Yang, S. L. De Bonis, C. Samanta, M. J. Esplandiu, Q. Dong, Y. Jin and A. Bachtold
Nature Phys., 16, 32-37, (2020)

Nanomechanical resonators are used with great success to couple mechanical motion to other degrees of freedom, such as photons, spins, and electrons [43, 173]. The motion of a mechanical eigenmode can be efficiently cooled into the quantum regime using photons [43–45], but not with other degrees of freedom. Here, we demonstrate a simple yet powerful method for cooling, amplification, and self-oscillation using electrons. This is achieved by applying a constant (DC) current of electrons through a suspended nanotube in a dilution fridge. We demonstrate cooling down to 4.6 ± 2.0 quanta of vibrations. We also observe self-oscillation, which can lead to prominent instabilities in the electron transport through the nanotube. We attribute the origin of the observed cooling and self-oscillation to an electrothermal effect. This work shows that electrons may become a useful resource for cooling the mechanical vibrations of nanoscale systems into the quantum regime.

8.1 Introduction

The vibrations of mechanical resonators have been coupled to electrons in different transport regimes, such as single-electron tunneling [5–9, 174, 175], Kondo [176], and quantum Hall effect [177, 178]. Because mechanical resonators are excellent force sensors, a small electrostatic force created by electrons generates a large displacement of the resonator. Conversely, the displacement reacts back on the electrons by a sizeable amount. This backaction of electrons on the resonator has been frequently studied by measuring the change in resonance frequency and in energy decay rate of vibrations [5–9, 174–178]. In principle, the backaction of electrons can also be used to suppress and amplify thermal vibrational fluctuations and to generate self-oscillation by applying a DC electron current [49, 91]. Reducing the thermal displacement fluctuations of a mechanical eigenmode is equivalent to cooling it according to the equipartition theorem. Signatures of a modest cooling down to $\sim$ 200 quanta as well as self-oscillation were observed over a decade ago in a pioneer work [12] where a resonator is coupled to a superconducting single-electron transistor. Meanwhile, many theoretical schemes have been proposed to cool mechanical vibrations using electrons in different electron transport regimes; see for instance Refs. [179–183]. However, these cooling schemes could not be implemented due to experimental difficulties. In this chapter, we show efficient backaction cooling in a current-biased suspended nanotube precooled in a dilution fridge.

Carbon nanotubes are a versatile system for the study of both electron transport and nanomechanics. Different electron transport regimes can be reached by tuning the transmission of electrons between the nanotube and electrodes [32]. Interaction can lead to electron attraction, Kondo behaviours, and Wigner states [32, 147, 184]. On the other hand, carbon nanotubes are so small that they make the lightest mechanical resonators fabricated thus far. Cooling a nanotube resonator in a dilution fridge leads to high quality factors [25, 26]. As a result, the force sensitivity of the resonator is record high [29], and the effect of the electron-vibration coupling is expected to be especially large.

8.2 Fabrication and measurement scheme

Suspending a carbon nanotube between two metal electrodes is key to form a nanomechanical resonator and to carry out state-of-the-art electron transport measurements. This suppresses the electron backscattering in the nanotube due to the charge impurities and the rugosity of the substrate. We grow the carbon nanotube between two metal electrodes in the last step of the fabrication process using chemical vapour

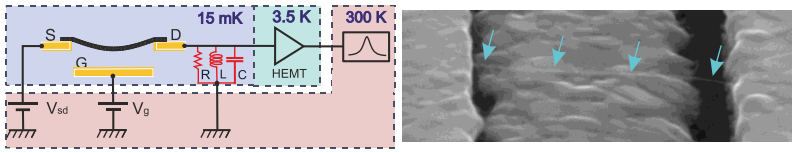

FIGURE 8.1: **Characterization of the nanotube electro-mechanical resonator.** Measurement schematic and scanning electron microscopy image of the suspended nanotube. Voltages V_{sd} and V_g are applied to electrodes S and G, respectively. Electrode D is connected to a RLC resonator and a high-electron-mobility-transistor (HEMT) amplifier.

deposition in order to minimise residual contamination [25]. Measurements are carried out by applying a DC voltage to the source electrode (V_{sd}) and the gate electrode (V_g) patterned at the bottom of the trench; see Fig. 8.1. We detect the electrical current from the drain electrode using a RLC resonator with frequency $\omega_{RLC} = 2\pi \cdot 1.27$ MHz and a high-electron-mobility-transistor amplifier [29, 113].

8.3 Characterization of the device

We record the differential conductance G_{diff} of the device by applying an oscillating voltage V_{sd}^{ac} to the source electrode with the frequency set at ω_{RLC}. Using a capacitive transduction scheme [29], we measure thermal vibrations with resonance frequency ω_0 by applying V_{sd}^{ac} at the frequency $\omega_0 - \omega_{RLC}$. In order to avoid perturbations from the measurement, we keep the amplitude of V_{sd}^{ac} much smaller than $k_B T/e$, where k_B is the Boltzmann constant, T the temperature of the cryostat, and e the electron charge. All the measurements presented here are carried out at the base temperature of the fridge except when stated differently.

Electron transport measurements indicate that electrons are in the Kondo regime [32]. A regular shell filling with Kondo ridges at zero source-drain bias is observed upon sweeping V_g; see Figs. 8.2(a) and 8.2(b). Unlike normal Coulomb blockade, G_{diff} increases in every second conductance valleys when decreasing temperature. This shows the SU(2) nature of the Kondo effect in this device.

Energy decay measurements of thermal vibrations reveal that the quality factor $Q = 6.8 \cdot 10^6$ is remarkably high when compared to previous works [25, 26, 29]. This is also higher than the quality factor inferred from the spectral resonance linewidth, since the energy decay rate Γ_{decay} is smaller than the spectral resonance linewidth Γ_{width}; see Figs. 8.3(a) and 8.3(b). The difference is attributed to dephasing.

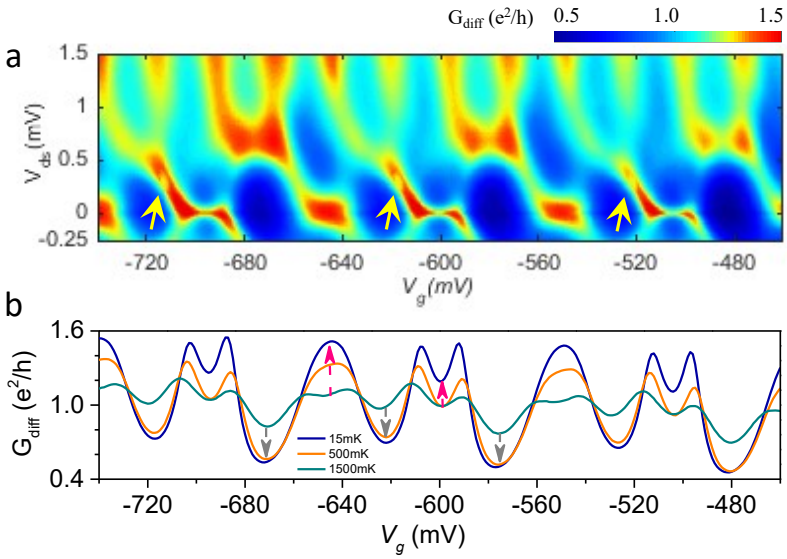

FIGURE 8.2: **Characterization of the nanotube electro-mechanical resonator. (a)** Differential conductance as a function of $V_{\rm sd}$ and $V_{\rm g}$. Yellow arrows indicate regions of conductance instabilities. **(b)** Differential conductance as a function of $V_{\rm g}$ with $V_{\rm sd} = 0$ mV.

The resonance frequency can be tuned by sweeping both $V_{\rm g}$ and $V_{\rm sd}$; as in Figs. 8.3(e) and 8.3(f). The slopes $\partial\omega_0/\partial V_{\rm g}$ and $-\partial\omega_0/\partial V_{\rm sd}$ are often rather similar, suggesting that they are related to the same origin, that is, the mechanical tension induced by the static displacement of the nanotube. Thermal vibrations can be cooled with the cryostat down to ~ 70 mK; like in Fig. 8.3(f). We attribute the saturation of the displacement variance at low temperature to the electric noise in the circuit.

8.4 Conductance instabilities

We observe instabilities in the conductance arising periodically in $V_{\rm g}$; see arrows in Fig. 8.2(b). They emerge at finite source-drain bias in charge stability diagram measurements. In these instability regions, the peaks in conductance are truncated, Figs. 8.4(a-c), and conductance traces as a function of $V_{\rm g}$ appear noisy; see Fig. 8.4(d). While similar conductance instabilities were previously reported [8], we will show below that these instabilities are related to large-amplitude vibrations.

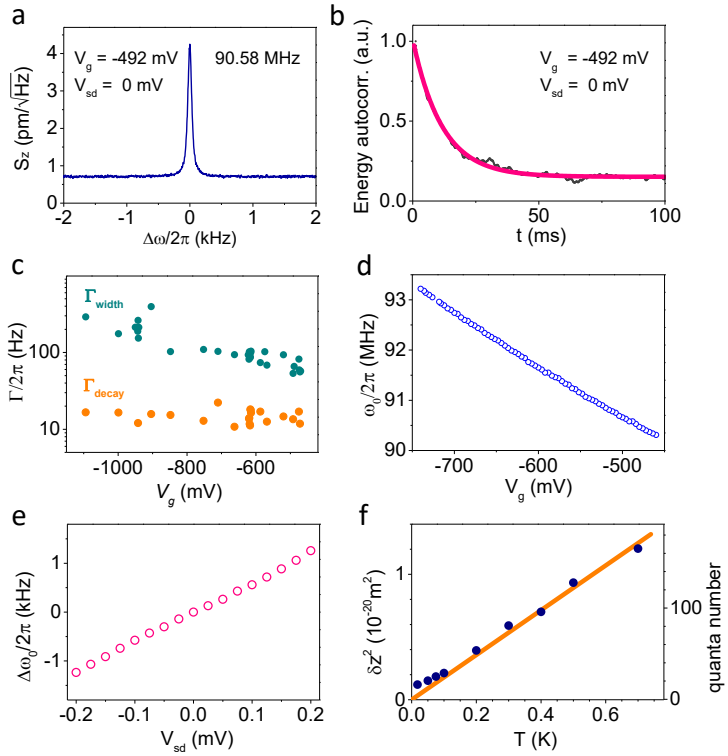

FIGURE 8.3: **Characterization of the nanotube electro-mechanical resonator.** **(a)** Displacement spectral density. **(b)** Energy decay obtained from the autocorrelation of the time (t) trace of $X^2 + Y^2$, where X and Y are the two quadratures of thermal vibrations. The pink line indicates an exponential decay. **(c)** Decay rate $\Gamma_{\rm decay}$ and spectral resonance width $\Gamma_{\rm width}$ as a function of $V_{\rm g}$ with $V_{\rm sd} = 0$ mV. **(d,e)** Resonance frequency as a function of $V_{\rm g}$ and $V_{\rm sd}$. We set $V_{\rm sd} = 0$ mV in **d** and $V_{\rm g} = -560$ mV in **e**. **(f)** Variance of the displacement of thermal vibrations as a function of temperature at $V_{\rm g} = -185$ mV.

The measured conductance instabilities originate from the switching of the mechanical motion between thermal noise and self-oscillation (Fig. 8.5). Upon sweeping $V_{\rm sd}$ through the instability region, the variance of the displacement δz^2 dramatically increases (Fig. 8.5(a)), and the decay rate gets suppressed towards zero near the border of the instability region (shaded in yellow in Fig. 8.5(b)). These two experimental facts point to the development of self-oscillation.

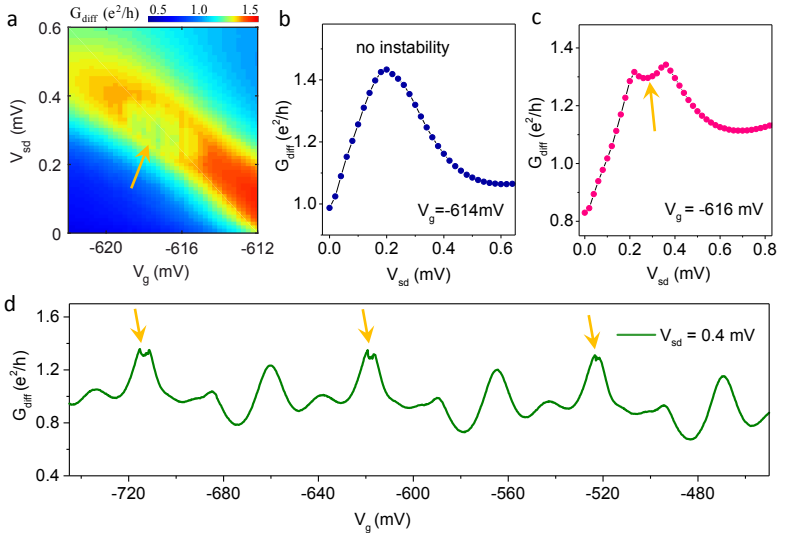

FIGURE 8.4: **Conductance instabilities. (a)** Differential conductance as a function of V_{sd} and V_g. Yellow arrows in the different panels indicate regions of conductance instabilities. **(b,c)** Differential conductance as a function of V_{sd} for two different V_g values. **(d)** Differential conductance as a function of V_g.

The phase-space and the histogram of the two quadratures of the motion can be described by the superposition of the distributions of a donut and a Gaussian-like peak (Figs. 8.5(h,i)), suggesting that the motion switches back and forth between self-oscillation with high δz^2 and thermal noise with low δz^2 (Sec. B.3 of App. B). This switching is further supported by the fact that the resonance lineshape is unusually broad, as in Fig. 8.5(g); indeed, the large linewidth is then related to the large fluctuations of δz^2 and the resonator nonlinearity. Pure self-oscillation with narrow resonance lineshape can also be observed without any switches to thermal vibrations; this often happens at higher V_{sd} values. The shift in resonance frequency due to electron backaction (Fig. 8.5(c)) is difficult to quantify, since the resonance frequency also depends on the mechanical tension induced by V_{sd}, the temperature rise of the nanotube lattice due to Joule heating, and the variance of the displacement through the mechanical nonlinearity.

8.5 Backaction cooling

Mechanical vibrations are cooled down to 4.6 ± 2.0 quanta at $V_g = -943$ mV upon increasing the source-drain bias to $V_{sd} \simeq 0.565$ mV; Figs. 8.6(a-c). Cooling is accompanied with a strong increase of the

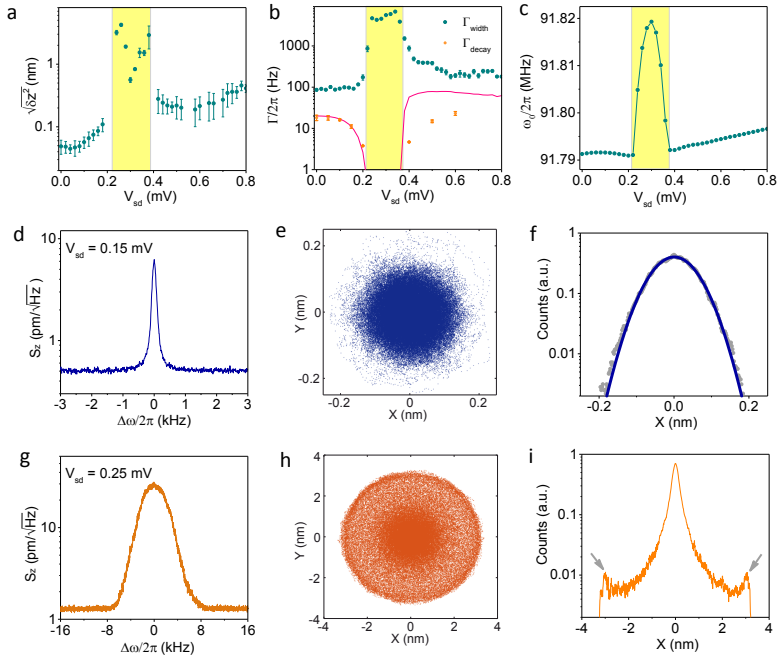

FIGURE 8.5: **Self-oscillation at $V_g = -616$ mV. (a)** Variance of the displacement as a function of V_{sd}. The yellow shaded area represents the region with self-oscillation. **(b)** Decay rate and spectral resonance width as a function of V_{sd}. The pink line is the expected decay rate using Eq. 8.1. **(c)** Resonance frequency as a function of V_{sd}. **(d-f)** Displacement spectral density, the phase-space of the two quadratures of the motion, and the associated histogram at $V_{sd} = 0.15$ mV. **(g-i)** Same as **d-f** but at $V_{sd} = 0.25$ mV. The arrows in **(i)** indicate the donut distribution. The confidence interval (CI) error bars in **a,b** arise from the uncertainty in the fitting of the measurement of the resonance lineshape and the energy decay to a Lorentzian and an exponential decay, respectively.

decay rate (Fig. 8.6(d)), indicating a backaction effect. This efficient cooling occurs when the transconductance is negative and large; see Fig. 8.1(e). We observe cooling at other V_g values when the transconductance is negative as well (Sec. B.2 of App. B). The determination of the number of quanta is robust against the hypothetical miscalibration of the amplification chain and of the attenuation along the coaxial cables (Sec. B.1 of App. B). The uncertainty in the transconductance, which enters into the transduction of the displacement, is 5.7 % of its

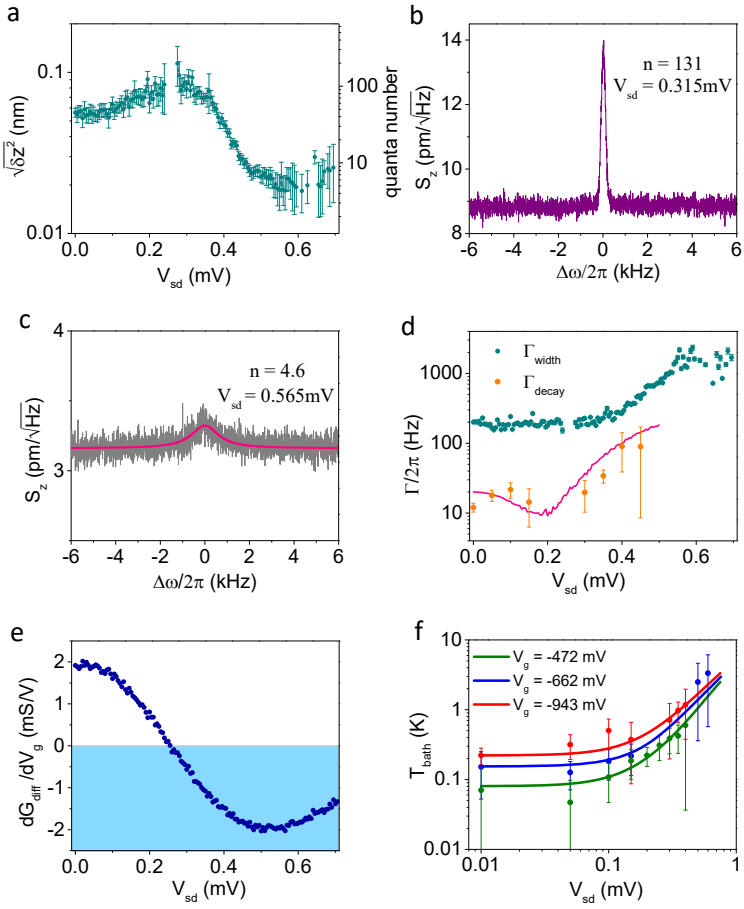

FIGURE 8.6: **Cooling at $V_g = -943$ mV. (a)** Variance of the displacement as a function of V_{sd}. **(b,c)** Displacement spectral density at two different V_{sd}. Here n is the quanta number. **(d)** Decay rate and spectral resonance width as a function of V_{sd}. The pink line is the expected decay rate using Eq. 8.1. **(e)** Transconductance as a function of V_{sd}. **(f)** Bath temperature of mechanical vibrations as a function of V_{sd} for three different V_g values. The solid lines indicate the dependence expected from Joule heating; see text. The CI error bars in **a,d** arise from the uncertainty in the fitting of the measurement of the resonance lineshape and the energy decay to a Lorentzian and an exponential decay, respectively. The error bars in **f** arise from the uncertainties in δz^2 and Γ_{decay}.

value at $V_g = -943$ mV and $V_{sd} \simeq 0.565$ mV. As explained above,

the frequency shift due to backaction cannot be quantified, since the frequency shift depends on various other effects that are difficult to disentangle experimentally.

The nanotube experiences Joule heating due to the current flowing through the resonator. Backaction cooling predicts that the phonon occupation at finite bias is given by $n(V_{sd}) = \Gamma_{bath} n_{bath}/\Gamma_{decay}(V_{sd})$ where $n_{bath} = k_B T_{bath}/\hbar\omega_0$ is the thermal phonon number and Γ_{bath} is the coupling to the thermal bath. We would achieve much lower phonon occupation, if the bath temperature T_{bath} was given by the cryostat temperature, while setting Γ_{bath} to the measured decay rate at zero-bias. This indicates that Joule heating is sizable. We deduce the bath temperature from the measured values of n and Γ_{decay} [185, 186]; see Fig. 8.6(f) . The temperature rise can be well described by Joule heating for different V_g values using the phenomenological relation $T_{bath} = T^0_{vib} + \eta G V^2_{sd}$, as in Fig. 8.6(f), where T^0_{vib} is the measured vibration temperature at zero-bias, G is the conductance, and η is the same constant for all the V_g values. The temperature rise is not accounted for by the electrostatic force associated to the electron shot noise of the nanotube, since the temperature rise does not depend linearly on V_{sd} and it is independent of V_g to a first approximation. The shot noise of the suspended nanotube behaves in the usual way with a Fano factor between 0.2 and 0.3 (Sec. B.4 of App. B).

8.6 Origin of the backaction effect

Here, we discuss the possible origins of the observed backaction. It could be related to the usual backaction in electro-mechanical resonators [5–9, 174–176], where conducting electrons generate an electrostatic force on the nanotube and the retardation of the force is given by the transmission of electrons between the nanotube and electrodes. However, we do not observe resonance frequency dips when sweeping V_g (Fig. 8.2(d)), showing that the strength of this backaction is weak. Moreover, this backaction predicts modest cooling at the conductance peaks [49, 91], which is the opposite of what is observed in Fig. 8.3, that is, self-oscillation near conductance peaks. This shows that the backaction measured in electro-mechanical resonators at zero source-drain bias cannot describe our results at finite bias. Another possible mechanism could be related to the retardation created by the circuit, where the vibration-induced current noise of the nanotube generates a retarded electrostatic force due to the capacitance of the circuit. However, the predicted decay rate is too weak to produce the cooling observed in Figs. 8.6(a) and 8.6(c). We conclude that backaction with electrostatic origins cannot account for our findings.

We attribute the origin of the backaction to an electrothermal effect [187], which is an analogue of the photothermal backaction often observed in opto-mechanical resonators [48]. The power GV^2_{sd} of Joule

heating modifies the mechanical tension in the nanotube through the effective thermal expansion coefficient of the device. This results in a net displacement δz of the resonator when the nanotube is bent by e.g. the static electrostatic force associated with V_g. This displacement reacts back on the dissipated power via $\delta G = \frac{dG}{dz}\delta z$ with a delay given by both the capacitance of the circuit and the thermalization time of the device [187]. This electrothermal effect modifies the decay rate by

$$\Delta\Gamma_{back} = -\alpha \frac{dG_{diff}}{dV_g} \frac{C_g'}{C_g} V_g z_s V_{sd}^2. \tag{8.1}$$

Here, C_g is the capacitance between the nanotube and the gate electrode, C_g' is its derivative with respect to z, and z_s is the static displacement. We use α as a free parameter in our analysis, since α depends on various quantities that are difficult to quantify. These include the thermalization time, the effective thermal expansion coefficient, and the three-dimensional profile of the static bending of the nanotube.

The electron transport in the device controls the electrothermal backaction through $\frac{dG_{diff}}{dV_g}$. When $\frac{dG_{diff}}{dV_g}$ is positive and large, the total decay rate of the resonator can become effectively negative, leading to self-oscillation. When $\frac{dG_{diff}}{dV_g}$ is strongly negative so that $\Delta\Gamma_{back} >> \Gamma_{bath}$, the vibrations are efficiently cooled. Equation 8.1 reproduces qualitatively the decay rate measured when increasing V_{sd} towards the self-oscillation regime shaded in yellow in Fig. 8.5(b) and to the strong cooling regime in Fig. 8.6(d) (see pink lines). See Sec. B.6 of App. B for more discussion on the different backactions.

8.7 Displacement sensitivity

Our detection method enables excellent displacement sensitivity. The imprecision noise S_z^{imp} can reach the level of the displacement noise of the zero-point fluctuations at resonance frequency,

$$S_z^{zpf} = \sqrt{2\hbar/m\omega_0\Gamma_{width}}, \tag{8.2}$$

where m is the effective mass (Sec. B.5 of App. B). Interestingly, the imprecision noise in this detection scheme can be further suppressed by setting the device transconductance to a higher value, while keeping the electron shot noise to a lower level compared to the Johnson-Nyquist noise by applying the source-drain voltage bias below $k_B T$. The imprecision noise reads

$$S_z^{imp} = \left(\frac{1}{2}\frac{dG_{diff}}{dV_g} V_g V_{sd}^{ac} \frac{C_g'}{C_g}\right)^{-1} S_I^{imp}. \tag{8.3}$$

Here S_I^{imp} is the current noise floor associated to the high-electron-mobility-transistor amplifier noise, the Johnson–Nyquist noise of the circuit, and the electron shot noise through the nanotube device, which can be tuned with V_{sd}^{ac} and V_{sd}.

8.8 Conclusions

Electrothermal cooling is a striking effect, since it takes advantage of Joule heating to cool mechanical vibrations. In addition, this cooling mechanism is efficient at temperatures close to the quantum regime. The electrothermal cooling method is simple, since it consists in applying a DC current of electrons through a suspended nanoelectronic device. The measurements of thermal vibrations are similar to the noise measurements on electronic devices carried out by many groups [188–190]. Electrothermal cooling allows us to demonstrate the lowest occupation number achieved with a resonator based on a low-dimensional nanoscale material [29, 48, 185, 186]. Future studies may enable ground-state cooling. This may be achieved by enhancing the back-action rate (Eq. 8.1) using devices with higher transconductance and stronger coupling to the gate (to increase the C_g'/C_g ratio). It will then be interesting to investigate the lowest measurement noise related to the imprecision noise and the quantum backaction noise, which arises from the electrostatic force noise associated to the electron shot noise. Cooling is also promising for enhancing the polaronic nature of charge carriers in a single-electron tunneling device [191]. This might offer the possibility to tune the zero-frequency electrical conduction of an electro-mechanical device.

Chapter 9

Conclusions

9.1 Summary

Throughout this thesis, we studied in detail CNT electro-mechanical resonators putting emphasis on the electron transport properties and the effects of the electromechanical coupling. Ultra-high quality devices were investigated at cryogenic temperature in an ultra-low noise environment providing a great platform to study quantum phenomena at the nanoscale.

In Chap. 5, we presented a new method to engineer CNT nanomechanical sensors. This technique allows us to monitor the mass growth of a Pt nanoparticle on the nanotube tip with high-resolution. We take advantage of a nanomechanical read-out by collecting secondary electrons in a FEBID system. This method can be easily used in any SEM or STEM setup without further modification.

In Chap. 6, we characterized the electronic temperature of the system after introducing major upgrades. We demonstrated more than a factor two reduction in the electron temperature.

In Chap. 7, we introduced ultra-clean transport measurements in suspended CNT devices. The ultra-high quality of the devices allowed us to investigate the quantum nature of the electron transport. The measurements present features of both interference and interaction between electrons. The fourfold enhancement of the conductance oscillation period while decreasing the temperature indicates the crossover from single-electron tunnelling to Fabry-Pérot interference. Both transport regimes coexist over a narrow temperature range.but over a large a long source-drain bias range. In summary, charge, spin and valley fluctuations governs the crossover between the different regimes.

In Chap. 8, we studied the coupling between the mechanical motion and the electron transport in CNT electro-mechanical systems. The backaction force has been observed trough the cooling and heating of the nanoresonator's eigenmode. The system has been cooled

to a record occupation number of 4.6 quanta. Additionally, we related the presence of the well-known transport instabilities to the self-oscillation in the CNT's motion. We attributed the backaction mechanism to an electrothermal origin. This is a simple and striking effect which takes advantage of Joule heating to efficiently cool the CNT's mechanical thermal vibrations close to the quantum regime. In conclusion, ultra-clean CNTs are an excellent platform to study the interaction between motion and electron transport because of their extremely high sensitivity to tiny forces.

9.2 Outlook

The mass and time resolution achieved in Chap. 5, together with the possibility of using different materials with FEBID [125, 126], may lead to new advances in different fields including magnetic force microscopy [20, 110–112, 127, 128]. This technique can be applied to other systems such as semiconducting nanowires [122, 129–131] and microfabricated top-down resonators [100, 132–138].

In Chap. 6, we showed how to reduce the electron temperature of suspended nanotube devices down to 25 mK. New strategies could be implemented to keep pushing down the electron temperature using better filtering and thermalization strategies [141, 142]. This is important to demonstrate the ground-state cooling of a CNT electromechanical resonator. If we enhance the backaction rate (Eq. 8.1) using devices with higher transconductance and stronger coupling to the gate (to increase the C_g'/C_g ratio), we could enhance the effect of backaction. We could also try to reduce the imprecision noise of the system towards the quantum limitation [192] and study the quantum backaction noise, which arises from the electrostatic force noise associated to the electron shot noise. The cooling effect is also promising in order to enhance the polaronic nature of charge carriers in CNT nanoresonators [191]. This might offer the possibility to tune the zero-frequency electrical conduction of an electro-mechanical device.

Another interesting line of research consists in further exploring the quantum transport through such high-quality nanotube devices. A quantitative understanding of the data presented in Chap. 7 is missing; the temperature induced crossover is not captured by any existing theoretical model. It would be interesting to compare the strength of charge, spin, and valley fluctuations when tuning temperature and the coupling rate between the nanotube and the leads. When the electron transmission approaches one in open fermion channels, the electron shot noise is suppressed to zero [144], indicating that there are no longer any charge, spin, and valley fluctuations in the nanotube; by contrast, in the lower Γ limit of SU(4) Kondo, spin and valley fluctuate, but not the charge. It is then natural to ask how the crossover temperature for these more open interacting channels compare with the

well-known Kondo temperature of closed quantum dots. We should measure the shot noise of the system [169–172] to further explore these correlated Fabry-Pérot oscillations. Since we presented a fabrication technique (see App. A) that allows us to tune the energy hierarchy of high-quality nanotube devices, we could characterize the quantum transport in a wide variety of transport regimes.

Appendix A

Additional information on Chapter 7

A.1 Experimental section

A.1.1 High-quality nanotubes obtained by current annealing

We grow nanotubes by chemical vapor deposition on prepatterned electrodes using the technique described in Ref. [167]. The nanotube is suspended between two metal electrodes Fig. A.1(a). We clean the nanotube in the dilution fridge at base temperature by applying a high constant source-drain voltage V_{sd} for a few minutes. The highest applied value of V_{sd} is usually chosen by ramping up the bias until the point when the current starts to decrease, see Fig. A.1(b). This current-annealing step cleans the nanotube surface from contamination. This procedure allows us to adsorb helium monolayers uniformly along nanotubes, indicating that the nanotube is essentially free of adsorbate contamination [15]. Figs. A.1(c,g) show the modulation of the differential conductance G_{diff} of device I as a function of V_g in the hole-side regime at 15 mK before and after annealing, respectively. The current annealing results in regular conductance modulation.

In the annealed sample rapid conductance oscillations are superposed on slow modulations, see Fig. A.1(d). Since the conductance remains always large, we attribute the rapid oscillation to the Fabry-Pérot interference with period in gate voltage being $\Delta V_g = 4e/C_g$. The first interpretation of slow modulation coming to mind is the so-called Sagnac interference, due to the gradual change of the Fermi velocity when sweeping V_g,[42, 73], caused by the trigonal warping. In the dispersion of non-interacting electrons trigonal warping manifests at energies further than $\sim$ 200 meV away from the charge neutrality point, while the range of single-particle energies scanned in our experiment is of the order of $\sim$ 56 meV (estimated from $\sim$ 40 peaks visible in Fig. 7.1(b) of Chap. 7, separated by $\Delta E \simeq 1.4$ meV). Unless the interactions bring the trigonal warping effects closer to the

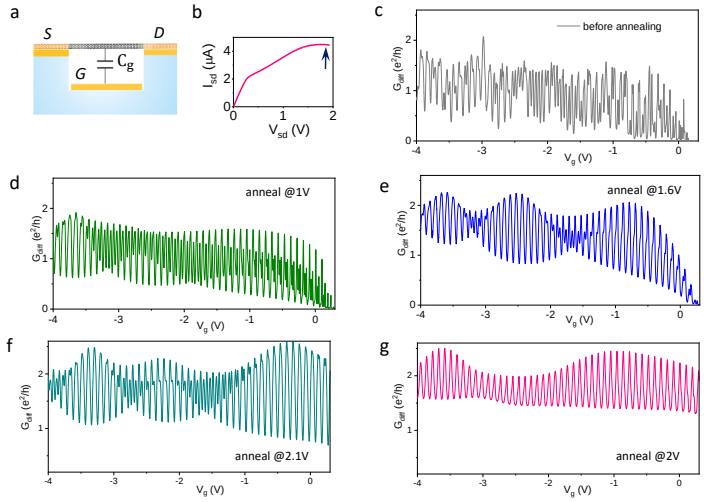

FIGURE A.1: **Current annealing and low-temperature transport characteristics. (a)** Three-terminal device with a suspended CNT contacted to source (S), drain (D), and gate (G) electrodes.**(b)** Current-voltage characteristic of device I at $T = 15$ mK. The arrow indicates when the current starts to decrease while increasing V_g. The highest voltage used for current annealing is usually around this value.**(c-g)** Gate voltage dependence of the conductance $G_{\text{diff}}(V_g)$ of device I at $T = 15$ mK measured before current annealing and after different current annealing steps. The measurements in d-g have been carried out in a second cool-down, while all the other presented data of device I have been recorded in the first cool-down. An oscillating voltage with amplitude smaller than $k_B T/e$ is applied to measure the differential conductance.

charge neutrality point, an alternative explanation of the slow modulation is needed. One possibility is the beating caused by the presence of a symmetry breaking mechanism which introduces additional valley mixing and/or another characteristic length scale into the system. The pattern of the secondary interference is completely changed each time that we do a current-annealing of the device, see Fig. A.1(d,e). We attribute this modification either to the atomic rearrangement of the platinum electrodes in the region near the nanotube, so that the intervalley backscattering rate at the contacts changes [42], or to the changed position of residual adatoms near the contacts.

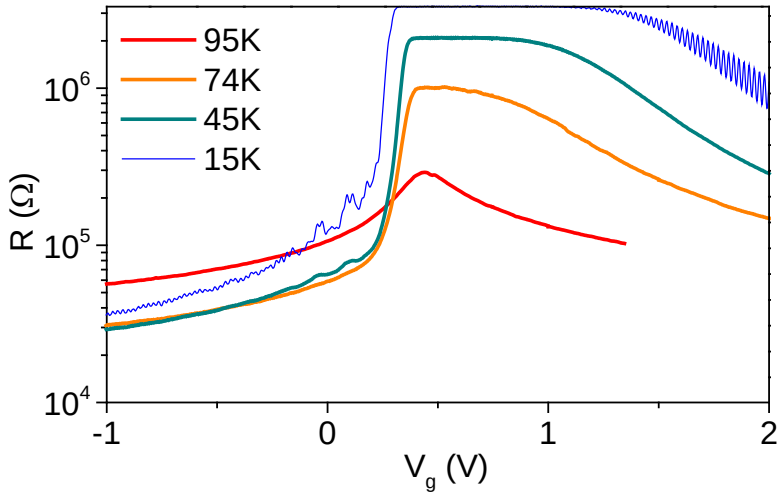

FIGURE A.2: **Resistance of device I as a function of gate voltage for different temperatures.**

The effect of the annealing on device II are discussed in the next subsection, see Fig. A.4.

A.1.2 Electron transport properties

In this subsection we provide additional data to further characterize device I and II discussed in the main text.

Size of the energy gap- The energy gap of the two nanotubes discussed in this work is on the order of 10 meV. The size of the energy gap can be obtained by recording the dependence of the resistance on V_g at different temperatures [32], see Fig. A.2. The order of magnitude of the band gap E_G is obtained from the temperature at which the resistance in the gap gets high, $E_G \sim k_B T$.

Temperature dependence of device I- In Fig. A.3 is shown a selection of $G_{diff}(V_g)$ traces of device I at different temperatures. We select the V_g ranges for which data are presented in the main text. The change in period of the oscillations with temperature is observed for all the gate voltage ranges.

Change from intermediate to strong coupling upon annealing - Finally, we show in Fig. A.4 the effect of successive annealing steps on the map of the differential conductance as a function of V_{sd} and V_g of device II. Remarkably, before annealing regions of very low differential conductance alternate with regions of high conductance in a way which

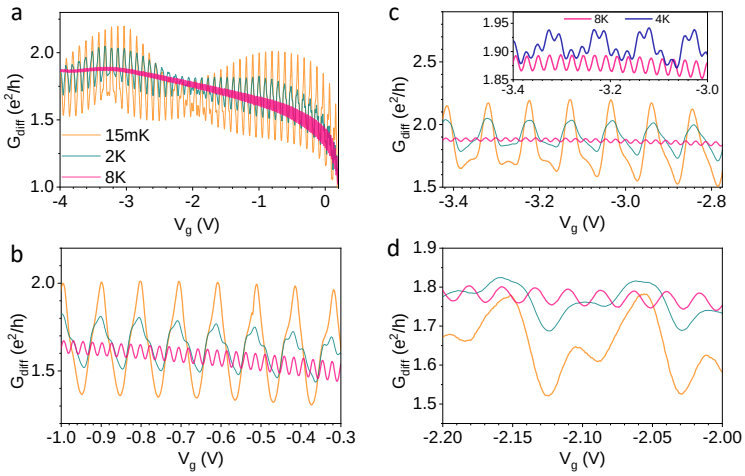

FIGURE A.3: **Series of $G_{\mathrm{diff}}(V_{\mathrm{g}})$ traces at different temperatures of device I**. We select the V_{g} ranges for which data are presented in the main text.

is reminiscent of the SU(2)xSU(2) Kondo effect seen in other CNT-based quantum dots [32]. Here, as seen from the conductance trace in Fig. A.4(d), within a periodicity of four electrons, an enhancement of the conductance is seen in the odd valleys. After the first annealing, a stronger coupling to the leads favours a conductance enhancement also in the intermediate valley, a signature of the formation of an SU(4) Kondo state. The second annealing leads to an even larger coupling to the leads, and the Kondo features are no longer seen at low bias. Rather, a checkerboard pattern typical of Fabry-Pérot interference is the dominant feature.

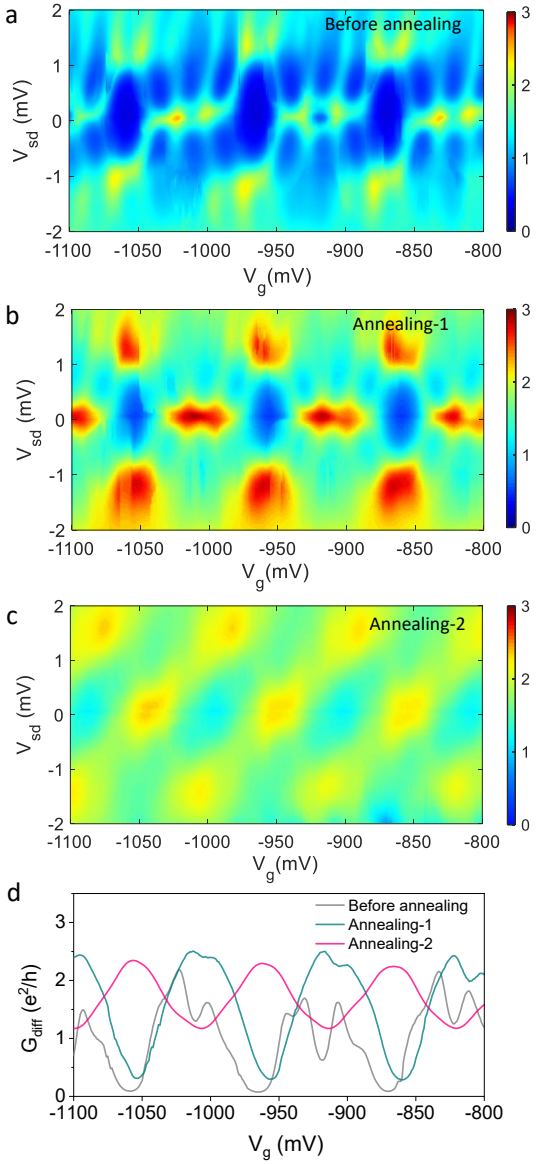

FIGURE A.4: **Differential conductance as a function of V_{sd} and V_{g} of device II after various annealing steps at $T = 15$ mK. (a)** Before annealing, the coupling to leads is such that clear Kondo ridges are observed at low bias. **(b)** Such features survive after the first annealing step. **(c)** After the second annealing step the differential conductance is overall larger and Fabry-Pérot features are seen. **(d)** Conductance traces are compared in this panel.

Appendix B

Additional information on Chapter 8

B.1 Calibration of the displacement

Electron-vibration coupling no only leads to backaction [5–9, 14, 174–178, 193–197] but also enables the detection of vibrations [22, 25, 26, 29, 113]. Mechanical vibrations are electrically detected using a RLC resonator and a HEMT amplifier cooled at liquid-helium temperature (Fig. 8.1(a) in Chap. 8 [29]). Displacement modulation is transduced capacitively into current modulation by applying an input oscillating voltage $V_{\rm sd}^{\rm ac}$ across the nanotube. The frequency $\omega_{\rm sd}/2\pi$ of the oscillating voltage is set to match $\omega_{\rm sd} = \omega_0 \pm \omega_{\rm RLC}$. Thermal vibrations are measured by recording the current noise at $\sim \omega_{\rm RLC}$. The current δI is related to the displacement of the nanotube by

$$\delta I = \beta \delta z, \tag{B.1}$$

$$\beta = \frac{1}{2}\frac{dG_{\rm diff}}{dV_{\rm g}} V_{\rm g} V_{\rm sd}^{\rm ac} \frac{C_{\rm g}'}{C_{\rm g}}. \tag{B.2}$$

The spectral density S_z of the displacement noise is obtained from the measured spectral density of the current noise using Eqs. B.1 and B.2.

The calibration of the number of quanta is obtained in a reliable way thanks to the equipartition theorem

$$m\omega_0^2 \delta z^2 = k_{\rm B} T. \tag{B.3}$$

In practice, we measure the spectral density of the current noise to quantify the variance of the current $\delta I_{\rm res}^2$ associated to the mechanical resonance of thermal vibrations. The measurement of $\delta I_{\rm res}^2$ as a function of temperature in Fig. 8.1(a) in the main text determines $m\left(\frac{C_{\rm g}}{C_{\rm g}'}\right)^2 = 2.5 \times 10^{-33} {\rm kg \cdot m^2}$ using Eqs. B.1-B.3. This allows us to quantify the effective temperature $T_{\rm vib}$ of the thermal vibrations at any

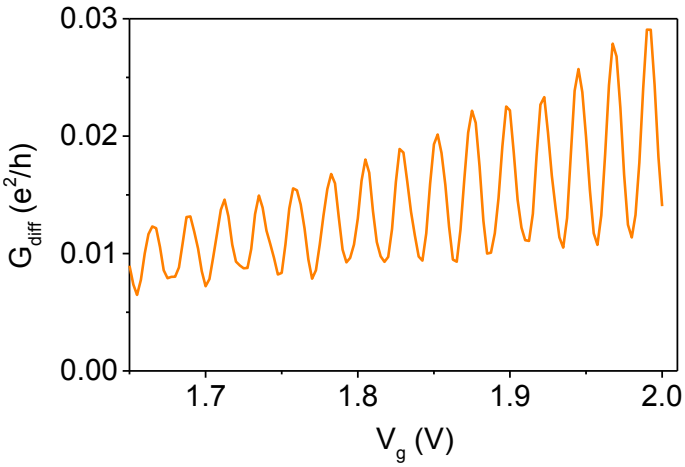

FIGURE B.1: **Coulomb blockade measurements.** Differential conductance G_{diff} as a function of gate voltage at 10 K and zero source-drain bias.

V_g and V_{sd} values by measuring δI^2_{res} and $\frac{dG_{diff}}{dV_g}$ and using

$$T_{vib} = m\left(\frac{C_g}{C'_g}\right)^2 \frac{4\omega_0^2}{k_B\left(\frac{dG_{diff}}{dV_g}V_g V_{sd}^{ac}\right)^2}\delta I^2_{res}. \tag{B.4}$$

Importantly, the determination of T_{vib} does not depend on the hypothetical inaccurate calibration of the attenuation along the coaxial cables created by thermal contraction and of the amplification chain. Indeed, such inaccurate calibration, if sizeable, would have an effect on V_{sd}^{ac} and $m\left(\frac{C_g}{C'_g}\right)^2$, but it would be canceled out when determining T_{vib}. We systematically measure $\frac{dG_{diff}}{dV_g}$ at any V_{sd}^{ac} and V_g values. The number of quanta of vibrations is obtained using $n = \frac{k_B T_{vib}}{\hbar\omega_0} - \frac{1}{2}$ with $\hbar$ the reduced Planck constant.

In order to quantify S_{zz} and δz^2, we estimate the capacitance C_g from the separation $\Delta V_g = 23.1$ mV between two conductance peaks in the Coulomb blockade regime at large positive V_g values (Fig. B.1). We obtain $C_g = e/\Delta V_g = 6.94 \times 10^{-18}$ F. We get $C'_g = 7 \times 10^{-12}$F/m from the measurement of the variance of the displacement as a function of temperature using $m = 2.7$ ag.

The energy decay rate Γ_{decay} is estimated by measuring the time trace of the two quadratures of thermal vibrations and by quantifying the autocorrelation of the amplitude squared. From these time trace measurements, we also obtain the phase-space of the two quadratures

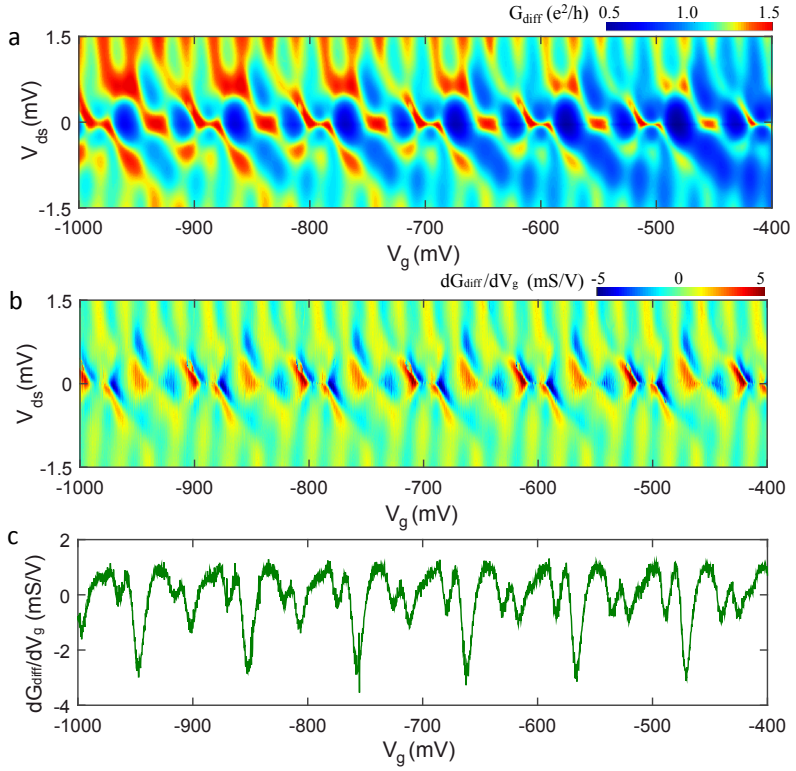

FIGURE B.2: **Electron transport measurements. (a,b)** Differential conductance and transconductance as a function of V_{sd} and V_g measured at the base temperature of the fridge. **(c)** Transconductance as a function of V_g measured at $V_{sd} = 0.7$ mV.

and the associated histogram (Fig. 8.3 of main text).

B.2 Relation between electron transport and vibration cooling

Figs. B.2(a,b) show that the measurements of G_{diff} and $\frac{dG_{diff}}{dV_g}$ as functions of V_g and V_{sd} are remarkably regular over a large range of gate voltage. This reflects the high quality of the nanotube. The shell filling with Kondo ridges at zero source-drain bias is observed over the full range of V_g. The instability in the conductance discussed in Figs. 8.1(b) and 8.2(d) of the main text appears periodically in gate voltage over the full V_g range as well.

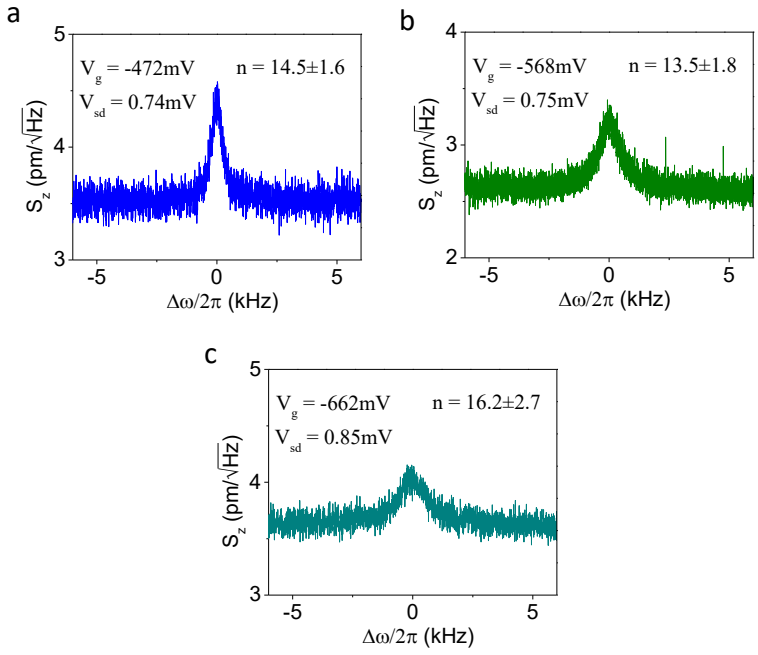

FIGURE B.3: **Cooling at different V_g values. (a-c)** Displacement power spectral density of thermal vibrations showing low occupation number in regions where $\frac{dG_{diff}}{dV_g}$ is strongly negative.

Figs. B.2(b,c) show that regions with strongly negative $\frac{dG_{diff}}{dV_g}$ emerge periodically in V_g at finite source-drain voltage. This occurs for V_{sd} in the range between 0.4 mV and 1.1 mV. We observe efficient cooling in these strongly negative $\frac{dG_{diff}}{dV_g}$ regions, as demonstrated by the measured spectra of thermal vibrations in Figs. B.3(a-c).

B.3 Self-oscillation

The vibrations of the nanotube in the instability region switch back and forth between thermal motion and self-oscillation, as it can be seen in the time traces of one of the two quadratures (X) and of the amplitude (R) in Fig. B.4. In these traces, the amplitude of thermal vibrations is low, whereas the amplitude in self-oscillation is high. These switches between thermal motion and self-oscillation occur randomly in time.

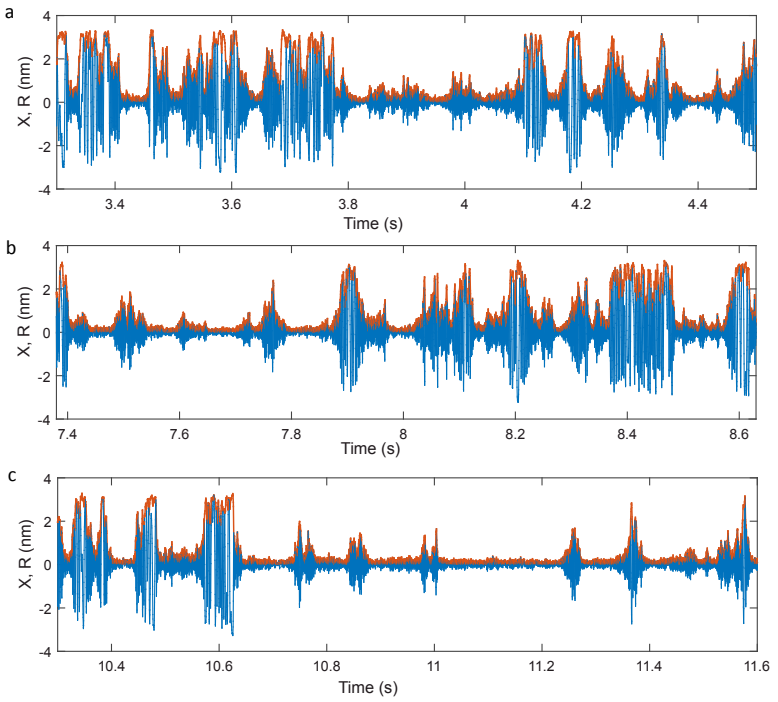

FIGURE B.4: **Time domain measurements. (a-c)** Three different time traces of one quadrature X (blue) and the corresponding amplitude R (orange) at $V_{sd} = 0.25$ mV for $V_g = -616$ mV, plotted from the Fig. 8.5(h) in Chap. 8

Pure self-oscillation can also be observed without any switches to thermal vibrations. See for instance Fig. B.5. This often happens at high V_{sd} values.

B.4 Shot Noise measurement

Here, we describe how we measure the shot noise of the nanotube device. The spectral density of the current noise S_{II} is transformed into spectral density of voltage noise S_{VV} through the total impedance $Z_{tot} = (R_{diff}^{-1} + Z_{RLC}^{-1})^{-1}$, where R_{diff} is the nanotube differential resistance and Z_{RLC} is the effective impedance of the RLC circuit. The voltage fluctuations, which are amplified by the high-electron-mobility-transistor amplifier (HEMT), are measured at the frequency $\omega_{RLC} = 2\pi \cdot 1.27$ MHz over $\sim$ 80 kHz bandwidth. Our noise measurement contains the background contribution S_{II}^{bg} related to the

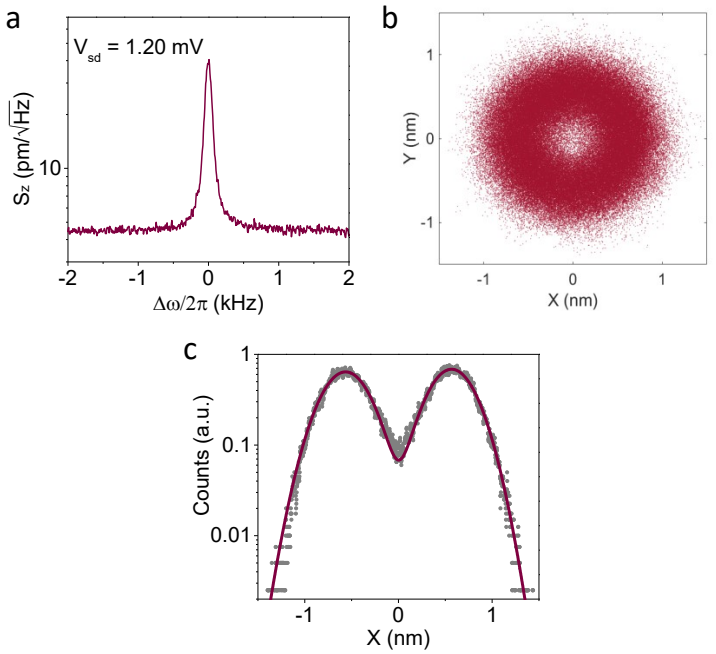

FIGURE B.5: **Pure self-oscillation. (a)** Displacement spectral density at $V_{sd} = 1.2$ mV and $V_g = -616$ mV. **(b)** The phase-space of the two quadratures of the motion. **(c)** Histogram associated to the phase-space in **b**.

Johnson-Nyquist noise of the total circuit and of the HEMT noise. This background contribution is independent of the source-drain voltage V_{sd}, so that it can be quantified from the current noise measured at $V_{sd} = 0$ mV. After the substraction of this background contribution, we determine the Fano factor F of the nanotube device at finite V_{sd} from the measured current noise using $F = S_{II}(V_{sd})/(2eI_{sd})$, where e is the electron charge, and I_{sd} is the DC current at a given source-drain bias V_{ds} (Fig. B.6).

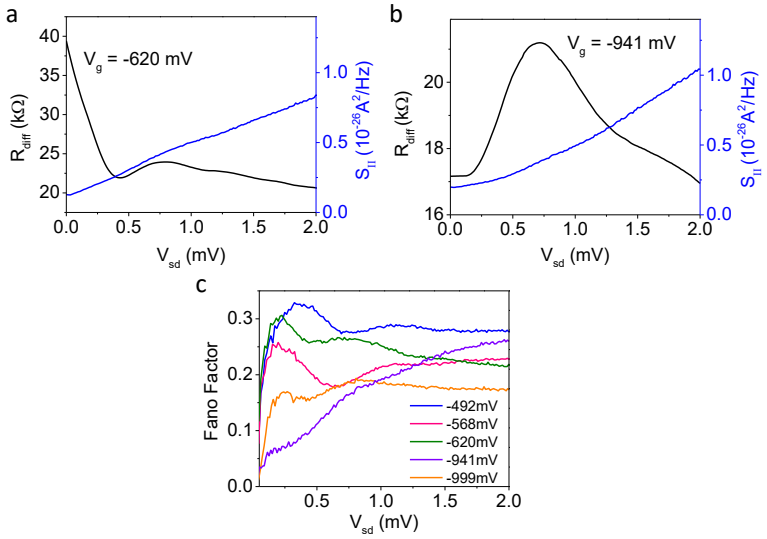

FIGURE B.6: **Shot noise measurements. (a,b)** Differential resistance R_{diff} (grey) and current noise density S_{II} (blue) as a function of V_{sd} for two different gate voltage values. **(c)** Fano factor as a function of V_{sd} for different V_{g} values.

B.5 Displacement sensitivity

The current noise floor $S_{\mathrm{I}}^{\mathrm{imp}}$ at ω_{RLC} sets the displacement imprecision noise $S_{\mathrm{z}}^{\mathrm{imp}}$ of the detection method using

$$S_{\mathrm{z}}^{\mathrm{imp}} = \left(\frac{1}{2} \frac{dG_{\mathrm{diff}}}{dV_{\mathrm{g}}} V_{\mathrm{g}} V_{\mathrm{sd}}^{\mathrm{ac}} \frac{C_{\mathrm{g}}'}{C_{\mathrm{g}}} \right)^{-1} S_{\mathrm{I}}^{\mathrm{imp}}. \tag{B.5}$$

The current noise floor at zero source-drain bias is given by the HEMT noise and the Johnson-Nyquist noise of the circuit. When increasing the bias, the contribution of the electron shot noise dominates the displacement sensitivity (Fig. B.7(a)). The V_{sd} dependence of the imprecision displacement noise is obtained using Eq. B.5 (Fig. B.7(b)). The imprecision noise can reach the level of the displacement noise $S_{\mathrm{z}}^{\mathrm{zpf}} = \sqrt{2\hbar/m\omega_0\Gamma_{\mathrm{width}}}$ of the zero-point fluctuations at resonance frequency (Fig. B.7(c)).

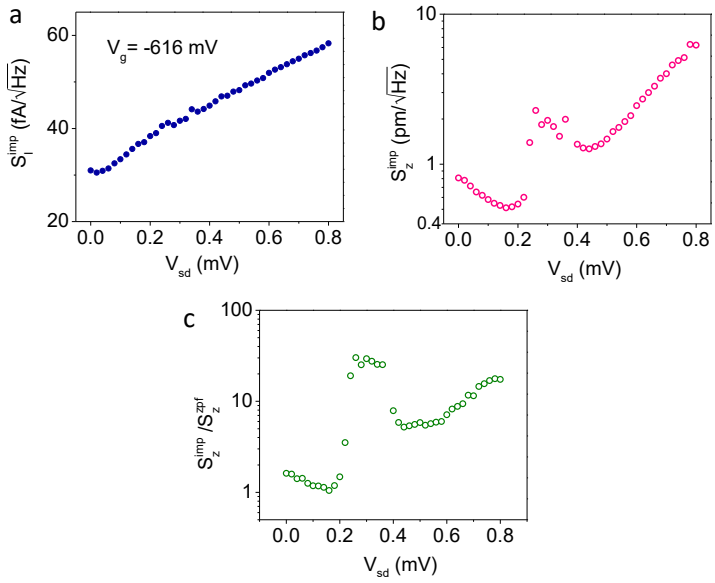

FIGURE B.7: **Displacement sensitivity. (a,b)** Current noise floor and displacement imprecision noise as a function of V_{sd}. **(c)** Same as (b) but with the displacement imprecision noise normalised by the displacement noise of the zero-point fluctuations at resonance frequency.

B.6 Backaction

B.6.1 Retardation time due to the circuit

Fig. B.8 shows the simplified electrical circuit used to evaluate the electrostatic and the electrothermal backactions when the retardation is given by the circuit. We consider the impedances relevant at the resonance frequency of the resonator. The nanotube with conductance G is connected on the source electrode to the capacitance $C_{RC} \simeq 60$ pF of the coaxial cable and the resistance $R_{50} = 50\,\Omega$ of an attenuator, which form the impedance of the circuit

$$Z_T = \left(R_{50}^{-1} + i\omega C_{RC}\right)^{-1}. \tag{B.6}$$

The mechanical vibrations modulate the nanotube conductance by the amount δG. When a DC voltage V_{sd} is applied to the source electrode nanotube, the conductance modulation generates an oscillating current δi_{ac} at the frequency close to ω_0. The current flowing through Z_T

creates an oscillating voltage δv_{ac} on the source electrode, so that

$$\delta v_{ac} = -\delta i_{ac} Z_T, \tag{B.7}$$
$$\delta i_{ac} = \delta G V_{sd} + G \delta v_{ac}. \tag{B.8}$$

Reference [187] made a similar analysis as here. The difference in the two analysis comes from the fact that our device is biased with a constant voltage, while the device in Ref. [187] is biased with a constant current.

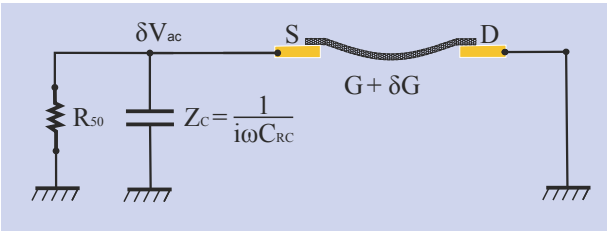

FIGURE B.8: **Simplified electrical circuit.**

The retardation time τ_{RC} of the backaction on the vibrations is of the order of $1/\omega_0$. The retardation time is related to the delay of the modulation of δv_{ac} with respect to δG. We thus express δv_{ac} as

$$\delta v_{ac} = -\frac{Z_T}{1 + Z_T G} \delta G V_{sd} \simeq -R_{50} \frac{1 - i\omega R_{50} C_{RC}}{1 + \omega^2 R_{50}^2 C_{RC}^2} \delta G V_{sd}, \tag{B.9}$$

where we use $R_{50} G << 1$ in the last equality. The argument of the complex number in the numerator is $\varphi = -\arctan(\omega R_{50} C_{RC})$, so that the retardation time is

$$\tau_{RC} = \frac{\arctan(\omega_0 R_{50} C_{RC})}{\omega_0}. \tag{B.10}$$

From the values of C_{RC}, R_{50}, and $\omega_0 \simeq 2\pi \cdot 92$ MHz, we get that $\omega_0 R_{50} C_{RC} = 1.7$. Therefore, the retardation time τ_{RC} of the circuit is of the order of $1/\omega_0$. The estimation $\omega_0 \tau_{RC} \sim 1$ is relevant, since this enhances cooling [198].

B.6.2 Electrostatic backaction with the retardation due to the circuit

As described in the last subsection, the modulation of the voltage δv_{ac} on the source electrode is due to the vibration-induced modulation of the conductance, when the nanotube is biased with a constant voltage. Assuming symmetric electrical contacts, the voltage modulation on

the nanotube is $\delta v_{\rm NT} = \frac{1}{2}\delta v_{\rm ac}$. This results in the electrostatic force

$$\delta F = C'_{\rm g} V_{\rm g} \delta v_{\rm NT} = -\frac{1}{2} C'_{\rm g} V_{\rm g} R_{50} \frac{1 - i\omega R_{50} C_{\rm RC}}{1 + \omega^2 R_{50}^2 C_{\rm RC}^2} \frac{\partial G}{\partial z} V_{\rm sd} \delta z. \quad \text{(B.11)}$$

The real part of this backaction force leads to the shift of the spring constant, and the imaginary part to the shift of the decay rate. Using $F = -m\Delta\Gamma_{\rm back}\frac{dz}{dt}$ and $\frac{dz}{dt} = i\omega z$, we get

$$\Delta k_{\rm back} = \frac{1}{2}\left(\frac{R_{50}}{1 + (R_{50}\omega C_{\rm RC})^2}\right) \frac{dG_{\rm diff}}{dV_{\rm g}} \frac{(C'_{\rm g} V_{\rm g})^2}{C_{\rm g}} V_{\rm sd}, \quad \text{(B.12)}$$

$$\Delta\Gamma_{\rm back} = -\frac{1}{2m}\left(\frac{R_{50}^2 C_{\rm RC}}{1 + (R_{50}\omega C_{\rm RC})^2}\right) \frac{dG_{\rm diff}}{dV_{\rm g}} \frac{(C'_{\rm g} V_{\rm g})^2}{C_{\rm g}} V_{\rm sd} \quad \text{(B.13)}$$

The retardation time of the backaction on the vibrations is about $1/\omega_0$.

This backaction cannot account for our data. Eq. B.13 cannot account for the efficient cooling in Figs. 8.6(a,c) shown in Chap. 8, since the predicted $\Delta\Gamma$ is one order of magnitude smaller than that measured in Fig. 8.6(d) of in Chap. 8.

B.6.3 Electrothermal backaction with the retardation due to the circuit

The closed loop of the backaction goes as follows. The dissipated power increases the temperature of the device. The effective thermal expansion of the device leads to the displacement of the nanotube. This displacement reacts back on the dissipated power via $\delta G = \frac{\partial G}{\partial z}\delta z$. The delay of the retardation time is $\tau_{\rm RC}$.

The dissipated power of the voltage-biased nanotube is $P = (G + \delta G)(V_{\rm sd} + \delta v_{\rm ac})^2$. The first-order expansion of the power reads

$$\delta P_1 = V_{\rm sd}^2 \delta G - 2\frac{Z_{\rm T} G}{1 + Z_{\rm T} G} V_{\rm sd}^2 \delta G. \quad \text{(B.14)}$$

The first term of this equation leads to backaction when taking into account the thermalization time of the device, as discussed in the next subsection. The second term results in the change of the decay rate because of the retardation of the circuit. This is what is discussed here.

The modulation of the dissipated power leads to the modulation of the mechanical tension in the nanotube. The tension modulation depends on the temperature profile along the nanotube and the electrodes, which is something hard to know precisely especially at low temperature when the electron transport is quasi-coherent [70]. In what follows, we assume for simplicity that the dissipation occurs solely in the nanotube, and that temperature rises by $\delta T = \delta P \tau_{\rm ph}/C_{\rm heat}$. Here, $C_{\rm heat}$ is the heat capacity of the nanotube and $\tau_{\rm ph}$ is

the thermalization time of the nanotube. We do an additional simplification using $\tau_{\mathrm{ph}} \simeq L/v \simeq 0.1$ ns, where L is the nanotube length and $v \simeq 10^4$ m/s is the phonon velocity in nanotubes [199]. Assuming that the thermal expansion is solely occurring in the nanotube, the nanotube expands by $\frac{\delta L}{L} = \alpha_{\mathrm{TEC}} \delta T$ where α_{TEC} is the thermal expansion coefficient of the nanotube. Using Hook's law, the change of the mechanical tension is given by $\delta T_{\mathrm{mech}} = 2\pi r E_{2\mathrm{d}} \frac{\delta L}{L}$ where $E_{2\mathrm{d}} = 340\,\mathrm{N/m}$ is the two-dimensional Young's modulus of graphene and r the nanotube radius. Overall, the mechanical tension is related to the dissipated power by

$$\delta T_{\mathrm{mech}} = \frac{\alpha_{\mathrm{TEC}} E_{2\mathrm{d}} \tau_{\mathrm{ph}}}{C_{\mathrm{heat}}} 2\pi r \delta P_1. \tag{B.15}$$

We emphasize that we would get a linear relation between the tension and the power as in Eq. B.15 albeit with a different ratio $\delta T_{\mathrm{mech}}/\delta P_1$, if we were considering dissipation in the electrodes and/or thermal expansion of the electrodes.

The modulation of the mechanical tension generates a shift in the spring constant and in the decay rate. For this, we use the Euler-Bernoulli equation that reads

$$\rho S \frac{d^2 Z}{dt^2} = -EI \frac{d^4 Z}{dx^4} + \left[T_{\mathrm{mech}} + \frac{ES}{2L} \int_0^L \left(\frac{dZ}{dx} \right)^2 dx \right] \frac{d^2 Z}{dx^2} \tag{B.16}$$

where ρ is the nanotube mass density, S the nanotube cross-sectional area, Z the displacement at the coordinate x along the nanotube axis, t the time, E the nanotube three-dimensional Young's modulus, and I the moment of inertia. We assume that the restoring force is solely given by the mechanical tension, as it is the case in our experiment, so that $EI \frac{d^4 Z}{dx^4} \to 0$. We set

$$Z(x,t) = z_{\mathrm{s}} \times \phi_{\mathrm{s}}(x) + z_1(t) \times \phi_1(x). \tag{B.17}$$

Here, $\phi_{\mathrm{s}}(x)$ and $\phi_1(x)$ are the profiles of the static deformation and the measured eigenmode with $\max(\phi_{\mathrm{s}}(x)) = \max(\phi_1(x))$=1, whereas z_{s} and $z_1(t)$ are the associated time dependent displacements. We use $\phi_{\mathrm{s}}(x) = \phi_1(x) = \sin(\pi x/L)$, a good approximation since the nanotube is under tensile tension. The equation of motion is obtained by multiplying the Euler-Bernoulli equation by $\phi_1(x)$ and integrating it along x. The mechanical tension is $T_{\mathrm{mech}} = T^0_{\mathrm{mech}} - \delta T_{\mathrm{mech}}$ where T^0_{mech} is the time-independent tension in the nanotube. The time-dependent tension creates a term proportional to z_1. The real part of this term induces a shift in the spring constant, and the imaginary part

leads to a shift in the decay rate,

$$\Delta k_{\text{back}} = \alpha m \frac{1}{C_{\text{RC}} R_{50}} \frac{dG_{\text{diff}}}{dV_{\text{g}}} \frac{C'_{\text{g}}}{C_{\text{g}}} V_{\text{g}} z_s V_{\text{sd}}^2, \tag{B.18}$$

$$\Delta \Gamma_{\text{back}} = -\alpha \frac{dG_{\text{diff}}}{dV_{\text{g}}} \frac{C'_{\text{g}}}{C_{\text{g}}} V_{\text{g}} z_s V_{\text{sd}}^2, \tag{B.19}$$

$$\alpha = \frac{\pi^3 r}{L} \frac{\alpha_{\text{TEC}} E_{2\text{d}} \tau_{\text{ph}}}{C_{\text{heat}}} \frac{1}{m} \left(\frac{2 C_{\text{RC}} G R_{50}^2}{\left(\omega C_{\text{RC}} R_{50}\right)^2 + 1} \right). \tag{B.20}$$

The retardation time of the backaction on the vibrations is about $1/\omega_0$, that is, $\tau \simeq 2$ ns.

We now compare the measurements of the decay rate as a function of V_{sd} in Fig. 8.5(b) and Fig. 8.6(d) in Chap. 8 with Eq. B.19 (pink lines). We estimate that the static displacement is $z_s = -0.97$ nm at $V_{\text{g}} = -616$ mV and $z_s = -2.08$ nm at $V_{\text{g}} = -943$ mV using $z_s = -\frac{4}{\pi} \frac{C'_{\text{g}} V_{\text{g}}^2}{m \omega_0^2}$ from the derivation of the Euler-Bernoulli equation. We use $C_{\text{heat}} = 1.6 \cdot 10^{-22}$ J/K from Ref. [200] where the specific heat capacity of nanotubes is $3 \cdot 10^{-5}$ J/gK at 0.1 K. The only free parameter left is the thermal expansion coefficient. From the comparison between the measurements and this model, we get $\alpha_{\text{TEC}} = 9 \cdot 10^{-8}$ 1/K. Although we did not find any report on α_{TEC} for nanotubes, graphene, and graphite at such low temperatures, the order of magnitude that we get is rather realistic. The temperature modulation involved in the backaction at $V_{\text{g}} = -943$ mV is estimated to be 40 μK and 0.4 mK at $V_{\text{sd}} = 0.1$ mV and $V_{\text{sd}} = 0.565$ mV, respectively.

To finish this subsection, we discuss the third-order expansion of the power modulation related to Eq. B.14, since it is relevant for the self-oscillation regime. The third-order expansion reads

$$\delta P_3 = V_{\text{sd}}^2 \delta G^3 \left(\frac{Z_{\text{T}}}{1 + Z_{\text{T}} G} \right)^2. \tag{B.21}$$

Carrying out the same derivation as that described above, we obtain two additional backaction force terms, that is, a Duffing force and a nonlinear decay force of the form $z^2 \frac{dz}{dt}$. Depending on the sign of $\frac{dG_{\text{diff}}}{dV_{\text{g}}}$, the nonlinear decay force can be negative, so that this force further increases the amplification, especially when the amplitude of motion is large. The exact derivation of the nonlinear decay force is difficult due to its renormalization by the other nonlinear forces. The study of this nonlinear force is beyond the scope of this work.

B.6.4 Electrothermal backaction with the retardation due to the thermalization time of the device

In contrast to the backaction discussed in the last subsection, this backaction arises from the modulation of the power $\delta P_1 = V_{sd}^2 \delta G$ in Eq. B.14 associated to the thermalization time of the device. The derivation of the backaction is similar to that above. The time-dependent tension that is induced by δP_1 creates a force F proportional to z_1 in the equation of motion. The shift in the decay rate is given by $\Delta\Gamma_{back} = \frac{1}{m}\frac{\partial F}{\partial z_1}\tau_{ph}$ when the thermalization time τ_{ph} is much shorter than ω_0 [198]. As a result, we obtain

$$\Delta\Gamma_{back} = -\alpha \frac{dG_{diff}}{dV_g}\frac{C_g'}{C_g} V_g z_s V_{sd}^2, \tag{B.22}$$

$$\alpha = \pi^3 \frac{r}{Lm}\frac{\alpha_{TEC} E_{2d} \tau_{ph}^2}{C_{heat}}. \tag{B.23}$$

When we compare the measured V_{sd} dependence of the decay rate with this model, the agreement is satisfactory. The functional form of Eq. B.22 is the same as that in Eq. B.19 when the retardation is due to the circuit. From the comparison between the measurements and this model, we get $\alpha_{TEC} = 3 \cdot 10^{-9}$ 1/K, which is smaller that the value obtained when the retardation is due to the circuit. The temperature modulation involved in the backaction at $V_g = -943$ mV is estimated to be 0.8 mK and 9 mK at $V_{sd} = 0.1$ mV and $V_{sd} = 0.565$ mV, respectively.

Bibliography

[1] G. Binnig, C. F. Quate, and Ch. Gerber. "Atomic Force Microscope". In: *Phys. Rev. Lett.* 56 (1986), p. 930 (cit. on p. 13).

[2] A. D. O'Connell, M. Hofheinz, M. Ansmann, R. C. Bialczak, M. Lenander, E. Lucero, M. Neeley, D. Sank, H. Wang, M. Weides, J. Wenner, J. M. Martinis, and A. N. Cleland. "Quantum ground state and single-phonon control of a mechanical resonator". In: *Nature* 464 (2010), 697—703 (cit. on p. 13).

[3] B. P. Abbott *et al*. "Observation of Gravitational Waves from a Binary Black Hole Merger". In: *Phys. Rev. Lett.* 116 (2016), p. 061102 (cit. on p. 13).

[4] A. N. Cleland and M. L. Roukes. "A nanometre-scale mechanical electrometer". In: *Nature* 392.6672 (1998), p. 160 (cit. on p. 14).

[5] R. G. Knobel and A. N. Cleland. "Nanometre-scale displacement sensing using a single electron transistor". In: *Nature* 424 (2003), pp. 291–293 (cit. on pp. 14, 80, 87, 101).

[6] M. T. Woodside and P. L. McEuen. "Scanned Probe Imaging of Single-Electron Charge States in Nanotube Quantum Dots". In: *Science* 296.5570 (2002), pp. 1098–1101 (cit. on pp. 14, 80, 87, 101).

[7] B. Lassagne, Y. Tarakanov, J. Kinaret, D. Garcia-Sanchez, and A. Bachtold. "Coupling Mechanics to Charge Transport in Carbon Nanotube Mechanical Resonators". In: *Science* 325.5944 (2009), pp. 1107–1110 (cit. on pp. 14, 80, 87, 101).

[8] G. A. Steele, A. K. Hüttel, B. Witkamp, M. Poot, H. B. Meerwaldt, L. P. Kouwenhoven, and H. S. J. van der Zant. "Strong Coupling Between Single-Electron Tunneling and Nanomechanical Motion". In: *Science* 325.5944 (2009), pp. 1103–1107 (cit. on pp. 14, 80, 82, 87, 101).

[9] N. Ares, T. Pei, A. Mavalankar, M. Mergenthaler, J. H. Warner, G. A. D. Briggs, and E. A. Laird. "Resonant Optomechanics with a Vibrating Carbon Nanotube and a Radio-Frequency Cavity". In: *Phys. Rev. Lett.* 117.17 (2016), p. 170801 (cit. on pp. 14, 80, 87, 101).

[10] Y. Wen, N. Ares, F. J. Schupp, T. Pei, G. A. D. Briggs, and E. A. Laird. "A coherent nanomechanical oscillator driven by single-electron tunnelling". In: *Nature Phys.* 16.1 (2020), pp. 75–82 (cit. on pp. 14, 76).

[11] M. D. LaHaye, O. Buu, B. Camarota, and K. C. Schwab. "Approaching the quantum limit of a nanomechanical resonator". In: *Science* 304.5667 (2004), pp. 74–77 (cit. on p. 14).

[12] A. Naik, O. Buu, M. D. LaHaye, A. D. Armour, A. A. Clerk, M. P. Blencowe, and K. C. Schwab. "Cooling a nanomechanical resonator with quantum back-action". In: *Nature* 443.7108 (2006), pp. 193–196 (cit. on pp. 14, 80).

[13] K. J. Lulla, M. Defoort, C. Blanc, O. Bourgeois, and E. Collin. "Evidence for the role of normal-state electrons in nanoelectromechanical damping mechanisms at very low temperatures". In: *Phys. Rev. Lett.* 110.17 (2013), p. 177206 (cit. on p. 14).

[14] M. D. LaHaye, J. Suh, P. M. Echternach, K. C. Schwab, and M. L. Roukes. "Nanomechanical measurements of a superconducting qubit". In: *Nature* 459.7249 (2009), pp. 960–964 (cit. on pp. 14, 101).

[15] A. Noury, J. Vergara-Cruz, P. Morfin, M. C. Gordillo, J. Boronat, S. Balibar, and A. Bachtold. "Layering Transition in Superfluid Helium Adsorbed on a Carbon Nanotube Mechanical Resonator". In: *Phys. Rev. Lett.* 122 (2019), p. 165301 (cit. on pp. 14, 56, 64, 95).

[16] A. M. Guénault, A. Guthrie, R. P. Haley, S. Kafanov, Yu. A. Pashkin, V. Pickett G. R. andTsepelin, D. E. Zmeev, E. Collin, R. Gazizulin, and O. Maillet. "Detecting a phonon flux in superfluid ^{4}He by a nanomechanical resonator". In: *Phys. Rev. Lett.* 101 (2020), p. 060503 (cit. on p. 14).

[17] C. A. Regal, J. D. Teufel, and K. W. Lehnert. "Measuring nanomechanical motion with a microwave cavity interferometer". In: *Nature Phys.* 4.7 (2008), p. 555 (cit. on p. 14).

[18] J. D. Teufel, T. Donner, D. Li, J. W. Harlow, M. S. Allman, K. Cicak, A. J. Sirois, J. D. Whittaker, K. W. Lehnert, and R. W. Simmonds. "Sideband cooling of micromechanical motion to the quantum ground state". In: *Nature* 475.7356 (2011), p. 359 (cit. on p. 14).

[19] D. Rugar, C. S. Yannoni, and J. A. Sidles. "Mechanical detection of magnetic resonance". In: *Nature* 360.6404 (1992), p. 563 (cit. on p. 14).

[20] D. Rugar, R. Budakian, H. J. Mamin, and B. W. Chui. "Single spin detection by magnetic resonance force microscopy". In: *Nature* 430 (2004), 329—332 (cit. on pp. 14, 56, 62, 92).

[21] C. L. Degen, M. Poggio, H. J. Mamin, C. T. Rettner, and D. Rugar. "Nanoscale magnetic resonance imaging". In: *PNAS* 106 (2009), pp. 1313–1317 (cit. on pp. 14, 56).

[22] V. Sazonova, Y. Yaish, H. Ustunel, D. Roundy, T. A. Arias, and P. L. McEuen. "A tunable carbon nanotube electromechanical oscillator". In: *Nature* 431.7006 (2004), pp. 284–287 (cit. on pp. 14, 101).

[23] J. Chaste, M. Sledzinska, M. Zdrojek, J. Moser, and A. Bachtold. "High-frequency nanotube mechanical resonators". In: *Appl. Phys. Lett.* 99.21 (2011), p. 213502 (cit. on p. 14).

[24] E. A. Laird, F. Pei, W. Tang, G. A Steele, and L. P. Kouwenhoven. "A high quality factor carbon nanotube mechanical resonator at 39 GHz". In: *Nano Lett.* 12.1 (2011), pp. 193–197 (cit. on p. 14).

[25] J. Moser, A. Eichler, J. Güttinger, M. I. Dykman, and A. Bachtold. "Nanotube mechanical resonators with quality factors of up to 5 million". In: *Nature Nanotech.* 9 (2014), pp. 1007–1011 (cit. on pp. 14, 80, 81, 101).

[26] A. K. Hüttel, G. A. Steele, B. Witkamp, M. Poot, L. P. Kouwenhoven, and H. S. J. van der Zant. "Carbon Nanotubes as Ultrahigh Quality Factor Mechanical Resonators". In: *Nano Lett.* 9.7 (2009), pp. 2547–2552 (cit. on pp. 14, 80, 81, 101).

[27] J. Chaste, A. Eichler, J. Moser, G. Ceballos, R. Rurali, and A. Bachtold. "A nanomechanical mass sensor with yoctogram resolution". In: *Nature Nanotech.* 7 (2012), 301—304 (cit. on pp. 14, 56, 59).

[28] J. Moser, J. Güttinger, A. Eichler, M. J. Esplandiu, D. E. Liu, M. I. Dykman, and A. Bachtold. "Ultrasensitive force detection with a nanotube mechanical resonator". In: *Nature Nanotech.* 8 (2013), 493—496 (cit. on pp. 14, 56).

[29] S. L. de Bonis, C. Urgell, W. Yang, C. Samanta, A. Noury, J. Vergara-Cruz, Q. Dong, Y. Jin, and A. Bachtold. "Ultrasensitive Displacement Noise Measurement of Carbon Nanotube Mechanical Resonators". In: *Nano Lett.* 18.8 (2018), pp. 5324–5328 (cit. on pp. 14, 56, 64, 66, 68, 80, 81, 89, 101).

[30] R. Martel, V. Derycke, C. Lavoie, J. Appenzeller, K. K. Chan, J. Tersoff, and Ph. Avouris. "Ambipolar Electrical Transport in Semiconducting Single-Wall Carbon Nanotubes". In: *Phys. Rev. Lett* 87 (2001), p. 256805 (cit. on pp. 14, 20).

[31] P. Jarillo-Herrero, S. Sapmaz, C. Dekker, L. P. Kouwenhoven, and H. S. J. van der Zant. "Electron-hole symmetry in a semiconducting carbon nanotube quantum dot". In: *Nature* 429 (2004), 389—392 (cit. on pp. 14, 20).

[32] E. A. Laird, F. Kuemmeth, G. A. Steele, K. Grove-Rasmussen, J. Nygård, K. Flensberg, and L. P. Kouwenhoven. "Quantum transport in carbon nanotubes". In: *Rev. Mod. Phys.* 87 (2015), p. 703 (cit. on pp. 14, 70, 75, 76, 80, 81, 97, 98).

[33] M. Bockrath, D. H. Cobden, P. L. McEuen, N. G. Chopra, A. Zettl, A. Thess, and R. E. Smalley. "Single-Electron Transport in Ropes of Carbon Nanotubes". In: *Science* 275.5308 (1997), pp. 1922–1925 (cit. on pp. 14, 26, 70).

[34] J. Cao, Q. Wang, M. Rolandi, and H. Dai. "Aharonov-bohm interference and beating in single-walled carbon nanotube interferometers". In: *Phys. Rev. Lett.* 93 (2004), p. 216803 (cit. on p. 14).

[35] G. A. Steele, G. Gotz, and L. P. Kouwenhoven. "Tunable few-electron double quantum dots and Klein tunnelling in ultra-clean carbon nanotubes". In: *Nature Nanotech.* 4.5944 (2009), 363—367 (cit. on pp. 14, 20).

[36] S. J. Tans, M. H. Devoret, H. Dai, A. Thess, R. E. Smalley, L. J. Geerligs, and C. Dekker. "Individual single-wall carbon nanotubes as quantum wires". In: *Nature* 386 (1997), p. 474 (cit. on pp. 14, 26, 70).

[37] J. Nygård, D. H. Cobden, and P. E. Lindelof. "Kondo physics in carbon nanotubes". In: *Nature* 408 (2000), p. 342 (cit. on pp. 14, 30, 70).

[38] W. Liang, M. Bockrath, and H. Park. "Shell Filling and Exchange Coupling in Metallic Single-Walled Carbon Nanotubes". In: *Phys. Rev. Lett.* 88 (2002), p. 126801 (cit. on p. 14).

[39] B. Babić, T. Kontos, and C. Schönenberger. "Kondo effect in carbon nanotubes at half filling". In: *Phys. Rev. B* 70 (2004), p. 235419 (cit. on p. 14).

[40] P. Jarillo-Herrero, J. Kong, H. S. J. van der Zant, C. Dekker, L. P. Kouwenhoven, and S. De Franceschi. "Orbital Kondo effect in carbon nanotubes". In: *Nature* 434 (2005), p. 484 (cit. on pp. 14, 70, 75).

[41] W. Liang, M. Bockrath, D. Bozovic, J. H. Hafner, M. Tinkham, and H. Park. "Fabry - Perot interference in a nanotube electron waveguide". In: *Nature* 411.6838 (2001), pp. 665–669 (cit. on pp. 14, 34, 35, 70, 71, 73).

[42] A. Dirnaichner, M. del Valle, K. J. G. Götz, F. J. Schupp, N. Paradiso, M. Grifoni, Ch. Strunk, and A. K. Hüttel. "Secondary Electron Interference from Trigonal Warping in Clean Carbon Nanotubes". In: *Phys. Rev. Lett.* 117 (2016), p. 166804 (cit. on pp. 14, 34, 70, 72, 95, 96).

[43] M. Aspelmeyer, T. J. Kippenberg, and F. Marquardt. "Cavity Optomechanics". In: *Rev. Mod. Phys.* 86 (2014), p. 1391 (cit. on pp. 14, 79).

[44] J. B. Clark, F. Lecocq, R. W. Simmonds, J. Aumentado, and J. D. Teufel. "Sideband cooling beyond the quantum backaction limit with squeezed light". In: *Nature* 541 (2017), pp. 191–195 (cit. on pp. 14, 79).

[45] M. Rossi, D. Mason, J. Chen, Y. Tsaturyan, and A. Schliesser. "Measurement-based quantum control of mechanical motion". In: *Nature* 563.7729 (2018), pp. 53–58 (cit. on pp. 14, 79).

[46] J. Chan, T. P. Mayer Alegre, A. H. Safavi-Naeini, J. T. Hill, A. Krause, S. Gröblacher, M. Aspelmeyer, and O. Painter. "Laser cooling of a nanomechanical oscillator into its quantum ground state". In: *Nature* 478 (2011), 89—92 (cit. on p. 14).

[47] S. Gigan, H. R. Böhm, F. Paternostro M. andBlaser, J. B. Langer G.and Hertzberg, K. C. Schwab, D. Bäuerle, Aspelmeyer M., and A. Zeilinger. "Strong Coupling Between Single-Electron Tunneling and Nanomechanical Motion". In: *Nature* 444 (2006), pp. 67–70 (cit. on p. 14).

[48] R. A. Barton, I. R. Storch, V. P. Adiga, R. Sakakibara, B. R. Cipriany, B. Ilic, S. P. Wang, P. Ong, P. L. McEuen, J. M. Parpia, and H. G. Craighead. "Photothermal Self-Oscillation and Laser Cooling of Graphene Optomechanical Systems". In: *Nano Lett.* 12.9 (2012), pp. 4681–4686 (cit. on pp. 14, 87, 89).

[49] A. D. Armour, M. P. Blencowe, and Y. Zhang. "Classical dynamics of a nanomechanical resonator coupled to a single-electron transistor". In: *Phys. Rev. B* 69.12 (2004), p. 125313 (cit. on pp. 14, 80, 87).

[50] A. Hajimiri M. L. Roukes X. L. Feng C. J. White. "A self-sustaining ultrahigh-frequency nanoelectromechanical oscillator". In: *Nature Nanotech.* 3 (2008), pp. 342–346 (cit. on p. 14).

[51] S. Iijima. "Helical microtubules of graphitic carbon". In: *Nature* 354 (1991), pp. 56–58 (cit. on p. 17).

[52] K. S. Novoselov, A. K. Geim, S. V. Morozov, D. Jiang, Y. Zhang, S. V. Dubonos, I. V. Grigorieva, and A. A. Firsov. "Electric Field Effect in Atomically Thin Carbon Films". In: *Science* 306 (2004), pp. 666–669 (cit. on p. 17).

[53] M. José-Yacamán, M. Miki-Yoshida, L. Rendón, and J. G. Santiesteban. "Catalytic growth of carbon microtubules with fullerene structure". In: *Applied Physics* 62 (1993), pp. 202–204 (cit. on p. 17).

[54] T. Guo, P. Nikolaev, A. Thess, D. T. Colbert, and R. E. Smalley. "Catalytic growth of single-walled manotubes by laser vaporization". In: *Chem. Phys. Lett.* 243 (1995), pp. 49–54 (cit. on p. 17).

[55] T. W. Ebbesen and P. M. Ajayan. "Large-scale synthesis of carbon nanotubes". In: *Nature* 358 (1992), pp. 220–220 (cit. on p. 17).

[56] L. X. Zheng, M. J. O'Connell, S. K. Doorn, X. Z. Liao, Y. H. Zhao, E. A. Akhadov, M. A. Hoffbauer, B. J. Roop, Q. X. Jia, R. C. Dye, Peterson, D. E., S. M. Huang, J. Liu, and Y. T. Zhu. "Ultralong single-wall carbon nanotubes". In: *Nature Mater.* 3 (2004), 673—676 (cit. on p. 17).

[57] N. Geblinger, A. Ismach, and E. Joselevich. "Self-organized nanotube serpentines". In: *Nature Nanotech.* 3 (2008), 195—200 (cit. on p. 17).

[58] C. Lu and J. Liu. "Controlling the Diameter of Carbon Nanotubes in Chemical Vapor Deposition Method by Carbon Feeding". In: *Phys. Chem. B* 110.41 (2006), 20254—20257 (cit. on p. 17).

[59] Y. Li, R. Cui, L. Ding, Y. Liu, W. Zhou, Y. Zhang, Z Jin, F. Peng, and J. Liu. "How Catalysts Affect the Growth of Single-Walled Carbon Nanotubes on Substrates". In: *Adv. Mater.* 22 (2010), 1508—1515 (cit. on p. 17).

[60] V. Gavryushin. *Graphene Brillouin Zone and Electronic Energy Dispersion*. Vol. 122. Wolfram Demonstrations Project, 2011, p. 165301 (cit. on p. 18).

[61] S. Ilani and P.McEuen. "Electron Transport in Carbon Nanotubes". In: *Annu. Rev. Condens. Matter Phys.* 1 (2010), 1—25 (cit. on p. 20).

[62] M.-F. Yu, B. S. Files, S. Arepalli, and R. S. Ruoff. "Tensile Loading of Ropes of SingleWall Carbon Nanotubes and their Mechanical Properties". In: *Phys. Rev. Lett.* 84.24 (2000), 5552—5555 (cit. on p. 21).

[63] E. D. Minot, V. Yaish Y. Sazonova, J.-Y. Park, M. Brink, and P. L. McEuen. "Tuning Carbon Nanotube Band Gaps with Strain". In: *Phys. Rev. Lett.* 90.15 (2003), p. 156401 (cit. on p. 21).

[64] B. Babíc, J. Furer, S. Sahoo, S. Farhangfar, and C. Schönenberger. "Intrinsic Thermal Vibrations of Suspended Doubly Clamped Single-Wall Carbon Nanotubes". In: *Nano Lett.* 3.11 (2003), 1577—1580 (cit. on p. 21).

[65] L. P. Kouwenhoven, C. M. Marcus, P. L. McEuen, S. Tarucha, R. M. Westervelt, and N. S. Wingreen. "Mesoscopic Electron transport". In: vol. 122. Springer, Dordrecht, 1997. Chap. Electron transport in quantum dots, pp. 105–214 (cit. on pp. 26, 70).

[66] D. V. Averin and Yu. V. Nazarov. *Single Charge Tunneling - Coulomb Blockade Phenomena in Nanostructures*. Ed. by H. Grabert and M.H. Devoret. Vol. 122. Springer, 1992, pp. 217–247 (cit. on p. 30).

[67] D. Goldhaber-Gordon, Hadas Shtrikman, D. Mahalu, David Abusch-Magder, U. Meirav, and M. A. Kastner. "Kondo effect in a single-electron transistor". In: *Nature* 391 (1998), p. 156 (cit. on p. 30).

[68] Sara M. Cronenwett, Tjerk H. Oosterkamp, and Leo P. Kouwenhoven. "A Tunable Kondo Effect in Quantum Dots". In: *Science* 281.5376 (1998), pp. 540–544 (cit. on p. 30).

[69] W. G. van der Wiel, S. de Franceschi, T. Fujisawa, J. M. Elzerman, S. Tarucha, and L. P. Kouwenhoven. "The Kondo Effect in the Unitary Limit". In: *Science* 289.5487 (2000), pp. 2105–2108 (cit. on p. 31).

[70] S. Datta. *Electronic transport in mesoscopic systems*. Vol. 122. Cambridge University Press, Cambridge, 1995, p. 165301 (cit. on pp. 33, 34, 69, 110).

[71] M. Cahay, M. McLennan, and S. Datta. "Conductance of an array of elastic scatterers: A scattering matrix approach". In: *Phys. Rev. B* 37 (1988), pp. 10125–10136 (cit. on pp. 33, 34).

[72] T. S. Chu and T. Itoh. "Generalized scattering matrix method for analysis of cascaded and offset microstrip step discontinuities". In: *IEEE transactions on microwave theory and techniques* 34 (1986), pp. 280–284 (cit. on pp. 33, 34).

[73] N. Lotfizadeh, M. J. Senger, D. R. McCulley, E. D. Minot, and V. V. Deshpande. "Sagnac Electron Interference as a Probe of Electronic Structure". In: *arXiv:1808.01341* 122 (2018), p. 165301 (cit. on pp. 34, 70, 72, 95).

[74] J. B. Johnson. "The Schottky Effect in Low Frequency Circuits". In: *Phys. Rev.* 26 (1925), p. 71 (cit. on p. 36).

[75] W. Schottky. "Small-Shot Effect and Flicker Effect". In: *Phys. Rev.* 28 (1926), p. 74 (cit. on pp. 36, 37).

[76] J. B. Johnson. "Thermal Agitation of Electricity in Conductors". In: *Phys. Rev.* 32 (1928), p. 97 (cit. on p. 36).

[77] H. Nyquist. "Thermal Agitation of Electric Charge in Conductors". In: *Phys. Rev.* 32 (1928), p. 110 (cit. on p. 36).

[78] R. J. Schoelkopf, A. A. Clerk, S. M. Girvin, K. W. Lehnert, and M. H. Devoret. "Quantum Noise in Mesoscopic Physics". In: vol. 122. Springer, Dordrecht, 2003. Chap. Qubits as Spectrometers of Quantum Noise, pp. 175–203 (cit. on p. 37).

[79] U. Fano. "Ionization Yield of Radiations. II. The Fluctuations of the Number of Ions". In: *Phys. Rev.* 72 (1947), p. 26 (cit. on p. 37).

[80] H. Birk, M. J. M. de Jong, and C. Schönenberger. "Shot-Noise Suppression in the Single-Electron Tunneling Regime". In: *Phys. Rev. Lett.* 75 (1995), 1610—1613 (cit. on p. 37).

[81] A. Nauen, I. Hapke-Wurst, F. Hohls, U. Zeitler, R. J. Haug, and K. Pierz. "Shot noise in self-assembled InAs quantum dots". In: *Phys. Rev. B* 66 (2002), p. 161303 (cit. on p. 37).

[82] H. van Wees B. J. and. van Houten, J. G Beenakker C. W. J. and. Williamson, L. P. Kouwenhoven, D. van der Marel, and C. T. Foxon. "Quantized conductance of point contacts in a two-dimensional electron gas". In: *Phys. Rev. Lett.* 60 (1988), p. 848 (cit. on p. 37).

[83] Y. Ronen, Y. Cohen, J.-H. Kang, A. Haim, M.-T. Rieder, M. Heiblum, D. Mahalu, and H. Shtrikman. "Charge of a quasi-particle in a superconductor". In: *PNAS* 113.7 (2016), pp. 1743–1748 (cit. on p. 37).

[84] H. B. Callen and T. A. Welton. "Irreversibility and Generalized Noise". In: *Phys. Rev.* 83 (1951), p. 34 (cit. on p. 42).

[85] D. Des Cloizeaux. "Theory of condensed matter". In: vol. 122. IAEA, Vienna, 1968. Chap. Linear Response Theory, pp. 325–354 (cit. on pp. 43, 48).

[86] R. Kubo. "Statistical Mechanical Theory of Irreversible Processes I". In: *J. Phys. Soc. Jpn.* 12 (1957), 570—586 (cit. on pp. 43, 48).

[87] R. Lifshitz and M. C. Cross. *Reviews of Nonlinear Dynamics and Complexity. Reviews of Nonlinear Dynamics and Complexity*. Ed. by H. G. Schuster. Vol. 1. Wiley-VCH, 2009, 1—52 (cit. on pp. 44, 45).

[88] H. W. Ch. Postma, I. Kozinsky, A. Husain, and M. L. Roukes. "Dynamic range of nanotube- and nanowire-based electromechanical systems". In: *Appl. Phys. Lett.* 86 (2005), p. 223105 (cit. on p. 44).

[89] A. Eichler, J. Moser, J. Chaste, M. Zdroje, I. Wilson-Rae, and A. Bachtold. "Nonlinear damping in mechanical resonators made from carbon nanotubes and graphene". In: *Nature Nanotech.* 6 (2011), 339—342 (cit. on p. 45).

[90] E. M. Lifshitz, A. M. Kosevich, and L. P. Pitaevskii. *Theory of elasticity*. Ed. by L. D. Landau and E. M. Lifshitz. Vol. 122. Elsevier, 1986, 1—195 (cit. on p. 45).

[91] A. A. Clerk and S. Bennett. "Quantum nanoelectromechanics with electrons, quasi-particles and Cooper pairs effective bath descriptions and strong feedback effects". In: *New J. Phys.* 7 (2005), p. 238 (cit. on pp. 48, 80, 87).

[92] A. A. Clerk, M. H. Devoret, S. M. Girvin, F. Marquardt, and R. J. Schoelkopf. "Introduction to quantum noise, measurement, and amplification". In: *Rev. Mod. Phys.* 82 (2010), p. 1155 (cit. on p. 48).

[93] S. Huang, X. Cai, and J. Liu. "Growth of millimeter-long and horizontally aligned single-walled carbon nanotubes on flat substrates". In: *J. Am. Chem. Soc.* 125 (2003), pp. 5636–5637 (cit. on p. 55).

[94] S. Huang, M. Woodson, R. Smalley, and J. Liu. "Growth mechanism of oriented long single walled carbon nanotubes using "fast-heating" chemical vapor deposition process". In: *Nano Lett.* 4.6 (2004), pp. 1025–1028 (cit. on p. 55).

[95] Y. T. Yang, C. Callegari, X. L. Feng, K. L. Ekinci, and M. L. Roukes. "Zeptogram-Scale Nanomechanical Mass Sensing". In: *Nano Lett.* 6 (2006), pp. 583–586 (cit. on pp. 56, 59).

[96] H.-Y. Chiu, P. Hung, H. W. C. Postma, and M. Bockrath. "Atomic-Scale Mass Sensing Using Carbon Nanotube Resonators". In: *Nano Lett.* 8 (2008), pp. 4342–4346 (cit. on pp. 56, 59).

[97] E. Gil-Santos, D. Ramos, J. Martinez, M. Fernandez-Regulez, R. Garcia, A. San Paulo, M. Calleja, and J. Tamayo. "Nanomechanical mass sensing and stiffness spectrometry based on two-dimensional vibrations of resonant nanowires". In: *Nature Nanotech.* 5 (2010), 641–645 (cit. on pp. 56, 59).

[98] H. J. Mamin and D. Rugar. "Sub-attonewton force detection at millikelvin temperatures". In: *Appl. Phys. Lett.* 79 (2001), pp. 3358–3360 (cit. on p. 56).

[99] E. Gavartin, P. Verlot, and T. J. Kippenberg. "A hybrid on-chip optomechanical transducer for ultrasensitive force measurements". In: *Nature Nanotech.* 7 (2012), pp. 509–514 (cit. on p. 56).

[100] M. Héritier, A. Eichler, Y. Pan, U. Grob, I. Shorubalko, M. D. Krass, Y. Tao, and C. L. Degen. "Nanoladder Cantilevers Made from Diamond and Silicon". In: *Nano Lett.* 18 (2018), pp. 1814–1818 (cit. on pp. 56, 62, 92).

[101] M. S. Hanay, S. Kelber, A. K. Naik, D. Chi, S. Hentz, E. C. Bullard, E. Colinet, L. Duraffourg, and M. L. Roukes. "Single-protein nanomechanical mass spectrometry in real time". In: *Nature Nanotech.* 7 (2012), 602–608 (cit. on pp. 56, 59).

[102] M. S. Hanay, S. Kelber, C. D. O'Connell, P. Mulvaney, J. E. Sader, and M. L. Roukes. "Inertial imaging with nanomechanical systems". In: *Nature Nanotech.* 10 (2015), 339–344 (cit. on pp. 56, 59).

[103] S. Dominguez-Medina, S. Fostner, M. Defoort, M. Sansa, A.-K. Stark, M. A. Halim, E. Vernhes, M. Gely, G. Jourdan, T. Alava, P. Boulanger, C. Masselon, and S. Hentz. "Neutral mass spectrometry of virus capsids above 100 megadaltons with nanomechanical resonators". In: *Science* 362 (2018), pp. 918–922 (cit. on pp. 56, 59).

[104] Z. Wang, J. Wei, P. Morse, J. G. Dash, O. E. Vilches, and David H. Cobden. "Phase Transitions of Adsorbed Atoms on the Surface of a Carbon Nanotube". In: *Science* 327 (2010), pp. 552–555 (cit. on pp. 56, 59).

[105] Y. T. Yang, C. Callegari, X. L. Feng, and M. L. Roukes. "Surface Adsorbate Fluctuations and Noise in Nanoelectromechanical Systems". In: *Nano Lett.* 11 (2011), pp. 1753–1759 (cit. on pp. 56, 59).

[106] J. Atalaya, A. Isacsson, and M. I. Dykman. "Diffusion-Induced Bistability of Driven Nanomechanical Resonators". In: *Phys. Rev. Lett.* 106 (2011), p. 227202 (cit. on p. 56).

[107] A. Tavernarakis, J. Chaste, A. Eichler, G. Ceballos, M. C. Gordillo, J. Boronat, and A. Bachtold. "Atomic Monolayer Deposition on the Surface of Nanotube Mechanical Resonators". In: *Phys. Rev. Lett.* 112 (2014), p. 196103 (cit. on pp. 56, 59).

[108] C. Rhén and A. Isacsson. "Particle number scaling for diffusion-induced dissipation in graphene and carbon nanotube nanomechanical resonators". In: *Phys. Rev. B* 93 (2016), p. 125414 (cit. on p. 56).

[109] J. Schwender, I. Tsioutsios, A. Tavernarakis, Q. Dong, Y. Jin, U. Staufer, and A. Bachtold. "Improving the read-out of the resonance frequency of nanotube mechanical resonators". In: *Appl. Phys. Lett.* 113 (2018), p. 063104 (cit. on pp. 56, 59).

[110] N. Rossi, F. R. Braakman, D. Cadeddu, D. Vasyukov, G. Tütüncüoglu, A. Fontcuberta i Morral, and M. Poggio. "Vectorial scanning force microscopy using a nanowire sensor". In: *Nature Nanotech.* 12 (2017), 150–155 (cit. on pp. 56, 62, 92).

[111] L. M. de Lépinay, B. Pigeau, B. Besga, P. Vincent, P. Poncharal, and O. Arcizet. "A universal and ultrasensitive vectorial nanomechanical sensor for imaging 2D force fields". In: *Nature Nanotech.* 12 (2017), 156–162 (cit. on pp. 56, 62, 92).

[112] J. M. Nichol, T. R. Naibert, E. R. Hemesath, L. J. Lauhon, and R. Budakian. "Nanoscale Fourier-Transform Magnetic Resonance Imaging". In: *Phys. Rev. X* 3 (2013), p. 031016 (cit. on pp. 56, 62, 92).

[113] I. Khivrich, A. A. Clerk, and S. Ilani. "Nanomechanical pump-probe measurements of insulating electronic states in a carbon nanotube". In: *Nature Nanotech.* 14.2 (2019), pp. 161–167 (cit. on pp. 56, 81, 101).

[114] A. W. Barnard, M. Zhang, G. S. Wiederhecker, M. Lipson, and P. L. McEuen. "Real-time vibrations of a carbon nanotube". In: *Nature* 566 (2019), 89–93 (cit. on p. 56).

[115] M. Nishio, S. Sawaya, S. Akita, and Y. Nakayama. "Density of electron-beam-induced amorphous carbon deposits". In: *Journal of Vacuum Science & Technology B* 23 (2005), pp. 1975–1979 (cit. on p. 56).

[116] S. Sawaya, S. Akita, and Y. Nakayama. "In situ mass measurement of electron-beam-induced nanometer-sized W-related deposits using a carbon nanotube cantilever". In: *Appl. Phys. Lett.* 89 (2006), p. 193115 (cit. on p. 56).

[117] V. Friedli, C. Santschi, J. Michler, P. Hoffmann, and I. Utke. "Mass sensor for in situ monitoring of focused ion and electron beam induced processes". In: *Appl. Phys. Lett.* 90 (2007), p. 053106 (cit. on p. 56).

[118] A. Banerjee, T. Mankad, S. Dhamodaran, J. Ramkumar, and V. N. Kulkarni. "The measurement of attogram mass accumulation on nanostructures during e-beam scanning, using carbon nanopillars in resonant mode". In: *Nanotechnology* 20 (2009), p. 345501 (cit. on p. 56).

[119] S. Sangiao, C. Magen, D. Mofakhami, G. de Loubens, and J. M. de Teresa. "Magnetic properties of optimized cobalt nanospheres grown by focused electron beam induced deposition (FEBID) on cantilever tips". In: *Beilstein J. Nanotechnol.* 8 (2017), 2106–2115 (cit. on p. 56).

[120] A. Tavernarakis, A. Stavrinadis, A. Nowak, I. Tsioutsios, A. Bachtold, and P. Verlot. "Optomechanics with a hybrid carbon nanotube". In: *Nature Comm.* 9 (2018), p. 662 (cit. on pp. 56, 59).

[121] I. Tsioutsios, A. Tavernarakis, J. Osmond, P. Verlot, and A. Bachtold. "Real-Time Measurement of Nanotube Resonator Fluctuations in an Electron Microscope". In: *Nano Lett.* 17 (2017), pp. 1748–1755 (cit. on pp. 56, 57).

[122] S. Pairis, F. Donatini, M. Hocevar, D. Tumanov, N. Vaish, J. Claudon, J.-P. Poizat, and P. Verlot. "Shot-noise-limited nanomechanical detection and radiation pressure backaction from an electron beam". In: *Phys. Rev. Lett.* 122 (2019), p. 083603 (cit. on pp. 56, 62, 92).

[123] J. D. Wnuk, J. M. Gorham, S. G. Rosenberg, W. F. van Dorp, T. E. Madey, C. W. Hagen, and D. H. Fairbrother. "Electron Induced Surface Reactions of the Organometallic Precursor Trimethyl (methylcyclopentadienyl) platinum(IV)". In: *J. Phys. Chem. C* 113 (2009), pp. 2487–2496 (cit. on p. 57).

[124] R. Winkler, B. B. Lewis, J. D. Fowlkes, P. D. Rack, and H. Plank. "High-Fidelity 3D-Nanoprinting via Focused Electron Beams Growth Fundamentals". In: *ACS Applied Nano Materials* 1 (2018), pp. 1014–1027 (cit. on p. 60).

[125] A. Botman, J. J. L. Mulders, and C. W. Hagen. "Creating pure nanostructures from electron-beam-induced deposition using purification techniques a technology perspective". In: *Nanotechnology* 20 (2009), p. 372001 (cit. on pp. 62, 92).

[126] M. Huth, F. Porrati, and O. V. Dobrovolskiy. "Focused electron beam induced deposition meets materials science". In: *Microelectronic Engineering* 185-186 (2018), pp. 9–28 (cit. on pp. 62, 92).

[127] N. Rossi, B. Gross, F. Dirnberger, D. Bougeard, and M. Poggio. "Magnetic Force Sensing Using a Self-Assembled Nanowire". In: *Nano Lett.* 19 (2019), pp. 930–936 (cit. on pp. 62, 92).

[128] R. Fischer, D. P. McNally, C. Reetz, G. G. T. Assumpcao, T. Knief, Y. Lin, and C. A. Regal. "Spin detection with a micromechanical trampoline towards magnetic resonance microscopy harnessing cavity optomechanics". In: *New J. of Phys.* 21 (2019), p. 043049 (cit. on pp. 62, 92).

[129] T. Henry, K. Kim, Z. Ren, C. Yerino, J. Han, and H. X. Tang. "Directed Growth of Horizontally Aligned Gallium Nitride Nanowires for Nanoelectromechanical Resonator Arrays". In: *Nano Lett.* 7 (2007), pp. 3315–3319 (cit. on pp. 62, 92).

[130] A. Niguès, A. Siria, and P. Verlot. "Dynamical backaction cooling with free electrons". In: *Nature Comm.* 6 (2015), p. 8104 (cit. on pp. 62, 92).

[131] F. R. Braakman and M. Poggio. "Force sensing with nanowire cantilevers". In: *Nanotechnology* 30 (2019), p. 332001 (cit. on pp. 62, 92).

[132] I. Yeo, P.-L. de Assis, A. Gloppe, E. Dupont-Ferrier, P. Verlot, N. S. Malik, E. Dupuy, J. Claudon, J-M. Gérard, A. Auffèves, G. Nogues, S. Seidelin, J.-P. Poizat, O. Arcizet, and M. Richard. "Strain-mediated coupling in a quantum dot–mechanical oscillator hybrid system". In: *Nature Nanotech.* 9 (2014), 106–110 (cit. on pp. 62, 92).

[133] M. Defoort, K. J. Lulla, T. Crozes, O. Maillet, O. Bourgeois, and E. Collin. "Slippage and Boundary Layer Probed in an Almost Ideal Gas by a Nanomechanical Oscillator". In: *Phys. Rev. Lett.* 113 (2014), p. 136101 (cit. on pp. 62, 92).

[134] J. P. Mathew, R. Patel, A. Borah, C. B. Maliakkal, T. S. Abhilash, and M. M. Deshmukh. "Nanoscale Electromechanics To Measure Thermal Conductivity, Expansion, and Interfacial Losses". In: *Nano Lett.* 15 (2015), pp. 7621–7626 (cit. on pp. 62, 92).

[135] E. Gil-Santos, C. Baker, D. T. Nguyen, W. Hease, C. Gomez, A. Lemaître, S. Ducci, G. Leo, and I. Favero. "High-frequency nano-optomechanical disk resonators in liquids". In: *Nature Nanotech.* 10 (2015), 810–816 (cit. on pp. 62, 92).

[136] A. H. Ghadimi, S. A. Fedorov, N. J. Engelsen, M. J. Bereyhi, R. Schilling, D. J. Wilson, and T. J. Kippenberg. "Elastic strain engineering for ultralow mechanical dissipation". In: *Science* 360 (2018), pp. 764–768 (cit. on pp. 62, 92).

[137] S. K. Roy, V. T. K. Sauer, J. N. Westwood-Bachman, A. Venkatasubramanian, and W. K. Hiebert. "Improving mechanical sensor performance through larger damping". In: *Science* 360 (2018), p. 5220 (cit. on pp. 62, 92).

[138] P. Paulitschke, F. Keber, A. Lebedev, J. Stephan, H. Lorenz, S. Hasselmann, D. Heinrich, and E. M. Weig. "Ultraflexible Nanowire Array for Label- and Distortion-Free Cellular Force Tracking". In: *Nano Lett.* 19 (2019), pp. 2207–2214 (cit. on pp. 62, 92).

[139] Q. Dong, Y.X. Liang, U. Gennser, A. Cavanna, and Y. Jin. "The Role of the Gate Geometry for Cryogenic HEMTs: Towards an Input Voltage Noise Below 0.5nV/$sqrtHz$ at 1 kHz and 4.2 K". In: *J. Low. Temp. Phys.* 167 (2012), 626—631 (cit. on p. 64).

[140] Q. Dong, Y. X. Liang, D. Ferry, A. Cavanna, L. Couraud, and Y. Jin. "Ultra-low noise high electron mobility transistors for high-impedance and low frequency deep cryogenic readout electronics". In: *Appl. Phys. Lett.* 105 (2014), p. 013504 (cit. on p. 64).

[141] D. I. Bradley, R. E. George, D. Gunnarsson, R. P. Haley, H. Heikkinen, Y. A. Pashkin, J. Penttilä, J. R. Prance, M. Prunnila, L. Roschier, and M. Sarsby. "Nanoelectronic primary thermometry below 4mK". In: *Nature Comm.* 7 (2016), p. 10455 (cit. on pp. 65, 92).

[142] Z. Iftikhar, A. Anthore, S. Jezouin, F. D. Parmentier, Y. Jin, A. Cavanna, A. Ouerghi, U. Gennser, and F. Pierre. "Primary thermometry triad at 6mK in mesoscopic circuits". In: *Nature Comm.* 7 (2016), p. 12908 (cit. on pp. 65, 92).

[143] M. Büttiker. "Four-terminal phase-coherent conductance". In: *Phys. Rev. Lett.* 57 (1986), p. 1761 (cit. on p. 67).

[144] Y. M. Blanter and M. Büttiker. "Shot noise in mesoscopic conductors". In: *Phys. Rep.* 336 (2000), pp. 1–166 (cit. on pp. 67, 76, 92).

[145] S. D. Bennett, J. Maassen, and A. A. Clerk. "Scattering approach to backaction in coherent nanoelectromechanical systems". In: *Phys. Rev. Lett.* 105 (2010), p. 217206 (cit. on p. 67).

[146] S. De Franceschi and J. A. van Dam. "Single-electron tunneling in InP nanowires". In: *Appl. Phys. Lett.* 83 (2003), p. 344 (cit. on p. 70).

[147] Vikram V. Deshpande and Marc Bockrath. "The one-dimensional Wigner crystal in carbon nanotubes". In: *Nature Phys.* 4 (2008), pp. 314–318 (cit. on pp. 70, 80).

[148] S. Pecker, F. Kuemmeth, A. Secchi, M. Rontani, D. C. Ralph, P. L. McEuen, and S. Ilani. "Observation and spectroscopy of a two-electron Wigner molecule in an ultraclean carbon nanotube". In: *Nature Phys.* 9 (2013), p. 576 (cit. on p. 70).

[149] I. Shapir, A. Hamo, S. Pecker, C. P. Moca, Ö. Legeza, G. Zarand, and S. Ilani. "Imaging the electronic Wigner crystal in one dimension". In: *Science* 364.6443 (2019), pp. 870–875 (cit. on p. 70).

[150] N. Lotfizadeh, D. R. McCulley, M. J. Senger, H. Fu, E. D. Minot, B. Skinner, and V. V. Deshpande. "Band-Gap-Dependent Electronic Compressibility of Carbon Nanotubes in the Wigner Crystal Regime". In: *Phys. Rev. Lett.* 123.19 (2019), p. 197701 (cit. on p. 70).

[151] M. Bockrath, D.H. Cobden, J. Lu, A.G. Rinzler, R.E. Smalley, L. Balents, and P.L. McEuen. "Luttinger liquid behavior in carbon nanotubes". In: *Nature* 397 (1997), p. 598 (cit. on p. 70).

[152] H. W. C. Postma, T. Teepen, Z. Yao, M. Grifoni, and C. Dekker. "Carbon nanotube single electron transistor at room temperature". In: *Science* 293.5527 (2001), pp. 76–79 (cit. on p. 70).

[153] J. Paaske, A. Rosch, P. Wöle, N. Mason, C. M. Marcus, and J. Nygård. "Non-equilibrium singlet-triplet Kondo effect in carbon nanotubes". In: *Nature Phys.* 2 (2006), pp. 460–464 (cit. on p. 70).

[154] A. Makarovski, J. Liu, and G. Finkelstein. "Evolution of Transport Regimes in Carbon Nanotube Quantum Dots". In: *Phys. Rev. Lett.* 99 (2007), p. 066801 (cit. on pp. 70, 75, 76).

[155] T.-F. Fang, W. Zuo, and H.-G. Luo. "Kondo Effect in Carbon Nanotube Quantum Dots with Spin-Orbit Coupling". In: *Phys. Rev. Lett.* 101 (2008), p. 246805 (cit. on p. 70).

[156] J. P. Cleuziou, N. V. N'Guyen, S. Florens, and W. Wernsdorfer. "Interplay of the Kondo Effect and Strong Spin-Orbit Coupling in Multihole Ultraclean Carbon Nanotubes". In: *Phys. Rev. Lett.* 111 (2013), p. 136803 (cit. on p. 70).

[157] D. R. Schmid, S. Smirnov, M. Margaska, A. Dirnaichner, P. L. Stiller, M. Grifoni, A. K. Hüttel, and C. Strunk. "Broken SU(4) symmetry in a Kondo-correlated carbon nanotube". In: *Phys. Rev. B* 91 (2015), p. 155435 (cit. on p. 70).

[158] M. Niklas, S. Smirnov, D. Mantelli, M. Marganska, N. Nguyen, W. Wernsdorfer, J. Cleuziou, and M. Grifoni. "Blocking transport resonances via Kondo many-body entanglement in quantum dots". In: *Nature Comm.* 7 (2016), p. 12442 (cit. on p. 70).

[159] M. Ferrier, T. Arakawa, T. Hata, R. Fujiwara, R. Delagrange, R. Weil, R. Deblock, R. Sakano, A. Oguri, and K. Kobayashi. "Universality of non-equilibrium fluctuations in stronly correlated quantum liquids". In: *Nature Phys.* 12 (2016), p. 230 (cit. on pp. 70, 75).

[160] M. Ferrier, T. Arakawa, T. Hata, R. Fujiwara, R. Delagrange, R. Deblock, Y. Teratani, R. Sakano, A. Oguri, and K. Kobayashi. "Quantum Fluctuations along Symmetry Crossover in a Kondo-Correlated Quantum Dot". In: *Phys. Rev. Lett.* 118 (2017), p. 196803 (cit. on p. 70).

[161] M. M. Desjardins, J. J. Viennot, M. C. Dartiailh, L. E. Bruhat, M. R. Delbecq, M. Lee, M.-S. Choi, A. Cottet, and T. Kontos. "Observation of the frozen charge of a Kondo resonance". In: *Nature* 545 (2017), pp. 71–74 (cit. on p. 70).

[162] T. S. Jespersen, M. Aagesen, C. Sørensen, P. E. Lindelof, and J. Nygård. "Kondo physics in tunable semiconductor nanowire quantum dots". In: *Phys. Rev. B* 74 (2006), p. 233304 (cit. on p. 70).

[163] L. V. Litvin, H.-P. Tranitz, W. Wegscheider, and C. Strunk. "Decoherence and single electron charging in an electronic Mach-Zehnder interferometer". In: *Phys. Rev. B* 75 (2007), p. 033315 (cit. on p. 70).

[164] N. Y. Kim, P. Recher, W. D. Oliver, Y Yamamoto, J. Kong, and H. Dai. "Tomonaga-Luttinger Liquid Features in Ballistic Single-Walled Carbon Nanotubes: Conductance and Shot Noise". In: *Phys. Rev. Lett.* 99 (2007), p. 036802 (cit. on p. 70).

[165] A. V. Kretinin, R. Popovitz-Biro, D. Mahalu, and H. Shtrikman. "Multimode Fabry-Perot conductance oscillations in suspended stacking-faults-free InAs nanowires". In: *Nano Lett.* 10 (2010), p. 3439 (cit. on p. 70).

[166] I. Neder, M. Heiblum, Y. Levinson, D. Mahalu, and V. Umansky. "Unexpected Behavior in a Two-Path Electron Interferometer". In: *Phys. Rev. Lett.* 96 (2006), p. 016804 (cit. on p. 70).

[167] J. Cao, Q. Wang, and H. Dai. "Electron transport in very clean, as-grown suspended carbon nanotubes". In: *Nature Materials* 4 (2005), p. 745 (cit. on pp. 72, 95).

[168] F. B. Anders, D. E. Logan, M. R. Galpin, and G. Finkelstein. "Zero-Bias Conductance in Carbon Nanotube Quantum Dots". In: *Phys. Rev. Lett.* 100 (2008), p. 086809 (cit. on pp. 75, 76).

[169] E. Onac, F. Balestro, B. Trauzettel, C. F. J. Lodewijk, and L. P. Kouwenhoven. "Shot-Noise Detection in a Carbon Nanotube Quantum Dot". In: *Phys. Rev. Lett.* 96 (2006), p. 026803 (cit. on pp. 76, 93).

[170] P. Recher, N. Y. Kim, and Y. Yamamoto. "Tomonaga-Luttinger liquid correlations and Fabry-Perot interference in conductance and finite-frequency shot noise in a single-walled carbon nanotube". In: *Phys. Rev. B* 74 (2006), p. 235438 (cit. on pp. 76, 93).

[171] F. Wu, P. Queipo, A. Nasibulin, T. Tsuneta, T. H. Wang, E. Kauppinen, and P. J. Hakonen. "Shot Noise with Interaction Effects in Single-Walled Carbon Nanotubes". In: *Phys. Rev. Lett.* 99 (2007), p. 156803 (cit. on pp. 76, 93).

[172] L. G. Herrmann, T. Delattre, P. Morfin, J.-M. Berroir, B. Plaçais, D. C. Glattli, and T. Kontos. "Shot Noise in Fabry-Perot Interferometers Based on Carbon Nanotubes". In: *Phys. Rev. Lett.* 99 (2007), p. 156804 (cit. on pp. 76, 93).

[173] P. Treutlein, C. Genes, K. Hammerer, M. Poggio, and P. Rabl. *Hybrid Mechanical Systems*. Ed. by M. Aspelmeyer, T. Kippenberg, and F. Marquardt. Vol. 122. Springer, Berlin, Heidelberg, 2014, p. 165301 (cit. on p. 79).

[174] A. Benyamini, A. Hamo, S. Viola Kusminskiy, F. von Oppen, and S. Ilani. "Real-space tailoring of the electron-phonon coupling in ultraclean nanotube mechanical resonators". In: *Nature Phys.* 10 (2014), pp. 151–156 (cit. on pp. 80, 87, 101).

[175] Y. Okazaki, I. Mahboob, K. Onomitsu, S. Sasaki, and H. Yamaguchi. "Gate-controlled electromechanical backaction induced by a quantum dot". In: *Nature Comm.* 7 (2016), p. 11132 (cit. on pp. 80, 87, 101).

[176] K. J. G. Götz, D. R. Schmid, F. J. Schupp, P. L. Stiller, Ch. Strunk, and A. K. Hüttel. "Nanomechanical Characterization of the Kondo Charge Dynamics in a Carbon Nanotube". In: *Phys. Rev. Lett.* 120.24 (2018), p. 246802 (cit. on pp. 80, 87, 101).

[177] V. Singh, B. Irfan, G. Subramanian, H. S. Solanki, S. Sengupta, S. Dubey, A. Kumar, S. Ramakrishnan, and M. M. Deshmukh. "Coupling between quantum Hall state and electromechanics in suspended graphene resonator". In: *Appl. Phys. Lett.* 100.23 (2012), p. 233103 (cit. on pp. 80, 101).

[178] C. Chen, V. V. Deshpande, M. Koshino, S. Lee, A. Gondarenko, A. H. MacDonald, P. Kim, and J. Hone. "Modulation of mechanical resonance by chemical potential oscillation in graphene". In: *Nature Phys.* 12 (2016), pp. 240–244 (cit. on pp. 80, 101).

[179] S. Zippilli, G. Morigi, and A. Bachtold. "Cooling Carbon Nanotubes to the Phononic Ground State with a Constant Electron Current". In: *Phys. Rev. Lett.* 102.9 (2009), p. 096804 (cit. on p. 80).

[180] F. Santandrea, L. Y. Gorelik, R. I. Shekhter, and M. Jonson. "Cooling of Nanomechanical Resonators by Thermally Activated Single-Electron Transport". In: *Phys. Rev. Lett.* 106.18 (2011), p. 186803 (cit. on p. 80).

[181] P. Stadler, W. Belzig, and G. Rastelli. "Ground-State Cooling of a Carbon Nanomechanical Resonator by Spin-Polarized Current". In: *Phys. Rev. Lett.* 113.4 (2014), p. 047201 (cit. on p. 80).

[182] L. Arrachea, N. Bode, and F. von Oppen. "Vibrational cooling and thermoelectric response of nanoelectromechanical systems". In: *Phys. Rev. B* 90.12 (2014), p. 125450 (cit. on p. 80).

[183] W. Belzig P. Stadler and G. Rastelli. "Ground-State Cooling of a Mechanical Oscillator by Interference in Andreev Reflection". In: *Phys. Rev. Lett.* 117 (2016), p. 197202 (cit. on p. 80).

[184] A. Hamo, A. Benyamini, I. Shapir, I. Khivrich, J. Waissman, K. Kaasbjerg, Y. Oreg, F. von Oppen, and S. Ilani. "Electron attraction mediated by Coulomb repulsion". In: *Nature* 535 (2016), pp. 395–400 (cit. on p. 80).

[185] X. Song, M. Oksanen, J. Li, P. J. Hakonen, and M. A. Sillanpää. "Graphene Optomechanics Realized at Microwave Frequencies". In: *Phys. Rev. Lett.* 113.2 (2014), p. 027404 (cit. on pp. 87, 89).

[186] P. Weber, J. Güttinger, A. Noury, J. Vergara-Cruz, and A. Bachtold. "Force sensitivity of multilayer graphene optomechanical devices". In: *Nature Comm.* 7 (2016), p. 12496 (cit. on pp. 87, 89).

[187] P. G. Steeneken, K. Le Phan, M. J. Goossens, G. E. J. Koops, G. J. A. M. Brom, C. van der Avoort, and J. T. M. van Beek. "Piezoresistive heat engine and refrigerator". In: *Nature Phys.* 7 (2011), pp. 354–359 (cit. on pp. 87, 88, 109).

[188] E. Bocquillon, V. Freulon, J.-M. Berroir, P. Degiovanni, B. Placais, A. Cavanna, Y. Jin, and G. Feve. "Coherence and Indistinguishability of Single Electrons Emitted by Independent Sources". In: *Science* 339 (2013), pp. 1054–1057 (cit. on p. 89).

[189] T. Jullien, P. Roulleau, B. Roche, A. Cavanna, Y. Jin, and D. C. Glattli. "Quantum tomography of an electron". In: *Nature* 514 (2014), pp. 603–607 (cit. on p. 89).

[190] M. Banerjee, M. Heiblum, V. Umansky, D. E. Feldman, Y. Oreg, and A. Stern. "Observation of half-integer thermal Hall conductance". In: *Nature* 559.7713 (2018), pp. 205–210 (cit. on p. 89).

[191] F. Pistolesi and S. Labarthe. "Current blockade in classical single-electron nanomechanical resonator". In: *Phy. Rev. B* 76.16 (2007), p. 165317 (cit. on pp. 89, 92).

[192] J. D. Teufel, T. Donner, M. A. Castellanos-Beltran, J. W. Harlow, and K. W. Lehnert. "Nanomechanical motion measured with an imprecision below that at the standard quantum limit". In: *Nature Nanotech.* 4 (2009), 820—823 (cit. on p. 92).

[193] J. Zhu, M. Brink, and P. L. McEuen. "Frequency shift imaging of quantum dots with single-electron resolution". In: *Appl. Phys. Lett.* 87.24 (2005), p. 242102 (cit. on p. 101).

[194] R. Stomp, Y. Miyahara, S. Schaer, Q. Sun, H. Guo, P. Grutter, S. Studenikin, P. Poole, and A. Sachrajda. "Detection of Single-Electron Charging in an Individual InAs Quantum Dot by Noncontact Atomic-Force Microscopy". In: *Phys. Rev. Lett.* 94.5 (2005), p. 056802 (cit. on p. 101).

[195] S. D. Bennett, L. Cockins, Y. Miyahara, P. Grütter, and A. A. Clerk. "Strong Electromechanical Coupling of an Atomic Force Microscope Cantilever to a Quantum Dot". In: *Phys. Rev. Lett.* 104 (2010), p. 017203 (cit. on p. 101).

[196] J.-M. Pirkkalainen, S. U. Cho, Francesco Massel, J. Tuorila, T. T. Heikkilä, P. J. Hakonen, and M. A. Sillanpää. "Cavity optomechanics mediated by a quantum two-level system". In: *Nature Comm.* 6 (2015), p. 6981 (cit. on p. 101).

[197] G. Deng, D. Zhu, X. Wang, C. Zou, J. Wang, H. Li, G. Cao, D. Liu, Y. Li, M. Xiao, G. Guo, K. Jiang, X. Dai, and G.g Guo. "Strongly Coupled Nanotube Electromechanical Resonators". In: *Nano Lett.* 16.9 (2016), pp. 5456–5462 (cit. on p. 101).

[198] C. H. Metzger and K. Karrai. "Cavity cooling of a microlever". In: *Nature* 432 (2004), pp. 1002–1005 (cit. on pp. 109, 113).

[199] A. De Martino, R. Egger, and A. O. Gogolin. "Phonon-phonon interactions and phonon damping in carbon nanotubes". In: *Phys. Rev. B* 79 (2009), p. 205408 (cit. on p. 111).

[200] J. Hone, B. Batlogg, Z. Benes, A. T. Johnson, and J. E. Fischer. "Quantized Phonon Spectrum of Single-Wall Carbon Nanotubes". In: *Science* 289.5485 (2000), pp. 1730–1733 (cit. on p. 112).